Bose Gases in Double-Well Potentials

Adam J. Barker

Magdalen College

University of Oxford

A thesis submitted for the degree of

Doctor of Philosophy

Hilary Term, 2020

This thesis is dedicated to the outstanding efforts of the National Health Service during the Covid-19 pandemic.

Acknowledgements

I was extremely lucky as a 17 year-old to have been offered an atomic physics summer project with Dr Matt Jones at Durham University. My physics education thus segued from Ohm's law, to constructing a pyramidal MOT for cold atoms the following week. This, most valuably, was my taste of professional experimental physics which set a steady course towards my Master's and ultimately my doctoral thesis, which no amount of undergraduate practical labs could shake me from.

I would first like to express my sincere gratitude to Professor Christopher Foot for his guidance throughout my time in Oxford. Chris has provided an ideal environment for me to pursue both my academic and extra-curricular interests, which together have made this a thoroughly enriching experience. I would also like to thank Professor Mike Payne, Professor Zoran Hadzibabic, Professor Rob Smith and Dr Raphael Lopes, all of whom went out of their way to encourage me deeper into physics.

My time in the lab has been made so enjoyable by the companionship provided by Dr Elliot Bentine. His encouragement and wicked sense of humour will get any researcher through dark experimental times - I have never laughed harder than the 'quantum physics' mouldy water incident. Dr Kathrin Luksch and I shared many of the struggles of a misbehaving experiment but have emerged the better for it. I thank Kathrin for her kindness and steady supply of continental snacks. I have been supported throughout by many other lab members, including Dr Tiffany Harte, Shinichi Sunami, David Garrick and Abel Beregi. I know I am leaving the experiment in Shinichi, David and Abel's capable hands and expect a great deal from them. I also thank Sean, Leo and all of the other Foot Group members for their invaluable contributions to lab morale.

Outside of the lab, much time has been spent on mowed lawns and backwaters. I am particularly thankful for the lifelong friendships forged within the Cambridge and Oxford University Golf Clubs, Magdalen College Boat Club, Pembroke College RUFC and the Idlers. I extend special thanks to Oxford friends Henry, Rob, Tom, Ercole, Andrew and Steve for their companionship, old Cantabs Michael, James W $\times 2$, Douglas, Mark, Felix, Owen, Alex $\times 2$, Kathy, Lucy, Gigi, Connie and Spence, as well as old-timers Andy, Olly and Dan. I beg the forgiveness of those I cannot accommodate in this very short manifestation of an extremely long list.

I am sincerely grateful to my parents Jane and Darron, Elliot, my grandparents, Anne and Stu, and my extended family for their encouragement and support always. Finally, the headline act: thank you, Heather, for your unabating love and patience.

Bose Gases in Double-Well Potentials

Adam J. Barker

Magdalen College
University of Oxford

A thesis submitted for the degree of
Doctor of Philosophy

Hilary Term, 2020

This thesis presents experimental results which utilise multiple-radiofrequency-dressed potentials as a method of confinement for cold atoms, and details progress towards investigations of the out-of-equilibrium dynamics of two-dimensional systems.

This work has demonstrated the matter-wave interference of Bose gases released from a double-well potential. We investigate the scaling of the matter-wave inteference fringe wavelength, verify the coherence of the experimental procedure, and demonstrate the controllability of the multiple-radiofrequency-dressed potentials to load a prescribed fraction of atoms into each potential well. Methods presented elsewhere were also used to produce two-dimensional Bose gases in the Berezinskii-Kosterlitz-Thouless regime. We present a discussion of phase correlations in two-dimensional Bose gases, including their time-dependent behaviour as the system equilibrates following a quench.

Radiofrequency-dressed potentials are intrinsically state-selective, as we demonstrate through manipulations of a mixture of ^{87}Rb atoms in different hyperfine states within a double-well potential. This can be used to implement species-selective potentials and is a promising architecture for future experiments concerning impurity physics. We find this mixture to be long-lived in the radiofrequency-dressed potential, in stark contrast to recent experiments on this apparatus, in which mixtures of RF-dressed ^{87}Rb and ^{85}Rb were found to suffer from very fast inelastic loss.

Furthermore, we describe the application of machine learning methods to optimise the experimental sequence, in particular the stages of laser cooling and evaporative cooling which are necessary to achieve a quantum gas. We compare several machine learning methods, including Artificial Neural Networks and Gaussian Process regression, and determine experimental parameters which have the strongest influence on the desired outcome. We focus our efforts initially on producing Bose-Einstein condensates with very large atom numbers, although we later highlight the versatility of this method by improving other metrics, such as sequence repetition rate or the final temperature of the gas.

The following publications have arisen from work discussed in this thesis:

- **A. J. Barker**, S. Sunami, D. Garrick, A. Beregi, K. Luksch, E. Bentine and C. J. Foot, *Coherent splitting of two-dimensional Bose gases in magnetic potentials*, New Journal of Physics **22**, 103040 (2020).

- **A. J. Barker**, S. Sunami, D. Garrick, A. Beregi, K. Luksch, E. Bentine and C. J. Foot, *Realising a species-selective double well using multiple-radiofrequency-dressed potentials*, Journal of Physics B: Atomic, Optical and Molecular Physics **53**, 155001 (2020);

- **A. J. Barker**, H. Style, K. Luksch, S. Sunami, D. Garrick, F. Hill, C. J. Foot and E. Bentine, *Applying machine learning optimization methods to the production of a quantum gas*, Machine Learning: Science and Technology **1**, 015007 (2020);

- E. Bentine, **A. J. Barker**, K. Luksch, S. Sunami, T. L. Harte, B. Yuen, D. J. Owens, J. M. Hutson and C. J. Foot, *Inelastic collisions in radiofrequency-dressed mixtures*, Physical Review Research **2**, 033163 (2020);

- K. Luksch, E. Bentine, **A. J. Barker**, S. Sunami, T.L. Harte, B. Yuen and C. J. Foot, *Probing multiple-frequency atom-photon interactions with ultracold atoms*, New Journal of Physics **21**, 073067 (2019).

Publications not discussed in this thesis:

- T. Chalopin, V. Makhalov, C. Bouazza, A. Evrard, **A. J. Barker**, M. Lepers, J-F. Wyart, O. Dulieu, J. Dalibard, R. Lopes and S. Nascimbene, *Anisotropic light-shift and magic-polarization of the intercombination line of Dysprosium atoms in a far-detuned dipole trap*, Physical Review A **98**, 040502 (2018);

- T.L. Harte, E. Bentine, K. Luksch, **A. J. Barker**, D. Trypogeorgos, B. Yuen and C. J. Foot, *Multiple-radiofrequency dressed adiabatic potentials*, Physical Review A **97**, 013616 (2018);

- E. Bentine, T.L. Harte, K. Luksch, **A. J. Barker**, B. Yuen, J. Mur-Petit and C. J. Foot, *Species-selective confinement of rf-dressed atoms*, Journal of Physics B: Atomic, Optical and Molecular Physics **50**, 094002 (2017).

- R. Lopes, C. Eigen, **A. J. Barker**, K. G. H. Viebahn, M. Robert-de-Saint-Vincent, N. Navon, Z. Hadzibabic and R. P. Smith, *Quasiparticle energies in a strongly-interacting homogeneous Bose-Einstein condensate*, Physical Review Letters **118**, 210401 (2017).

Prior to studying in Oxford, I read Natural Sciences at Pembroke College, University of Cambridge. I completed a fourth-year research project with Profs. Zoran Hadzibabic and Robert Smith, where I designed and constructed a Bragg diffraction apparatus for cold-atoms. This device was added to an existing experiment which produced homogeneous Bose-Einstein condensates with tunable interactions. In collaboration with several members of the group, I used the method of Bragg diffraction to probe the quasiparticle excitation spectrum within the condensate and to assess the validity of several theoretical descriptions. I was responsible for collecting experimental data, and supporting further analysis, and this resulted in a publication in Physical Review Letters in 2017.

During the first year of my DPhil studies, I assembled and configured optical apparatus to produce cooling and repumping light for ^{87}Rb, which improved the reliability of the experimental system described within this thesis. As the apparatus is shared at any one time between 3-4 DPhil students, I provided day-to-day assistance in the running and maintenance of the experiment, including re-estabilishing Bose-Einstein condensation after several months of technical difficulties.

Dr. Elliot Bentine built optical apparatus for dual-species laser cooling of ^{85}Rb and ^{87}Rb during 2017. This was used in an investigation of inelastic loss processes in RF-dressed mixtures. I assisted Elliot in the acquisition of data in October-November 2017 and in further discussions with theory collaborators in Durham. This work has recently been published in Physical Review Research.

I completed a two-month internship in the group of Prof. Jean Dalibard, Dr. Raphael Lopes and Dr. Sylvain Nascimbene in College de France, Paris, during my second year. I improved the operation of an existing Zeeman slower and two-dimensional magneto-optical trap for dysprosium and joined an existing investigation into laser cooling at magic wavelengths. This work was published in 2018 in Physical Review A.

I also worked closely with Dr. Kathrin Luksch during my second year and was jointly responsible for the acquisition of spectroscopy data. This work was published in New Journal of Physics in 2019. I also assisted Kathrin, Elliot and Prof. Christopher Foot in the writing of a successful Engineering and Physical Sciences Research Council grant, which was awarded in 2018.

During my third year and fourth years, I led several experimental investigations, which are detailed in Chapters 4, 5, 6 and 7. These include machine learning optimisation of atomic cooling mechanisms; realising a state-selective double-well potential; producing two-dimensional Bose gases in our apparatus; and demonstrating matter-wave interference. Data acquisition, analysis and subsequent preparation of publications were supported by several members of the group, including Dr. Elliot Bentine, Dr. Kathrin Luksch, Shinichi Sunami, David Garrick and Abel Beregi.

I have co-supervised two Master's students during my DPhil. Aleksander Ulatowski designed and built microwave antennae for probing hyperfine transitions in ^{87}Rb, and contributed to a publication in Journal of Physics B in 2020. Harry Style assisted with the writing of code during the machine learning optimisation investigation. This work contributed to a publication in Machine Learning: Science and Technology in 2020.

Contents

Acronyms **10**

List of Figures **11**

1 Introduction **14**

2 Multiple-radiofrequency- dressed potentials **18**
2.1 Energy levels of atoms in magnetic fields 19
2.1.1 Trapping atoms in magnetic fields 21
2.2 The dressed-atom formalism 22
2.3 RF-dressed potentials 23
2.3.1 Species-selectivity 29
2.4 Multiple-radiofrequency-dressed potentials 30
2.5 Two-dimensional potentials 32
2.6 Conclusion 33

3 The experimental apparatus **34**
3.1 The experimental sequence and apparatus 35
3.1.1 The Magneto-optical Trap 35
3.1.2 Light-Induced Atomic Desorption 38
3.1.3 Laser systems 41
3.1.4 The colder Magneto-optical Trap 43
3.1.5 Controlling the experiment 45
3.2 Evaporative cooling 46
3.3 Magnetic traps for cold atoms 47
3.3.1 The magnetic quadrupole trap 48
3.3.2 The Time-Averaged Orbiting Potential trap 49
3.3.3 Implementing RF-dressed potentials 50
3.4 Producing and controlling RF fields 51
3.4.1 Urukul DDS modules 51
3.5 Other hardware 54
3.6 Imaging an atomic cloud 55
3.6.1 Time-of-Flight expansion 57
3.6.2 Horizontal imaging 58

3.6.3 Vertical imaging . . . 61

4 Optimising a quantum gas experiment 62
4.1 Introduction . . . 63
4.2 Implementation . . . 65
4.2.1 Experimental sequence . . . 65
4.2.2 Cost function for optimisation . . . 67
4.2.3 Non-convexity and early stopping . . . 70
4.3 Optimisation methods . . . 71
4.3.1 Differential evolution . . . 73
4.3.2 Gaussian Process regression . . . 74
4.3.3 Artificial Neural Networks . . . 76
4.4 Results . . . 79
4.4.1 Optimising evaporative cooling . . . 80
4.4.2 Sensitivities . . . 83
4.4.3 Simultaneous optimisation of laser cooling and evaporative cooling . . . 86
4.4.4 Tailoring the cost function to other aims . . . 88
4.5 Conclusion . . . 91

5 Realising a species-selective double well 93
5.1 Introduction . . . 94
5.2 Experimental methods . . . 95
5.3 A species-selective double-well potential . . . 96
5.4 Collisional stability of rf-dressed mixtures . . . 99
5.4.1 A dressed mixture of ^{87}Rb and ^{85}Rb . . . 99
5.4.2 A dressed mixture of ^{87}Rb atoms in different hyperfine states . . . 102
5.5 Conclusion and outlook . . . 107

6 Two-dimensional Bose gases 109
6.1 BKT physics in 2D Bose systems . . . 110
6.2 Theory of a 2D Bose Gas . . . 111
6.2.1 The BKT transition in dilute gases . . . 114
6.3 Experiments on 2D Bose gases . . . 115
6.3.1 An absolute calibration of atom number . . . 116
6.3.2 Characterising the potential and the trapped gas . . . 118
6.4 Out-of-equilibrium dynamics . . . 120
6.4.1 Results . . . 126
6.5 Outlook . . . 128

7 Matter-wave interferometry 131
7.1 Introduction and motivation . . . 132
7.2 Experimental methods . . . 134
7.2.1 Fundamental frequencies . . . 136
7.3 Analysis methods . . . 137

7.4 Interferometry of three-dimensional BECs . . . 140
7.5 Coherent splitting . . . 142
7.6 Two-dimensional potential wells . . . 144
7.6.1 Phase correlations . . . 145
7.7 Tunable centre of mass position . . . 148
7.8 Outlook . . . 152
7.8.1 Tomographic imaging . . . 153
7.8.2 Out-of-equilibrium dynamics . . . 155

8 Conclusion **156**
8.1 A gravitational gradiometer . . . 157
8.2 Out-of-equilibrium dynamics of 2D systems . . . 159

A Simulating a finite-temperature quantum gas **162**
A.1 The Hartree-Fock approximation . . . 163
A.2 Coupled Gross-Pitaevskii equations . . . 164
A.2.1 Single-particle excited states . . . 165
A.3 Numerical solution of the Gross-Pitaevskii equation . . . 166
A.3.1 Imaginary time propagation . . . 168
A.3.2 The time-dependent solution . . . 171
A.4 Coupled gases . . . 172
A.5 Conclusion . . . 174

Bibliography **175**

Acronyms

1D	One-dimensional
2D	Two-dimensional
3D	Three-dimensional
RF	Radiofrequency
MRF	Multiple radiofrequency
BEC	Bose-Einstein condensate
BKT	Berezinskii-Kosterlitz-Thouless
PSD	Phase-space density
RWA	Rotating wave approximation
MOT	Magneto-optical Trap
cMOT	Colder Magneto-optical Trap
TOP	Time-Averaged Orbiting Potential
TAAP	Time-Averaged Adiabatic Potential
TOF	Time-of-flight
UHV	Ultra-high vacuum
LIAD	Light-Induced Atomic Desorption
UV	Ultra-Violet
LED	Light-Emitting Diode
PCB	Printed Circuit Board
DDS	Direct Digital Synthesis
FPGA	Field-Programmable Gate Array
TTL	Transistor-transistor logic
LVTTL	Low Voltage Transistor-Transistor logic
SPI	Serial Peripheral Interface
CCD	Charge-coupled device
PID	Proportional-integral-derivative
MW	Microwave
ECDL	External Cavity Diode Laser
DMD	Digital Micromirror device
GP	Gaussian Process
DE	Differential Evolution
NN	Artificial Neural Network
ROI	Region-of-Interest

List of Figures

2.1 Zeeman substates of an atom in a weak magnetic field. 23

2.2 Schematic of the rf-dressed potential trap. 25

2.3 Calibration of the magnetic quadrupole field gradient. 28

2.4 Eigenenergies of RF-dressed states 29

2.5 Double-well potentials using multiple RF fields. 32

3.1 Schematic of the vacuum system. 36

3.2 Energy levels of the ^{87}Rb D2 manifold. 37

3.3 The LIAD LED mounting ring 39

3.4 Effects of UV illumination of a MOT. 41

3.5 Schematic of the cooling and repump optical apparatus. 42

3.6 Schematic of the injection-locked slave laser for cooling light. 43

3.7 Schematic of the tapered amplifier and optical apparatus. 44

3.8 Schematic of the UHV cell-side magnetic trapping apparatus. 49

3.9 PCBs to interface to Urukul DDS units. 53

3.10 Extracting atomic distributions from absorption images. 57

3.11 Horizontal imaging apparatus. 60

3.12 Focussing the horizontal imaging system. 60

4.1 A feedback loop for optimisation. 66

4.2 PSD vs evaporative cooling stage progression. 69
4.3 Illustration of a Gaussian Process. 75
4.4 The simple perceptron. 76
4.5 The ReLU and GELU activation functions. 77
4.6 Structure of an Artificial Neural Network. 78
4.7 Results of optimisation using machine learning vs manual optimisation. 80
4.8 Optimising the quadrupole and TOP evaporative cooling stages. . . . 81
4.9 Discovering sensitive experimental settings. 84
4.10 Optimisation of all cooling processes. 87
4.11 Tailoring the optimisation cost function. 90

5.1 Schematic of the experimental sequence to produce mixtures of atoms in different hyperfine states. 97
5.2 A species-selective double-well potential. 100
5.3 Decay of the number of atoms in states with $F = 1$, $\tilde{m}_F = 1$ and $F = 2$, $\tilde{m}_F = 1$ in an RF-dressed mixture. 106
5.4 Decay of an RF-dressed degenerate mixture of ^{87}Rb atoms in states with $F = 1$ and $F = 2$. 107

6.1 An exact calibration of atom number. 117
6.2 Oscillation frequencies of atoms in the highly anisotropic trap. 119
6.3 Absorption images of Bose gases in the 2D regime. 119
6.4 RF spectroscopy in the shell trap. 121
6.5 Creating an out-of-equilibrium distribution of atoms in the rf-dressed trap. 122
6.6 In-plane expansion in the relaxed trap. 124
6.7 Analysing the atomic distribution. 125
6.8 Preliminary results of out-of-equilibrium dynamics in a 2D Bose gas. . 127

7.1 Matter-Wave Interference of BECs in double wells. 135
7.2 Wavelength of matter-wave interference fringes for 3D BECs as a function of TOF and well separation. 141
7.3 Distribution of the phase across interference patterns. 142
7.4 Interference fringes with 2D Bose gases. 145
7.5 Decay of fringe contrast as a function of integration length. 147
7.6 Controlling the relative populations in each well. 150
7.7 Tuning the interference contrast via the relative well populations. . . 151
7.8 Tomographic imaging and Matter-Wave Interference. 154

8.1 A gravitational gradiometer for atoms with $F = 1$ and $F = 2$. 158
8.2 Signature of unbound vortices in Matter-Wave Interference patterns. . 161

A.1 Eigenstates and eigenenergies of a ^{87}Rb atom in a harmonic potential. 167
A.2 Simulated density profiles of trapped gases. 171
A.3 Simulating TOF for an interacting gas. 172
A.4 Occupation of ground and excited states in a finite-temperature system. 174

1

Introduction

Ultracold gases have emerged as an invaluable tool in the investigation of many-body quantum physics, and studies of these systems have led to an ever-deepening understanding of purely quantum mechanical phase transitions [1, 2]. Bose-Einstein condensation, and the corresponding state of matter, were predicted by Einstein [3], utilising the statistical distribution derived by Bose [4], and was first realised in dilute gases of rubidium and sodium in 1995 [5, 6]. Since these early experiments, as expertise in experimental techniques has grown, research has extended to condensed states of dipolar atoms [7–9], molecules [10–12] and fermions [13–16]. These systems now promise to solve many unanswered questions in fundamental quantum physics.

In contrast to solid state systems, cold atomic gases are highly versatile: atomic species, temperature, density and inter-atomic interactions can be somewhat tuned at will and to suit the experimental aims. Control over these sytems extends to their geometry and dimensionality, which has prompted further enquiry into quantum me-

chanics outside of our three-dimensional (3D) world. Moreover, quantum fluctuations play an increasingly significant role as the dimensionality of the system is reduced. In 3D systems, Bose-Einstein condensation manifests as a global phase across the system constituents whereas, in one dimension, phase fluctuations prevent pure condensation in finite-temperature systems altogether [17–19]. Nevertheless, the behaviour of phase and density fluctuations have been the focus of intense experimental and global interest [2, 20, 21]. In two dimensions and fewer, the Mermin-Wagner theorem prevents the formation of long-range order, but quasi-long-range order in two-dimensional (2D) interacting bosonic systems, characterised by the binding of vortex-antivortex pairs, is permitted under certain conditions [22–24]. 2D is thus a very special environment where quantum mechanical transitions, the onset of quasi-long-range order, and the effects of quantum fluctuations can be studied together.

As experiments have matured further, strong interest has developed in the out-of-equilibrium behaviour of quantum systems. This has posed questions on universality near critical points and generated theories on the equilibration and thermalisation of isolated quantum sytems [25–33]. This thesis details several advances towards the studies of out-of-equilibrium dynamics in 2D systems and is structured as follows.

We present radiofrequency-dressed potentials in Chapter 2, which form the backbone of experiments detailed within this thesis [34, 35]. These versatile methods of trapping cold atoms are suitable for a range of experimental aims: multiple radiofrequency (RF) fields can produce complex trap geometries, such as double-well potentials [34]; the traps are intrinsically species-selective and mixture components can be separately manipulated [36]; and the traps can be made extremely tight, to realise reduced dimensional systems by 'freezing out' some degrees of freedom [37–40]. Our traps are very smooth and free from the corrugations which usually blight optical trapping methods and are thus well suited to studies of time-dependent or out-of-equilibrium dynamics [37, 39, 41].

In Chapter 3, we discuss the experimental apparatus. We outline the optical cooling and evaporative cooling techniques required to produce gases at ultracold temperatures, as well several methods of magnetic trapping which are used throughout this thesis. We also introduce absorption imaging and subsequent analysis of the atomic distributions.

Experimental apparatuses of this nature are complicated, and attaining long-term, near-optimal performance is challenging. In Chapter 4, we present the application of machine learning methods to optimise our experiment, in particular the stages of laser cooling and evaporative cooling which are necessary to achieve a quantum gas [42]. We benchmark three popular machine learning methods and extract experimental parameters which have the strongest influence on the desired outcome.

In Chapter 5, we present the realisation of a species-selective double well using multiple radiofrequency (MRF)-dressed potentials [36]. We demonstrate manipulations of a mixture of ^{87}Rb atoms in hyperfine states with $F = 1$ and $F = 2$. We show additionally that this mixture is long-lived when RF-dressed, in contrast to recent experiments on this apparatus where a mixture of ^{87}Rb and ^{85}Rb in an RF-dressed potential was found to suffer from fast inelastic loss [43].

In Chapter 6, we follow methods presented elsewhere (reference [37]) to reduce the dimensionality of trapped gases. We perform experiments to investigate and characterise 2D gases in our apparatus and present preliminary results concerning the relaxation of the position and momentum distributions of an out-of-equilibrium 2D system.

Chapter 7 presents the realisation of matter-wave interference for Bose gases in 3D and 2D regimes using MRF-dressed potentials [44]. We investigate the expected scaling of the fringe wavelength, verify coherence of the experimental procedure, and demonstrate the versatility of the MRF-dressed potentials to achieve our research aims; we conclude this chapter with a discussion of phase correlations, including their

time-dependent behaviour as the system equilibrates following a quench.

Finally, Chapter 8 proposes future experimental directions, as well as a reflection on the aforementioned investigations.

2

Multiple-radiofrequency-dressed potentials

We begin by introducing a quantum-mechanical description of the energy levels of an atom. We focus on the structure of alkali atoms, which possess one valence electron, as these are utilised in the experiments detailed within this thesis. We describe the modifications to energy levels which arise under the application of a weak magnetic field and, later, the application of a strong photon field. We introduce the dressed-atom formalism and present RF-dressed potentials as a method of trapping for cold atoms. Finally, we describe the potentials for atoms dressed with multiple RF fields.

2.1 Energy levels of atoms in magnetic fields

Early descriptions of the energy levels of an atom emerged from Einstein's treatment of the interaction of atoms with light [45], as well as from major advancements by Fraunhofer [46], Rydberg [47] and others from the analysis of spectral lines. A quantum-mechanical theory of the atom, devised by Schrödinger in 1926 [48], superseded earlier semi-classical theories proposed by Bohr [49] and Sommerfeld [50], and formalised the energy levels and electron distributions within atoms as eigenvalues $\{E_i\}$ and eigenstates $\{\psi_i\}$ of a Hamiltonian operator $\hat{H}$, respectively.

The most coarse description (*gross structure*) of a single-valence atom is characterised by eigenenergies $E_{n,L}$ which depend on the principal quantum number n and orbital angular momentum quantum number L, which depends only on the valence electron outside the closed inner shells. The eigenstates $\psi_{n,L}$ are solutions to the time-independent Schrödinger equation

$$\hat{H}_{\text{Gross}}\ \psi_{n,L} = E_{n,L}\ \psi_{n,L}\ . \tag{2.1}$$

Observations of sub-structure in atomic emission and absorption spectra led to a refined theory of the atom, which included the interaction of the magnetic moment of the electron proportional to its intrinsic spin $\mathbf{S}$ with its orbital angular momentum, as well as the Darwin term and relativistic mass corrections [51]. The collective effect of these processes is encapsulated by the addition of the term $\beta\mathbf{L}\cdot\mathbf{S}$ to $\hat{H}_{\text{Gross}}$, where β is an atom-, n- and L-specific correction, to form the *fine structure* Hamiltonian

$$\hat{H}_{\text{Fine}} = \hat{H}_{\text{Gross}} + \beta\mathbf{L}\cdot\mathbf{S}\ . \tag{2.2}$$

We use $\mathbf{L}$ and $\mathbf{S}$, which are appropriate for the LS-coupling scheme for angular momenta, although these operators and the corresponding quantum numbers do not

need to be written in upper case for a single electron [1]. In this regime, the Hamiltonian in equation 2.2 is diagonal in the basis of eigenstates of the total electronic angular momentum $\mathbf{J} = \mathbf{L} + \mathbf{S}$, with eigenstates $|J, m_J\rangle$, where m_J is the eigenvalue of J_z, which corresponds to the projection of $\mathbf{J}$ onto a quantisation axis. Energy scales for gross structure are of the order $\alpha^2 m_e c^2$, where $\alpha \approx 1/137$ is the fine structure constant, m_e is the electron mass and c is the speed of light in vacuo, and of order $\alpha^4 m_e c^2$ for fine structure effects.

The interaction of the nuclear magnetic moment, which is proportional to the nuclear spin $\mathbf{I}$, with the magnetic field produced by the electron cloud proportional to $\mathbf{J}$, leads to further substructure [52]. This *hyperfine structure* arises from the Hamiltonian

$$\hat{H}_{\text{Hyperfine}} = \hat{H}_{\text{Gross}} + \beta \mathbf{L} \cdot \mathbf{S} + A \mathbf{I} \cdot \mathbf{J} \ , \tag{2.3}$$

where A is the hyperfine structure constant for a specific atom and energy level. This Hamiltonian is diagonalised by eigenvectors described by the total angular momentum $\mathbf{F}$, where $\mathbf{F} = \mathbf{I} + \mathbf{J}$, and its projection onto a quantisation axis m_F. These eigenvectors are labelled by $|F, m_F\rangle$.

We now consider the application of a weak magnetic field. The total magnetic moment of an atom $\boldsymbol{\mu}$ is the contribution from the electronic $\boldsymbol{\mu}_{\text{e}}$ and nuclear moments $\boldsymbol{\mu}_{\text{N}}$, such that

$$\boldsymbol{\mu} = \boldsymbol{\mu}_{\text{e}} + \boldsymbol{\mu}_{\text{N}} \ , \tag{2.4}$$

where $\boldsymbol{\mu}_{\text{e}} = -g_J \mu_B \mathbf{J}$, $\boldsymbol{\mu}_{\text{N}} = g_I \mu_N \mathbf{I}$ and g_J and g_I are the Landé g-factors for the electron and nuclear angular momenta, respectively, which arise from the projection of these angular momenta onto a quantisation axis [52]. The magnitude of the nuclear magneton $\mu_N = e\hbar/2m_p$ is approximately m_e/m_p that of the Bohr magneton μ_B and,

[1] The LS-coupling scheme is more generally applicable for systems with multiple valence electrons in light atoms with atomic number lower than 30.

consequently, the nuclear contribution to the magnetic moment is neglible[2], although the nuclear moment determines the constant A in equation 2.3. The interaction of an atom with magnetic moment $\boldsymbol{\mu}$ and a magnetic field $\mathbf{B}$, for a weak magnetic field, is thus described by the Zeeman Hamiltonian

$$V = -\boldsymbol{\mu} \cdot \mathbf{B} \ = g_J \mu_B \mathbf{J} \cdot \mathbf{B} \ . \tag{2.5}$$

We include the Zeeman contribution to the full Hamiltonian, which is given by

$$\hat{H} = \hat{H}_{\text{Gross}} + \beta \mathbf{L} \cdot \mathbf{S} + A \mathbf{I} \cdot \mathbf{J} + \underbrace{g_J \mu_B \mathbf{J} \cdot \mathbf{B}}_{\text{perturbation}} \ . \tag{2.6}$$

In the low field-regime, where $\mu_B B \ll A$, the Zeeman term in this Hamiltonian can be treated as a perturbation and the eigenstates of the system are still well described in the $|F, m_F\rangle$ basis. For small field strengths, where the second-order Zeeman term is negligible, the energies of the hyperfine Zeeman states are given by $m_F g_F \mu_B B$, where $B = |\mathbf{B}|$ and g_F describes the projection of $\mathbf{J}$ onto $\mathbf{F}$.

2.1.1 Trapping atoms in magnetic fields

In the low-field regime, atoms in a spatially-varying, static magnetic field $\mathbf{B}(\mathbf{r})$ have eigenenergies $m_F g_F \mu_{\text{B}} B(\mathbf{r})$, corresponding to the Zeeman substates $|m_F\rangle$ [52], where $B(\mathbf{r}) = |\mathbf{B}(\mathbf{r})|$ for position $\mathbf{r} = (x, y, z)$ [55]. The eigenenergies of the substates do not vary with the direction of $\mathbf{B}(\mathbf{r})$, as the atom's dipole moment remains aligned with the field as it moves, and thus they only depend on the magnitude of the field; this is the *adiabatic approximation* [52]. Consequently, the energy shift due to the Zeeman effect forms a spatially-varying potential which can confine atoms. The weak-field seeking states, for which $g_F m_F > 0$, can be trapped at local minima of $B(\mathbf{r})$. For

[2]The nuclear contribution leads to small corrections to g_F which are important in high-precision spectroscopic measurements [53] and in some magnetic trapping schemes [54].

example, in the magnetic quadrupole field described by

$$\mathbf{B}\,(x,y,z) = B'(x\hat{\mathbf{e}}_x + y\hat{\mathbf{e}}_y - 2z\hat{\mathbf{e}}_z)\ , \tag{2.7}$$

with field gradient B' and Cartesian unit vectors $\{\hat{\mathbf{e}}_x, \hat{\mathbf{e}}_y, \hat{\mathbf{e}}_z\}$, atoms are confined around the node at the origin. Figure 2.1 (left) illustrates the Zeeman eigenenergies as a function of vertical displacement below the node of a magnetic quadrupole field.

2.2 The dressed-atom formalism

When an atom is irradiated by a strong photon field of angular frequency ω, in the absence of coupling, the eigenstates can be described by the outer product of states of the atom with those of the photon field, and are thus solutions to

$$\hat{H} = \hat{H}_{\text{atom}} \otimes \hat{H}_{\text{field}}\ , \tag{2.8}$$

where $\hat{H}_{\text{atom}}$ and $\hat{H}_{\text{field}}$ are the Hamiltonians for the atom and RF field, respectively [56]. The eigenenergies are those which solve the time-independent Schrödinger equation

$$(\hat{H}_{\text{atom}} + \hat{H}_{\text{field}})\,|F, m_F\rangle \otimes |N\rangle = (m_F g_F \mu_B |B(\mathbf{r})| + N\hbar\omega)\,|F, m_F\rangle \otimes |N\rangle\ , \tag{2.9}$$

where N is the occupation of Fock state $|N\rangle$ of the RF field. This eigenvalues of this Hamiltonian have the structure of a 'ladder', where the Zeeman substates of the atom are repeated at intervals set by the Fock states of the RF field, as depicted in figure 2.1 (right). Spontaneous emission proceeds at a very slow rate and is not considered in the description of the eigenstates.

The Hamiltonian (equation 2.9) is modified to include the interaction $\hat{H}_{\text{interaction}}$

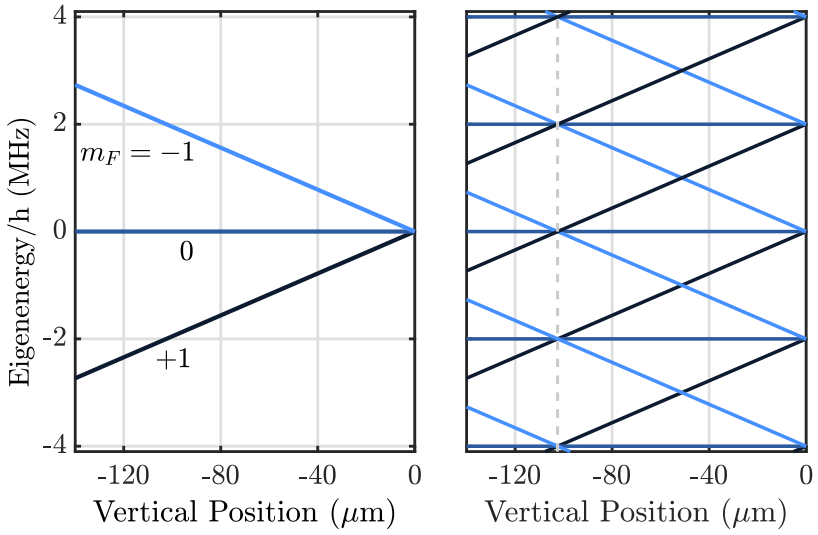

Figure 2.1: Left: Zeeman substates of a ^{87}Rb atom with $F = 1$ in a weak magnetic field. States with $m_F = 1, 0, -1$ are indicated by dark blue, blue and light blue colours, respectively. Right: states of the combined atom-photon system, in the absence of coupling. The dashed line indicates the spatial location where the atom is resonant with the 2 MHz RF field. The magnetic field has a gradient of 139.5 G cm^{-1} in both plots.

between the atoms and the field:

$$\hat{H} = \hat{H}_{\text{atom}} + \hat{H}_{\text{field}} + \hat{H}_{\text{interaction}} \ . \tag{2.10}$$

The eigenstates of equation 2.10 are now considered further in the context of traps for cold atoms.

2.3 RF-dressed potentials

The dressed-atom Hamiltonian (equation 2.10) can be simplified using several approaches to yield approximate solutions. In [57, 58], the Hamiltonian is reduced to only include terms which most strongly couple the atomic species to the quantised components of the RF field; this is equivalent to making the Rotating Wave approximation (RWA) [52]. For atoms with negative g_F, coupling arises from the σ^--polarised components of the dressing field, whereas atoms with positive g_F cou-

ple to σ^+-polarised components. The interaction couples states within manifolds of constant $N' = \mathrm{sgn}(g_F)m_F + N$. Dressed states within each manifold are labelled by quantum number $\tilde{m}_F$, which takes values [-F, $-F+1$, ... , F], and describes whether eigenenergies form a potential minimum ($\tilde{m}_F > 0$) or a maximum ($\tilde{m}_F < 0$) at the position of the RF resonance. The spectrum of dressed eigenstates is thus described by $|N, \tilde{m}_F\rangle$.

As also presented in [57], the Hamiltonian can be viewed in a semi-classical perspective, where the quantised atomic eigenstates interact with a classical RF field. In this picture, the applied RF, σ^- circularly polarised around $\hat{\mathbf{e}}_z$, takes the form

$$\mathbf{B}_{\mathrm{RF}}(\mathbf{r}, t) = B_{\mathrm{RF}} \left[\cos(\omega t)\hat{\mathbf{e}}_x - \sin(\omega t)\hat{\mathbf{e}}_y\right], \tag{2.11}$$

where $B_{\mathrm{RF}} = |\mathbf{B}_{\mathrm{RF}}|$ is the amplitude of the field. Similarly, a field linearly polarised along $\hat{\mathbf{e}}_x$ is described by

$$\mathbf{B}_{\mathrm{RF}}(\mathbf{r}, t) = B_{\mathrm{RF}} \cos(\omega t)\hat{\mathbf{e}}_x \ . \tag{2.12}$$

After applying the RWA, via either of the two approaches described above, and incorporating gravity, the eigenenergies of a dressed atom at position $\mathbf{r} = (x, y, z)$ are

$$U(\mathbf{r}) = \tilde{m}_F \hbar \sqrt{\delta(\mathbf{r})^2 + \Omega(\mathbf{r})^2} + N'\hbar\omega + Mgz \tag{2.13}$$

where $\Omega(\mathbf{r})$ is the Rabi frequency of coupling to the dressing field, which depends on the polarisation of the RF field, M is atomic mass, g is gravitational acceleration, z is vertical position and $\delta(\mathbf{r}) = \omega - g_F \mu_{\mathrm{B}} B(\mathbf{r})/\hbar$ is the angular frequency detuning between the applied RF field and the Zeeman splitting of the atoms [39, 40]. The RF-dressed eigenstates have avoided crossings where the RF field is resonant with

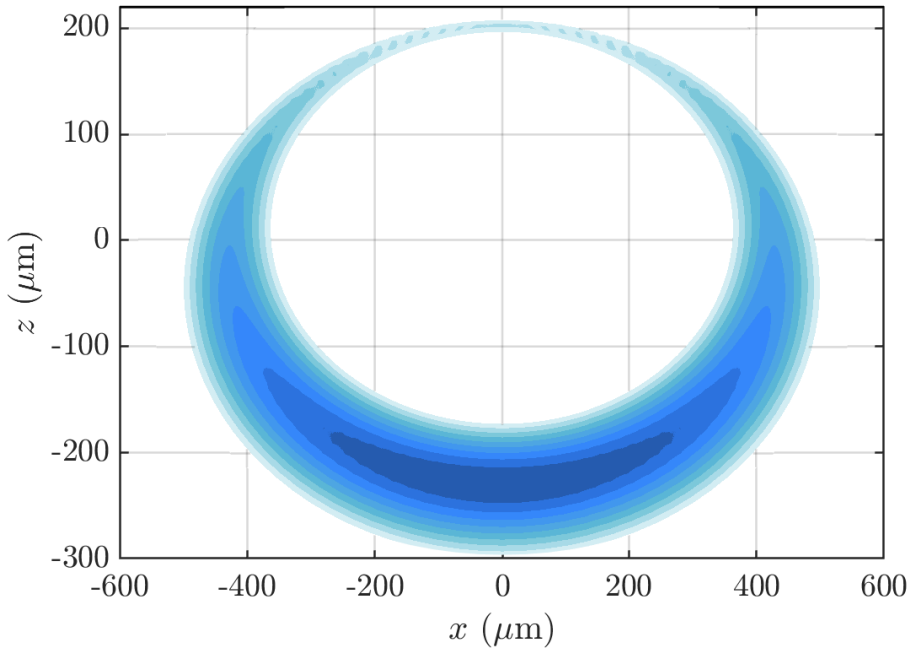

Figure 2.2: Schematic of an RF-dressed potential trap, in the $x - z$ plane, for ^{87}Rb with $F = 1$ and a single RF field at 3 MHz with σ^- polarisation and a magnetic field gradient $B' = 100\,\mathrm{G\,cm^{-1}}$. We choose the RF field amplitude to correspond to a Rabi frequency of $\Omega_0/2\pi = 500\,\mathrm{kHz}$. Lower potential energies are indicated by darker colours. As a consequence of gravity, atoms are trapped at the bottom of the shell and anisotropic confinement strengths leads to pancake-shaped trapped gases.

the Zeeman splitting of the atomic states, which occurs at positions $\mathbf{r}$ where

$$|g_F|\mu_{\mathrm{B}}B(\mathbf{r}) = \hbar\omega \ , \tag{2.14}$$

is satisfied. These positions are illustrated for the uncoupled (figure 2.1 b), dashed) and coupled cases (figure 2.4, dashed). The avoided crossings form potential wells in which atoms with $\tilde{m}_F > 0$ can be trapped, provided the coupling to the RF field is sufficiently strong that their dipole moment follows adiabatically and Landau-Zener loss processes are slow [59,60]. The static magnetic quadrupole field of equation 2.7 has isomagnetic surfaces defined by an effective radius $r_e(\mathbf{r})$ where

$$r_e(\mathbf{r}) = \sqrt{x^2 + y^2 + 4z^2} = r_0 \ , \tag{2.15}$$

which define an oblate spheroid of semi-axes r_0 and $r_0/2$ along the horizontal and vertical axes, respectively. The resonance condition of equation 2.14 is thus satisfied on the surface of an oblate spheroid centered on the origin, forming a 'shell' on which atoms are confined, as illustrated by figure 2.2.

A position-dependent coupling $\Omega(\mathbf{r})$ arises from the orientation of $B(\mathbf{r})$ with respect to the uniform RF field polarisation. For circularly polarised RF fields, the effective Rabi coupling takes the form

$$\Omega(\mathbf{r}) = \frac{|g_F|\mu_B B_{\mathrm{RF}}}{2\hbar}\left[1 - \frac{2z}{r_e(\mathbf{r})}\right] \ , \tag{2.16}$$

where the maximum Rabi frequency $\Omega_0 = |g_F|\mu_B B_{\mathrm{RF}}/\hbar$ occurs at the bottom of the spheriod [34]. Similarly, for an RF field linearly polarised along $\mathbf{e}_x$, we find

$$\Omega(\mathbf{r}) = \frac{|g_F|\mu_B B_{\mathrm{RF}}}{2\hbar}\left[\frac{\sqrt{y^2 + z^2}}{r_e(\mathbf{r})}\right] \ , \tag{2.17}$$

with a maximum Rabi coupling of $\Omega_0 = |g_F|\mu_B B_{\mathrm{RF}}/2\hbar$. We assume $\omega \gg \Omega_0$ and consider small detunings $|\delta| \ll \omega$ such that the RWA can be invoked. Under the influence of gravity, atoms are trapped a small displacement from the point of maximum coupling to the RF field, thus the trap centre is located at $(0, 0, -R)$, where

$$R = \frac{r_0}{2}\left(1 + \frac{\epsilon}{\sqrt{1-\epsilon^2}}\frac{\Omega_0}{\omega}\right) \quad , \tag{2.18}$$

and where $\epsilon = Mg/(2m_F\hbar\alpha)$ and $\alpha = |g_F|\mu_B B'/\hbar$ [37]. For small perturbations about the trap centre, for circularly polarised RF fields, we find the angular frequencies of radial and axial oscillations to be

$$\omega_r = \sqrt{\frac{g}{4R}}\left(1 - \frac{m_F\hbar\Omega_0}{2MgR}\sqrt{1-\epsilon^2}\right)^{1/2} \quad , \tag{2.19}$$

and

$$\omega_z = 2\alpha\sqrt{\frac{m_F\hbar}{M\Omega_0}}\left(1-\epsilon^2\right)^{3/4} \quad , \tag{2.20}$$

respectively [37]. We calibrate the gradient of the magnetic quadrupole field B' by performing trap frequency measurements in the shell trap. This is achieved by applying an impulse to the trapped cloud, via a jump in quadrupole field strength, and observing the subsequent centre-of-mass oscillation, as shown in figure 2.3 (upper). We extract the oscillation frequency as we vary the current through the magnetic quadrupole coils, as shown in figure 2.3 (lower), and extract the field gradient as $B'/\mathrm{A} = 1.18(0.01)\ \mathrm{G\,cm^{-1}\,A^{-1}}$ using equation 2.20.

Calibration of the RF amplitude and hence Ω_0 is performed using RF spectroscopy, as detailed in references [34,58,61–63]. Figure 2.4 illustrates the dressed eigenenergies for the cases of a ^{87}Rb atom with angular momentum $F = 1$ and $F = 2$, respectively, for a linearly polarised dressing field of frequency 2.0 MHz and amplitude $\Omega_0/2\pi = 200$ kHz, with a magnetic quadrupole field of gradient $B' = 139.5$ G cm^{-1}. States

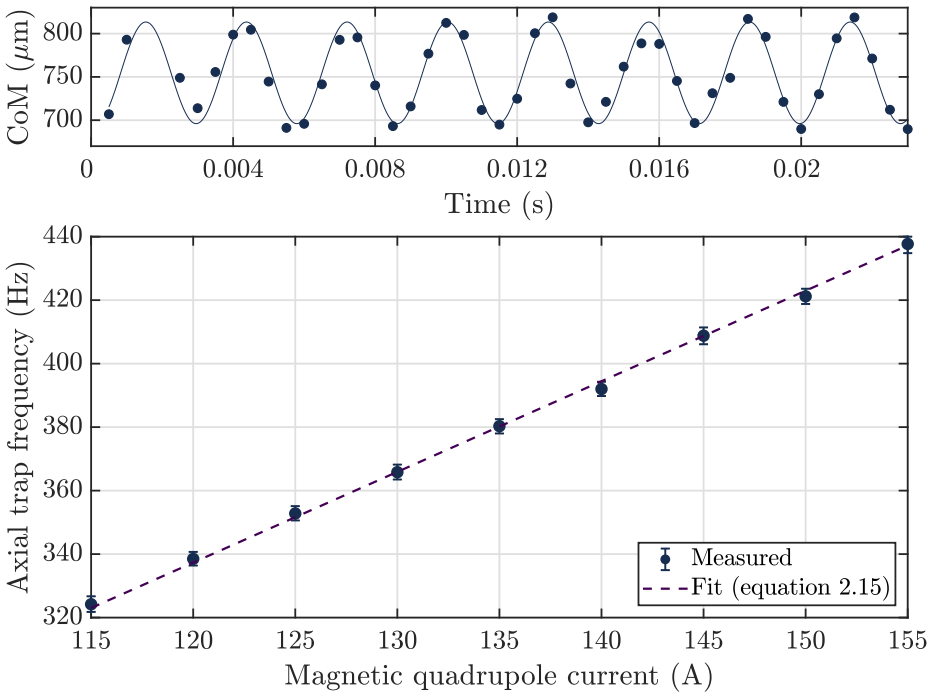

Figure 2.3: Calibration of the magnetic quadrupole field gradient. Upper: by applying a sudden jump in the magnetic quadrupole field, we induce an axial (z) centre-of-mass oscillation. The oscillation frequencies are extracted via a fitting procedure. Lower: the experiment is repeated over a range of currents in the current-carrying coils which produce the quadrupole field. We fit the data with equation 2.20 to find the field gradient $B'/\mathrm{A} = 1.18(0.01)\ \mathrm{G\,cm^{-1}\,A^{-1}}$.

with $\tilde{m}_F = 1$ are marked in bold. U has a local minimum near $\delta(\mathbf{r}) = 0$, as indicated by the dashed lines in figure 2.4.

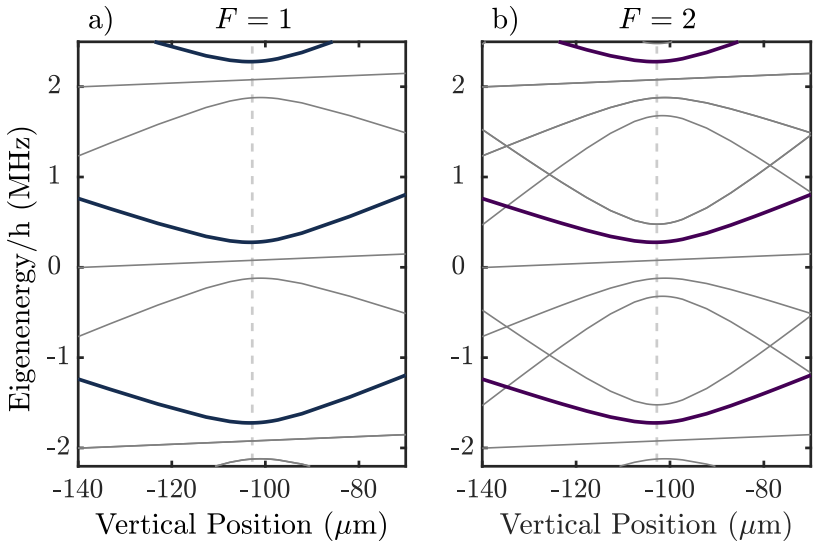

Figure 2.4: Eigenenergies of the RF-dressed states as a function of vertical position, z, for ^{87}Rb atoms with $|F = 1\rangle$ (a) and $|F = 2\rangle$ (b). The atoms are dressed by a linearly polarised, 2 MHz RF field with a corresponding Rabi frequency of $\Omega_0/2\pi = 200$ kHz. The eigenstates with $\tilde{m}_F = 1$ are emphasized in bold and the zero of energy is arbitrary. A magnetic quadrupole field of gradient of $B' = 139.5$ G cm^{-1} is used for both plots. Dashed lines indicate the positions where the resonance condition (eq 2.14) is satisfied.

Simulation of the eigenstates provides a useful diagnostic tool and is used to guide choices of parameters for experiments involving double-well potentials, detailed later in Chapters 5 and 7. We simulate the RF-dressed potentials using software developed by Elliot Bentine [57] and a formalism developed by Dimitris Trypogeorgos [64]. Eigenenergies of RF-dressed eigenstates are found via numerical integration of the time-dependent Schrödinger equation and utilise Floquet theory. Source code, which is used to simulate the RF-dressed eigenenergies throughout this thesis, is located in *https://bitbucket.org/footgroup/crfap/src/master/*.

2.3.1 Species-selectivity

The eigenenergies depend intrinsically on the magnetic nature of the atom, via the sign or magnitude of g_F. The magnitude of g_F determines the spatial location of avoided crossings, thus multiple RF components can be used to form spatially coincident

traps or to independently manipulate atoms of differing $|g_F|$ [43, 54, 65, 66]. The sign of g_F determines the handedness of the circularly polarised RF field which couples the Zeeman substates, as detailed in section 2.3. If a mixture contains atoms of differing $\mathrm{sgn}(g_F)$, each species couples to different polarisation components of an applied RF field, providing a means to manipulate each species independently [67]. This is also true for two different hyperfine states of the same species. For example, a mixture of ^{87}Rb atoms in the $F = 1$ and $F = 2$ hyperfine levels, which have $g_F = -1/2$ and $1/2$, respectively, can be individually manipulated by controlling the amplitudes of σ^-- and σ^+-polarised components of the applied RF field [65]. To highlight this capability, the term "species-selective potential" will be used for the rest of the manuscript, even though the experiments presented here are performed with two internal states of ^{87}Rb; for instance, in Chapter 5, we realise a species-selective double-well potential using multiple RF fields [36]. In other works, the species-selective nature of RF-dressed potentials has been exploited to realise atom interferometers [54, 68, 69].

2.4 Multiple-radiofrequency-dressed potentials

Complex potentials, such as double wells, can be engineered by increasing the number of dressing RF frequencies [34, 58, 65]. To describe the MRF-dressed potential, we express the dressing field in a semi-classical formalism as

$$\begin{aligned}\mathbf{B}_{\mathrm{RF}} &= \sum_{i=1}^{N} B_i\Big(\cos(\omega_i t)\,\hat{\mathbf{e}}_x - \sin(\omega_i t)\,\hat{\mathbf{e}}_y\Big) + A_i\Big(\cos(\omega_i t)\,\hat{\mathbf{e}}_x + \sin(\omega_i t)\,\hat{\mathbf{e}}_y\Big) \\ &= \sum_{i=1}^{N} \Big(B_i + A_i\Big)\cos(\omega_i t)\,\hat{\mathbf{e}}_x - \Big(B_i - A_i\Big)\sin(\omega_i t)\,\hat{\mathbf{e}}_y \ ,\end{aligned} \tag{2.21}$$

with components $i = 1, 2, ...N$, at angular frequencies ω_i [57]. A_i and B_i correspond to the circularly polarised RF field amplitudes that couple states with $F = 1$ and $F = 2$, respectively. The sum and difference of A_i and B_i correspond to the magnitudes of

the linearly polarised fields aligned along $\hat{\mathbf{e}}_x$ and $\hat{\mathbf{e}}_y$, respectively, which are produced by current-carrying coils, as illustrated in Chapter 3, figure 3.8. A full quantum mechanical treatment of the polychromatic dressing field and the corresponding dressed eigenstates is presented in [58, 70].

In this thesis, we present the realisation of a species-selective double-well potential. To first create a double-well potential, we apply three RF components, with frequencies separated by a common fundamental frequency. In figure 2.5 a), we illustrate a double-well potential for atoms with $F = 1$ using linearly-polarised RF fields with frequencies $\{\omega_i/2\pi\} = \{1.8\,\text{MHz}, 2\,\text{MHz}$ and $2.2\,\text{MHz}\}$ and amplitudes $\{A_i + B_i\}$ $= \{326\,\text{mG}, 243\,\text{mG}$ and $440\,\text{mG}\}$, which correspond to Rabi frequencies $\{114\,\text{kHz}, 85\,\text{kHz}$ and $154\,\text{kHz}\}$. Each RF field component i creates an avoided crossing at the position $\mathbf{r}_i$ where the species-dependent resonance condition $\hbar\omega_i = |g_F|\mu_\text{B}B(\mathbf{r}_i)$ is satisfied, which is indicated by the dashed lines. The RF field at 2 MHz, in this case, defines the 'barrier' of the double-well potential. States in which atoms are trapped, in this case $\tilde{m}_F = 1$, are indicated by thick lines (blue). The trap minimum for the atoms under the influence of gravity is slightly displaced from the spatial location of the avoided crossing, similarly to the single-RF case defined in section 2.3. Figure 2.5 b) illustrates the potential when the 2 MHz field amplitude is increased to 374 mG, which corresponds to a Rabi frequency of 131 kHz, to form a broad, single-well potential.

Additional RF components can be applied to control the polarisation of the field, which can be used to manipulate species of differing $\text{sgn}(g_F)$ independently, or to create spatially coincident potentials for species with differing $|g_F|$ [65]. Extending the schemes to many rfs may also realise lattice potentials [71].

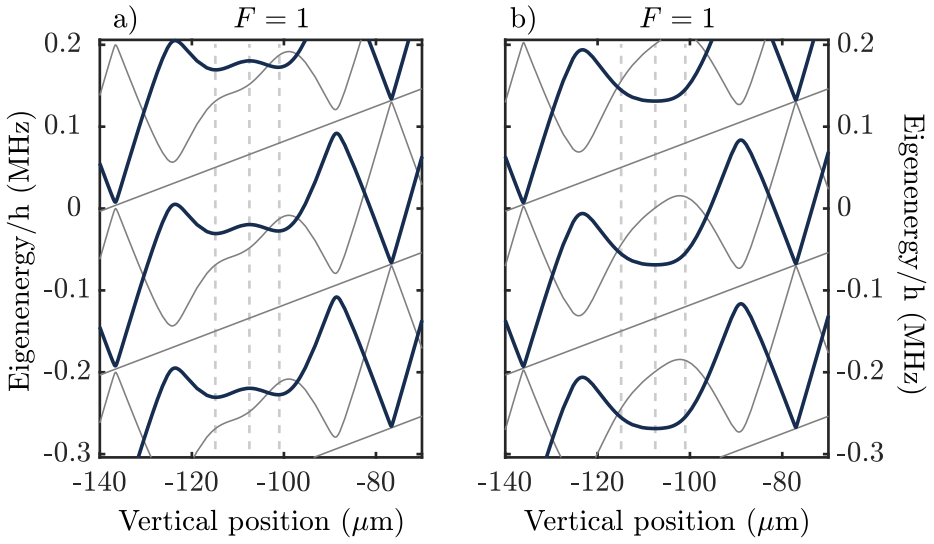

Figure 2.5: Eigenenergies of an ^{87}Rb atom with $F = 1$ when dressed with three linearly polarised RF components at frequencies 1.8 MHz, 2.0 MHz and 2.2 MHz with amplitudes 326 mG, 243 mG and 440 mG (a) and 326 mG, 131 mG and 440 mG (b). Trapped states for which $\tilde{m}_F = 1$ are indicated by the bold lines. Spatial locations where each RF field component is resonant are indicated by dashed lines. A quadrupole gradient of 133.4 G cm^{-1} is used for both plots.

2.5 Two-dimensional potentials

The confinement provided by the shell trap is intrinsically anisotropic: atoms are tighly confined along $\hat{\mathbf{e}}_z$, with axial trap frequencies of order 500 Hz and upwards, whereas radial confinement is set by the variation in $\Omega(\mathbf{r})$ and Mgz which are comparitively weak and produce radial trap frequencies of order 20 Hz. Consequently, distributions of trapped atoms form pancake-like geometries, where the axial extent is very small (<1 µm) and the radial extent is much larger (∼5 µm). For a thermal gas, the aspect ratio of the cloud is given by the relative harmonic oscillator lengths a_z/a_r, where $a_{r,z} = \sqrt{\hbar/M\omega_{r,z}}$. Further compression can be achieved by reducing Ω_0 or by increasing B' [37, 39]. For experiments detailed within Chapter 6, we use $\Omega_0/2\pi = 38$ kHz and $B' = 195$ G cm^{-1} to realise trap frequencies of 1.5 kHz (axial) and 27 Hz (radial).

For low temperature gases in these highly anisotropic potentials, the separation

between axial harmonic oscillator eigenstates exceeds the thermal energy, such that $\hbar\omega_z \gg k_B T$. The axial degree of freedom is consequently frozen out to realise a quasi-2D gas [24,37,72]. Experiments concerning 2D Bose gases, including a detailed description of a gas in this regime, are presented in Chapter 6.

2.6 Conclusion

In this chapter, we have introduced a description of the eigenstates for a bare alkali atom, which incorporated fine structure and hyperfine structure effects. We have extended this description to include atoms in weak static magnetic fields or those dressed by strong RF fields. The eigenenergies of RF-dressed atoms may form trapping potentials, and additional RF components extend the range of possible trap geometries to include double-well potentials or broad, flat-bottomed wells. We have introduced features of RF-dressed potentials which can be exploited to manipulate species with differing magnetic nature, or to compress a gas into the 2D regime, both of which are revisited in experiments detailed in later chapters.

3

The experimental apparatus

Much of the apparatus described within this chapter is typical of a cold-atom experiment. Atoms are first laser-cooled in a Magneto-Optical Trap (MOT) [52] and are then transported to an ultra-high vacuum (UHV) glass cell using an array of current-carrying coils mounted on a mechanical translation stage. Next, the atoms are confined by a sequence of magnetic trapping potentials and cooled further by forced evaporation to form an ultracold thermal or degenerate gas. The experimental setup has been described in greater detail in several theses, in particular references [57, 61, 73]. This chapter provides a summary of the operation of the experiment and additional detail on recent improvements. We first introduce upgraded laser systems, which are used for laser cooling and imaging atomic gases, as well as Light-Induced Atomic Desorption (LIAD), which was used as a means of improving sequence repetition rate. We detail the implemention and operation of new RF-generating hardware, which is used throughout to form RF-dressed potentials. Finally, we present the optical apparatus and cameras used to image the atomic distributions.

3.1 The experimental sequence and apparatus

To set the stage for the following sections, we first provide a broad overview of the experimental sequence. Atoms are trapped and cooled using an arrangement of lasers and magnetic fields in a MOT. To improve the rate at which we cool atoms in this stage, we illuminate the chamber with Ultra-Violet (UV) light, which increases the vapour pressure of ^{87}Rb in the chamber. We then cool the atoms further in a colder Magneto-Optical Trap (cMOT), prior to transporting the atoms to an UHV glass cell using magnetic field-producing coils mounted on a translation stage. The atoms are confined by a sequence of magnetic traps, including a magnetic quadrupole trap, a Time-Averaged Orbiting Potential (TOP) trap, a Time-Averaged Adiabatic Potential (TAAP) trap and RF-dressed potentials. Finally, we extract properties of the atomic gas using an absorption imaging protocol.

3.1.1 The Magneto-optical Trap

Pioneering work led by Phillips, Cohen-Tannoudji and Chu (Nobel Prize 1997), as well as many others, led to major developments in the laser cooling of atomic vapours [74, 75]. Today, laser cooling is a necessary step in the production of degenerate gases and other cold-atom systems such as in atomic clocks [76] or ions in state-of-the-art quantum computing schemes [77].

In the experimental apparatus detailed here, laser cooling is the first step in producing a degenerate gas. This takes place in a single-window vacuum chamber, at a pressure of approximately 1×10^{-9} torr, which contains four mirrors arranged as an inverted pyramid [79], as shown in figure 3.1. The chamber and mirrors are illuminated with a single laser beam with a power of approximately 450 mW and collimated to a $1/e^2$ waist of 4 cm. The laser beam is bichromatic: 80% of the total intensity is light detuned by $\Delta = -22$ MHz from the $F = 2$ to $F' = 3$ transition in the ^{87}Rb

Figure 3.1: Schematic of the vacuum system. Atoms are first laser cooled in a pyramidal MOT (left) before transport to a UHV glass cell (right) using current-carrying coils mounted on a moving translation stage (not shown for clarity). Atoms are confined by a sequence of magnetic trapping potentials formed by static and RF fields produced by current-carrying coils (orange) which surround the UHV glass cell.

D2 manifold (cooling light) [80], where F' is the total atomic angular momentum quantum number of the excited state, and provides the radiation forces which cool the atoms [52]. Due to the internal structure of the ^{87}Rb atom, off-resonant excitation may drive atoms into a dark state, in which they are no longer resonant with the cooling light. To avoid this, the remaining 20% of the total intensity comprises (repump) light resonant with the $F = 1$ to $F' = 2$ transition in the ^{87}Rb D2 manifold, which pumps 'dark' atoms with $F = 1$ back into the cooling cycle. Figure 3.2 illustrates the energy levels within the ^{87}Rb D2 manifold, as well as the transitions used for optical cooling in this experiment. The laser apparatus to produce these optical frequencies is detailed in section 3.1.3.

The pyramidal arrangement of mirrors, shown in the leftmost chamber of figure 3.1, produces light incident along all Cartesian axes, which act to slow the atoms along all translational degrees of freedom. A pair of anti-Helmholtz current-carrying

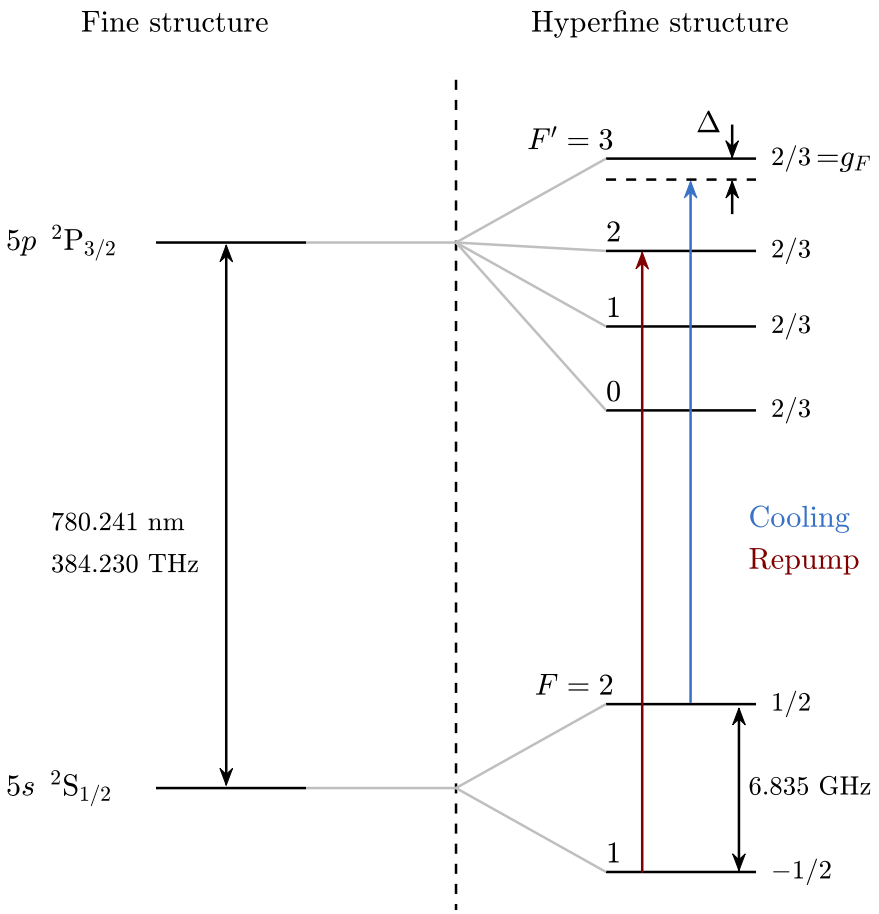

Figure 3.2: Energy levels of the ^{87}Rb D2 manifold [78]. We illustrate the fine structure (left) and hyperfine structure (right) levels, in the absence of an applied magnetic field. Levels are appropriately labelled with their term symbols and total angular momentum quantum numbers. The g_F factors of each hyperfine level are displayed (right). The optical transitions used for cooling (blue) and repump (red) in this apparatus are labelled, as well as the ground state hyperfine splitting of approximately 6.835 GHz. Furthermore, the $F' = 2$ and $F' = 3$ levels are separated by approximately 266 MHz. The cooling light is detuned from resonance by $\Delta = -22$ MHz in the typical operation of the MOT. The separations in energy are not illustrated to scale.

coils, which produce a magnetic quadrupole field, add spatial confinement to the radiation forces to form a MOT [52].

Room-temperature atoms are loaded into the MOT from background vapour, which is dispensed from rubidium dispensers located within the chamber. The rate of loading, as well as the maximum number of atoms cooled and trapped in the MOT, depends on many experimental parameters, including: the detuning from resonance of the cooling light and repump light, the gradient of the magnetic field and the vapour pressure of ^{87}Rb. The vapour pressure of ^{87}Rb in the MOT can be increased temporarily by the application of UV light, as we detail in section 3.1.2, which significantly reduces the time required to load a threshold number of atoms into the MOT.

3.1.2 Light-Induced Atomic Desorption

LIAD is a phenomenon where the pressure of an atomic vapour can be increased by the illumination of a surface with light, typically of UV wavelengths [81]. This effect is of great utility to a cold-atom experiment: UV light can be turned on when an increase in vapour pressure is desirable, for instance when loading a MOT. However, a higher vapour pressure causes atom loss in subsequent stages of the experiment, such as magnetic transport or probing a quantum gas. To avoid these issues, LIAD is turned off when performing tasks requiring lower vapour pressure. This effect has been observed in K [82], Rb [83, 84], Na [85], Li [86], as well as alkaline earth elements [87]. The mechanisms responsible for the increase in vapour pressure are still disputed: several investigations attribute the effect to an atomic analogue of the photoelectric effect [82], whereas others have suggested diffusion mechanisms [88].

There exists only one viewport into the MOT chamber, which constrains the delivery of UV light. Furthermore, to counter the effect of eddy currents produced by a sudden increase in the strength of the magnetic quadrupole field during magnetic

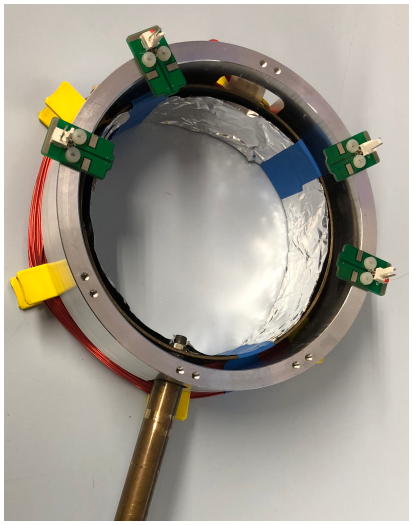

Figure 3.3: The dummy coil and the aluminium LIAD LED mounting ring. The LEDs face downwards, slightly protruding into the ring.

transport, a circular 'dummy' coil is mounted above the viewport, further obstructing access. The laser beam for the MOT passes through the centre of this circular coil. To avoid reducing the incident power of this beam, and given the optical access constraints imposed by the chamber, the UV LEDs used for LIAD are mounted on small PCBs (Printed Circuit Boards), which are in turn mounted on a ring which is fixed to the dummy coil above the MOT chamber, as shown in figure 3.3. The LEDs protrude within the locus of the coil by only a few mm and thus avoid any occlusion of the MOT laser beam.

There are two types of LED mounted on the ring, which are detailed in table 3.1.2. LEDs are configured such that, looking inwards, the positive terminal is on the left, and are connected in series, such that any LED failure will be immediately indicated by a sharp reduction in MOT loading rate. Schematics for the PCBs on which LEDs are mounted are located in *https://github.com/ajbarker93/circuits*.

Applying LIAD to a fully-loaded MOT may cause an increase in atom number, as a consequence of the increase in ^{87}Rb partial pressure. This is illustrated in figure 3.4 (a) for the case of illuminating a fully-loaded MOT with two 365 nm LEDs at 0.6 A.

Name	Wavelength (nm)	Maximum current (A)	Luminosity	Throw angle (deg)
TSLC N3535U-UNL1	385	1	525 mW @ 0.5 A	125
Nichia NCSU276AT	365	0.7	780 mW @ 0.5 A	130

Table 3.1: UV LEDs used in LIAD apparatus.

The LEDs are turned on at t_0 and the atom number rises by $\Delta N_0 \sim 5 \times 10^8$ (a 15% increase). After turning the LEDs off at t_1, the number falls exponentially to $\Delta N_1 \sim 1 \times 10^8$ below that of an unilluminated, fully-loaded MOT. The number is slowly restored to the steady-state atom number of a MOT in the absence of LIAD illumination. This behaviour has been observed in many contexts and is described by a phenomenological model presented by reference [83]. The various stages can be analysed to extract rate constants, which may vary with the wavelength and intensity of the UV light.

In our context, LIAD is most useful for reducing the time required to trap and cool a threshold number of atoms in the MOT. In this apparatus, the threshold is around 3.3×10^9 atoms, which is set by the number of atoms required to produce a Bose-Einstein condensate (BEC) in subsequent experimental stages. Consequently, without LIAD, the MOT must be loaded for 20 s . To realise higher experimental repetition rate, our figure of merit is not the increase in atom number that arises when LIAD is applied to a fully-loaded MOT but rather the time constant of loading a MOT from empty. We turn on the LIAD LEDs 0.2 s before loading the MOT and turn them off 0.1 s before the cMOT stage, which provides sufficient time for the vapour pressure to fall and not cause atom loss during the subsequent stages of the experiment.

We fit the loading curves shown in figure 3.4 (b) with a curve of the form

$$N(t) = N_{\mathrm{bg}} + N_0 \left(1 - e^{-t/\tau}\right) \ , \tag{3.1}$$

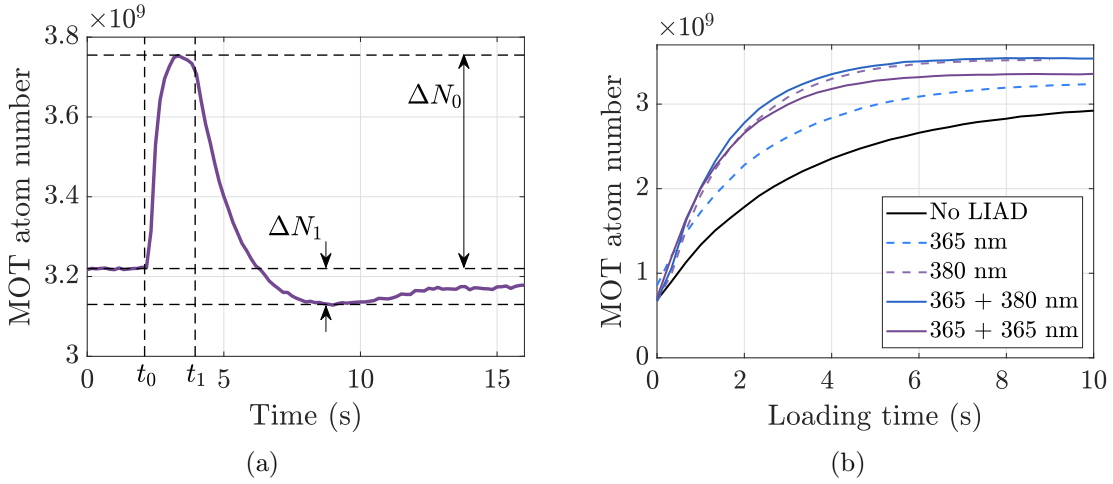

Figure 3.4: Effects of illuminating a MOT with UV light. (a) The LEDs are turned on at t_0 and turned off again at t_1. The increase in atom number ΔN_0 and temporary reduction in atom number following illumination ΔN_1 are illustrated. (b) Atom number vs loading time curves for no UV illumination (no LIAD) and illumination from various combinations of UV LEDs.

where the background atom number N_{bg} is a fictitious value arising from stray light in the absence of MOT fluorescence, $N_0 + N_{\mathrm{bg}}$ is the total apparent atom number, τ is an LED-specific time-constant and t is the time of loading [83]. We perform the measurement for an unilluminated MOT as well as various combinations of 365 nm and 380 nm diodes. The default (no LIAD) MOT loading rate had a characteristic time constant of 17 s. Both 365 nm + 365 nm and 365 nm + 380 nm arrangements were found to have a time constant of 4.2 s, as well as similar N_0. These arrangements are now used in the routine operation of the experiment and have reduced the required MOT loading time from 20 s to 8 s, a time saving of 60%.

3.1.3 Laser systems

Cooling and repump light for ^{87}Rb is produced by two Toptica DL Pro External cavity diode laser (ECDL) units [89] which are offset-locked in frequency from a 'master' Toptica DL Pro ECDL [57, 90]. Figure 3.5 illustrates the optical setups used for the cooling and repump lasers. The master laser is frequency-locked to a cooling transition

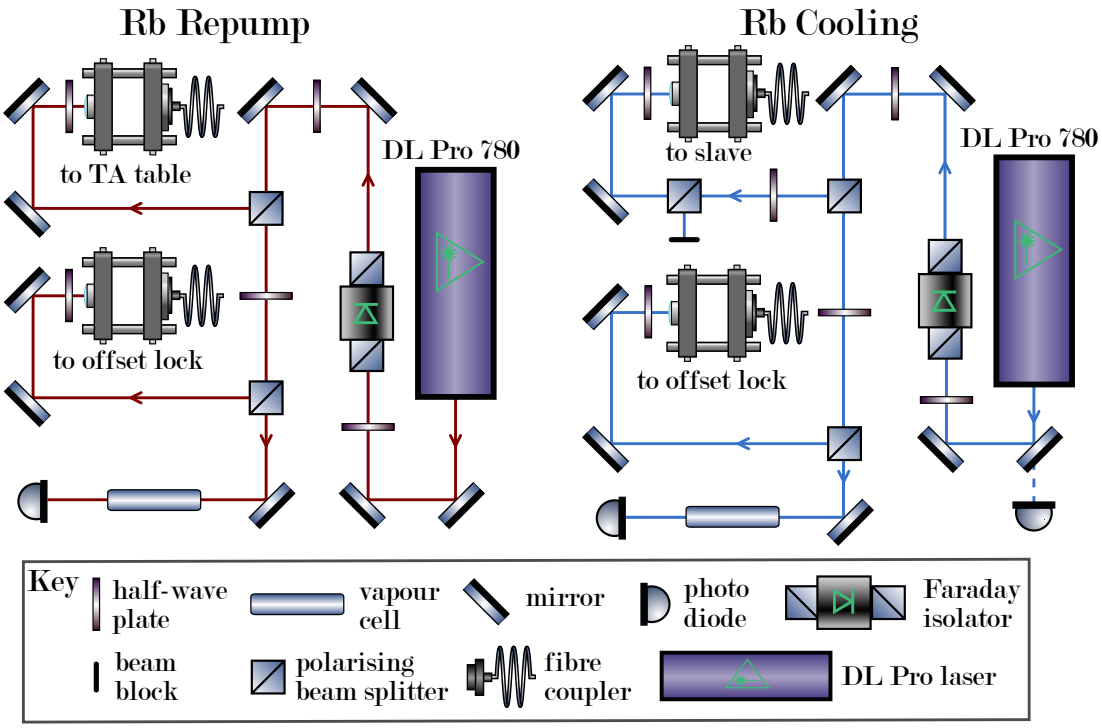

Figure 3.5: Schematic of the Toptica DL Pro lasers and optical apparatus used to producing cooling (blue) and repump (red) light for ^{87}Rb.

in ^{87}Rb using an error signal derived from modulation-transfer spectroscopy [61, 91] and off-the-shelf Proportional-integral-derivative (PID) feedback circuitry.

Adjustment of a reference frequency within the offset-locking electronics can tune the cooling or repump laser frequencies over several tens of MHz. This feature allows for quick switching between resonant frequencies used for imaging and off-resonant frequencies used in laser cooling, thus removing the need for separate optical modulators.

Each DL Pro laser produces up to 100 mW of light, which is insufficient to provide the 450 mW of total optical power required for sufficient atom numbers in the MOT. Furthermore, a proportion of the cooling light is used for imaging the atomic gases. We choose to amplify of the cooling light using an additional 'slave' laser. In our arrangement, illustrated in figure 3.6, 1-2 mW of frequency-locked cooling light is

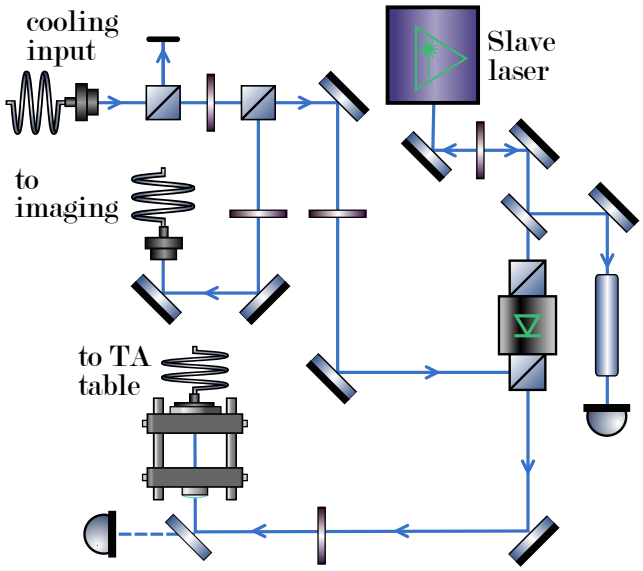

Figure 3.6: Schematic of the injection-locked slave laser setup for ^{87}Rb cooling light. Output power can be monitored using a photodiode.

injected into a diode laser[1], such that the output mode and frequency of the diode laser are locked by the seed. As compared to a DL Pro, diodes used in the slave laser are extremely cheap, and the laser can be operated close to the limit of its output power of ∼150 mW. The expensive DL Pro laser can be operated at lower output powers to preserve its long-term operation.

The repump light and slave-amplified cooling light are combined and further amplified by a tapered amplifier[2] [61] to give approximately 360 mW of cooling light and 90 mW of repump light, which is then directed into the MOT chamber via a polarisation-maintaining optical fibre. We typically achieve around 3.5×10^9 atoms of ^{87}Rb in the MOT in steady-state operation.

3.1.4 The colder Magneto-optical Trap

After laser cooling in the leftmost chamber of figure 3.1, atoms are transported to the UHV glass cell. This journey entails atoms being dragged through a 1 mm^2 hole

[1]Panasonic LNC780PS01WW diode
[2]Eagleyard EYP-TPA-0780-01000

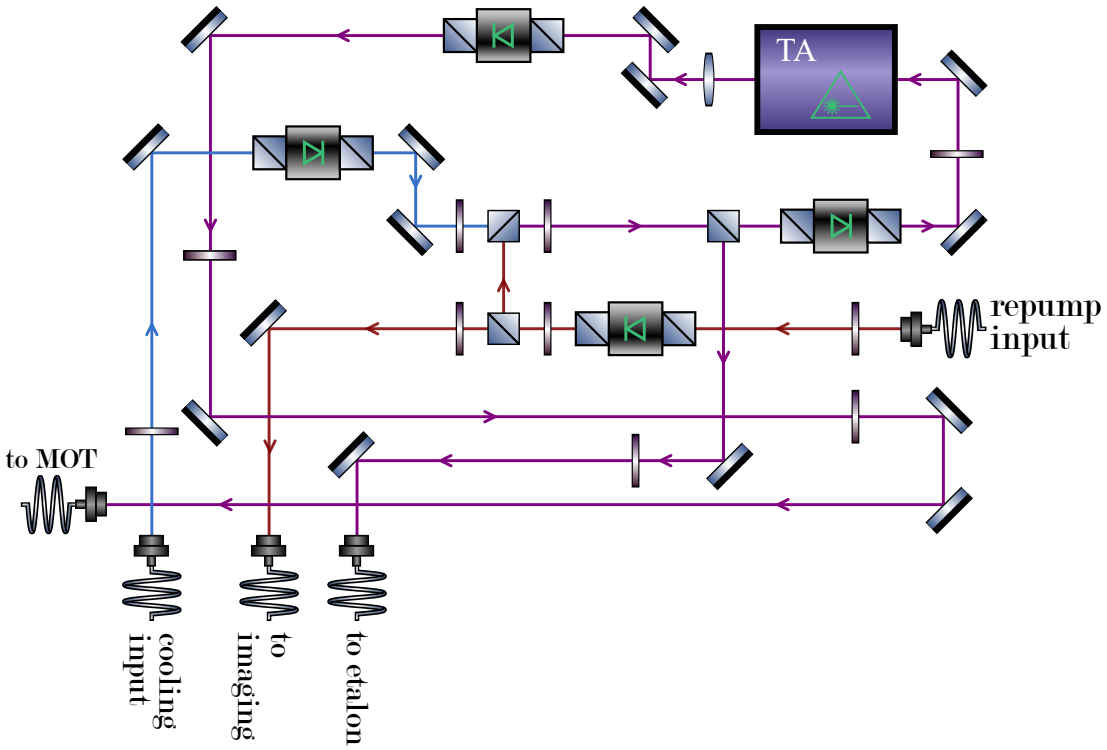

Figure 3.7: Schematic of the tapered amplifier and optical apparatus which produces amplified cooling and repump light. Amplified light is shown in purple and unamplified cooling and repump beams are indicated by blue and red lines, respectively. Other outputs are repump light used in imaging atoms in the UHV glass cell and light sent to a Fabry-Perot etalon for diagnostics. Unlabelled fibre ports are unused.

in the pyramidal mirrors and then along the ∼0.8 m-long tube which connects the opposite ends of the apparatus. The efficiency of this process, defined by the number of atoms which arrive in glass cell, is strongly dependent on the initial temperature of the gas. Thus, following the initial stage of laser cooling in the MOT, trapped atoms are subjected to further cooling in the cMOT.

The cMOT acts to reduce the temperature by approximately an order of magnitude [73, 92]. This is achieved by ramping down the magnetic quadrupole field gradient, which increases the volume over which sub-Doppler cooling mechanisms can occur [61, 92]. Simultaneously, the cooling light is detuned further, which reduces the effects of internal re-radiation which causes heating. The efficiency of the cMOT is dependent on several parameters, which include the time-dependent behaviour of the cooling and repump light frequency and the magnetic quadrupole gradient over the ∼300 ms duration.

The additional cooling provided by the cMOT, as compared to laser cooling in the MOT alone, significantly increases the efficiency of the experimental sequence, resulting in a greater number of atoms in the trapped vapour for all subsequent experimental stages. Furthermore, machine learning optimisation of the cMOT parameters has yielded a factor of 3 increase in the number of atoms transported to the glass cell, which is discussed in Chapter 4.

3.1.5 Controlling the experiment

The phrase 'quantum gas experiment' is often used to describe the collective operation of stages of laser cooling, evaporative cooling, potential shaping and imaging, which together realise and probe a quantum mechanical state-of-matter, such as a BEC. The successful and repeatable operation of these stages is dependent on the precise control of many experimental parameters. Often, these parameters must be varied on timescales of order µs and is therefore a task best suited to an 'experimental control'

computer. In our context, the experimental control computer is used to compile and deliver logical instructions to several National Instruments digital[3] and analog[4] output units. Analog outputs are connected to a variety of laboratory hardware, including: signal generators, voltage-controlled oscillators, cameras and power supplies. Digital outputs control the operation of switches, shutters and trigger image acquisition using several cameras. Furthermore, digital outputs are used to program RF-generating hardware, as detailed further in section 3.4.1.

Software required to write and compile sequence instructions was developed by Elliot Bentine [57]. Within the scope of this thesis, the control system has been extended to include machine learning optimisation routines and to control Microwave (MW) synthesisers for experiments detailed in Chapters 4 and 5, respectively.

3.2 Evaporative cooling

Atoms in a gas at a finite temperature have a distribution of energies described by the Boltzmann distribution [93]. Evaporative cooling is performed by selectively ejecting the highest-energy atoms, thus reducing the average energy of the remaining atoms. Atoms rethermalise through collisions such that the distribution of energies re-equilibrates and is characterised by a lower temperature [94]. In our case, evaporation is performed by the application of a weak RF field, colloquially referred to as a 'knife'. This removes atoms with energy exceeding a threshold determined by the frequency of the knife, by exploiting the energy level structure within the trap, as we now discuss.

The application of a magnetic field acts to Zeeman-split the otherwise degenerate states of the manifold. Furthermore, in a spatially-dependent magnetic field, the Zeeman splitting is dependent on the spatial location within the trap. This can be exploited to selectively eject atoms which explore a greater volume of space owing

[3]National Instruments 9403 & 6534
[4]National Instruments 9263

to their higher-than-average kinetic energy. During the evaporative cooling stage the RF knife frequency is reduced steadily; as the evaporation stage progresses, this reduces the threshold energy at which atoms are removed and further lowers the cloud temperature.

The RF knife is first applied when performing evaporative cooling on atoms trapped in the magnetic quadrupole trap and again in the TOP and TAAP traps, which are presented in the following section. The RF field is sourced from a synthesizer, amplified and transmitted to the atoms using a coil antenna situated above the UHV glass cell. Evaporative cooling stages have also been optimised using machine learning methods, which are detailed at length in Chapter 4.

3.3 Magnetic traps for cold atoms

After laser cooling in both the MOT and cMOT, the atoms are transported to a UHV glass cell using magnetic field-producing coils mounted on a translation stage. The UHV glass cell is maintained at approximately 1×10^{-10} torr by two ion pumps, which are arranged in a differential pumping configuration [61]. The atom cloud is then confined in the glass cell by a quadrupole magnetic field produced by fixed current-carrying coils. Additional coils are used to produce auxiliary fields throughout the transport stage to minimise heating and improve mode-matching to the final confining potential.

The atoms confined in the magnetic quadrupole trap are cooled to around 50 µK by forced evaporation using an RF knife [94]. We then apply a rotating 7 kHz field, forming a TOP trap [5]. Depending on the context of the specific experimental sequence, strong RF fields can then be applied, using macroscopic current-carrying coils which surround the UHV glass cell, to form a TAAP trap and, later, an RF-dressed potential trap.

3.3.1 The magnetic quadrupole trap

We first revisit the theory of magnetic trapping, which is presented in Chapter 2. The potential energy $U(\mathbf{r})$ of an atom in a magnetic field is given by

$$U(\mathbf{r}) = -\boldsymbol{\mu} \cdot \mathbf{B}(\mathbf{r}) = m_F g_F \mu_B |B(\mathbf{r})|. \tag{3.2}$$

In the case of a magnetic quadrupole field, $\mathbf{B} = B'(x\hat{\mathbf{e}}_x + y\hat{\mathbf{e}}_y - 2z\hat{\mathbf{e}}_z)$, with field gradient B', the magnitude of the field grows linearly as a function of displacement from the central field node and forms a 'linear' trap for states with $g_F m_F > 0$.

There are two magnetic quadrupole traps utilised in our experimental sequence. The first is produced by current-carrying coils in an anti-Helmholtz arrangement which are mounted on a moving translation stage. This is used to provide the relatively weak magnetic field required in the MOT and the stronger field necessary to transport atoms from the MOT chamber to the UHV glass cell. The second magnetic quadrupole trap is formed by a fixed pair of current-carrying coils, also in an anti-Helmholtz arrangement, mounted concentrically along the vertical axis and either side of the UHV glass cell. These coils are water-cooled and separated spatially by approximately 10 cm. The fixed quadrupole coils are indicated by the thick blue coils in figure 3.8.

After transporting the laser-cooled atomic cloud to the UHV glass cell, we perform evaporative cooling over 15 s to produce an atomic cloud of 1×10^7 atoms at approximately 50 µK. The magnetic quadrupole trap is a useful trap architecture in which to perform a first stage of evaporative cooling: the trap depth is very large, and thus atoms with very high kinetic energies remain trapped. The confinement provided by the trap is tight and consequently thermal re-equilibration occurs quickly, as this occurs on a timescale inversely proportional to the confinement strength. However, when approaching µK temperatures, the central node in the magnetic quadrupole

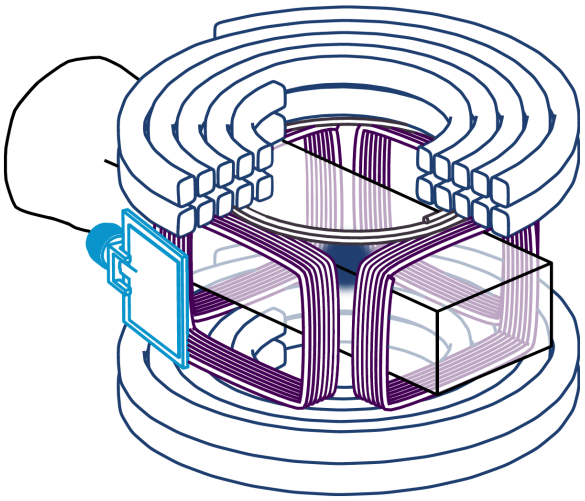

Figure 3.8: Schematic of the UHV cell-side magnetic trapping apparatus, showing the quadrupole coils (dark blue), the x and y dressing RF coil pairs (purple), the RF coil used for evaporation (grey) and the microwave patch antenna (light blue). The TOP coils, not shown for clarity, are similar in position and scale to the dressing RF coils. The atoms (dark blue cloud) are confined within the UHV glass cell (black) and a section of the upper quadrupole coil is cut away for clarity. This figure is based on an earlier version by Elliot Bentine.

field permits unwanted Majorana transitions, or spin flips, to untrapped states and causes atom loss [94]. Therefore the magnetic quadrupole trap is not suitable for further cooling towards degeneracy.

3.3.2 The Time-Averaged Orbiting Potential trap

From the magnetic quadrupole described in the previous section, atoms are loaded into a TOP trap to continue evaporative cooling [5,94]. The magnetic field of the TOP trap is a combination of a static quadrupole field and a rotating 7 kHz bias field that lies in the horizontal plane. The bias field is described by $\mathbf{B}_{\text{bias}}(t) = B_x \cos(\omega t)\hat{\mathbf{e}}_x + B_y \sin(\omega t)\hat{\mathbf{e}}_y$, where $\omega = 2\pi \times 7\,\text{kHz}$ is the field rotation frequency, and B_x and B_y are the amplitudes of the quadratures of the bias field. B_x and B_y can be individually controlled to produce an elliptically-polarised field, with anisotropy ϵ expressed as $\epsilon = B_y/B_x - 1$. The time-averaged combined field magnitude is consequently of the

form

$$\langle B \rangle_t \sim B_x \sqrt{1+(1+\epsilon)^2} + \frac{B'^2}{4B_x} \left(x^2 + \frac{y^2}{1+\epsilon} + 8z^2 \right) . \quad (3.3)$$

The magnitude of the magnetic field in this trap is no longer zero at the potential minimum, which prevents the occurrence of Majorana loss, and evaporative cooling in the TOP trap can cool the gas to degeneracy. Alternatively, a truncated evaporative cooling sequence can cool the cloud to temperatures of order 600 nK prior to loading the gas into RF-dressed trap architectures.

3.3.3 Implementing RF-dressed potentials

Following the TOP trap, we load atoms into trapping potentials formed by the application of both static and oscillatory magnetic fields. The experimental sequence proceeds as follows. RF radiation is applied to atoms confined in the TOP trap, to realise a TAAP trap [95]. A final stage of evaporative cooling proceeds in the TAAP trap where the RF knife frequency is controlled to realise cold thermal gases at $\sim$0.4 µK or to produce BECs of $0.5 - 4 \times 10^5$ atoms at $30 - 150$ nK. Following the completion of the evaporative cooling stage, the amplitude of the bias field is ramped to zero and the atoms are loaded into an RF-dressed potential. RF-dressed potentials are discussed in detail in Chapter 2, where we discuss the geometry and versatility of this trapping method. Additional RF fields can be applied to realise a double-well potential [34] or to perform RF spectroscopy of the trapped gases [58].

So far, we have described the apparatus and methods which are necessary to realise ultracold gases which are then used in several experiments, including: species-selective manipulations of mixtures in double-well potentials (Chapter 5) [36], probing the out-of-equilibrium dynamics of 2D Bose gases (Chapter 6), and to realise matter-wave interference of BECs (Chapter 7) [44]. We now discuss the technical details and implementation of RF field-producing hardware which is vital to the operation of this

apparatus.

3.4 Producing and controlling RF fields

RF fields are not only used in the realisation of tunable trapping potentials: forced evaporative cooling using an RF knife produces an ultracold cloud, and RF and MW fields drive transitions between eigenstates in spectroscopic studies of the potentials or to form mixtures of atoms in different hyperfine states, respectively. For the case of RF-dressed potentials, the number of available RF components limits the range of trapping geometries which may be realised. The experimental scheme to load atoms into a double-well potential, as detailed in Chapter 5, uses and controls a minimum of 4 separate RF fields: the circularly polarised RF field which forms the TAAP comprises RF fields along $\hat{\mathbf{e}}_x$ and $\hat{\mathbf{e}}_y$, and the final double well is formed of 3 linearly polarised fields along $\hat{\mathbf{e}}_x$. Previously, the RF fields were generated using a Direct Digital Synthesis (DDS) with a maximum of 4 output channels and which suffered from various issues including noise [57, 61]. In the course of this thesis, we have replaced these units with state-of-the-art RF-generating hardware, which can produce up to 16 distinct RF fields. Furthermore, this system provides higher output amplitudes and better shielding against spurious noise.

This section details the operation of the RF-generating circuit boards which are now used and describes the hardware required to interface these devices with the experimental apparatus.

3.4.1 Urukul DDS modules

The DDS PCB modules[5] are designed by M-Labs and other collaborators as part of the Artiq project[6]. Specifically, the Urukul system comprises DDS chips, buffers,

[5] https://github.com/sinara-hw/Urukul/wiki
[6] https://m-labs.hk/artiq/sinara.html

Field-Programmable Gate Array (FPGA) units and other components as a rack-mountable PCB. Each Urukul system houses 4 DDS chips[7] and their respective SMA output connectors. The clock signal can be derived from an external source, via an SMA input, or from a local quartz oscillator clock[8]. Logical communications are processed by an FPGA module[9] and Urukul cards can be daisy-chained or addressed separately. Power is provided by 12 V and 3.3 V power rails via the 30-pin input block.

3.4.1.1 Communication with the DDS chips

Communication with our experimental control system is performed by a National Instruments digital output card[10], which delivers a programmed waveform containing logical information to connected devices. The output cards produce 0-5 V Transistor-transistor logic (TTL) signals which are delivered by 68-pin high-density SCSI connectors. We interface this connector to the Urukul modules by isolating each channel and converting the signal level to 3.3 V (Low Voltage Transistor-transistor logic (LVTTL)). Groups of 8 communication lines are combined with two ground and two 15 V power lines inserted together into a 12-pin IDC header block. The PCB to perform these tasks is shown in figure 3.9 (a). Each of these blocks is then connected to a subsequent PCB where the communication channels are each converted to low-voltage differential signalling (LVDS) pairs (3.3 V $\pm$ 0.35 V (typ.)), as required by the Urukul modules. The 15 V input is converted to regulated power lines at 12 V and 3.3 V. The power and communications lines are then combined into a 30-pin IDC header block, which is compatible with the connections on the Urukul module. A PCB to perform these tasks is shown in figure 3.9 (b). Individual DDS chips are selected using CS0, CS1 and CS2 lines with the appropriate address, which can be

[7] Analog Devices AD9910
[8] Crystek CCHD-950-50
[9] Xilinx X2CC128
[10] National Instruments 6535

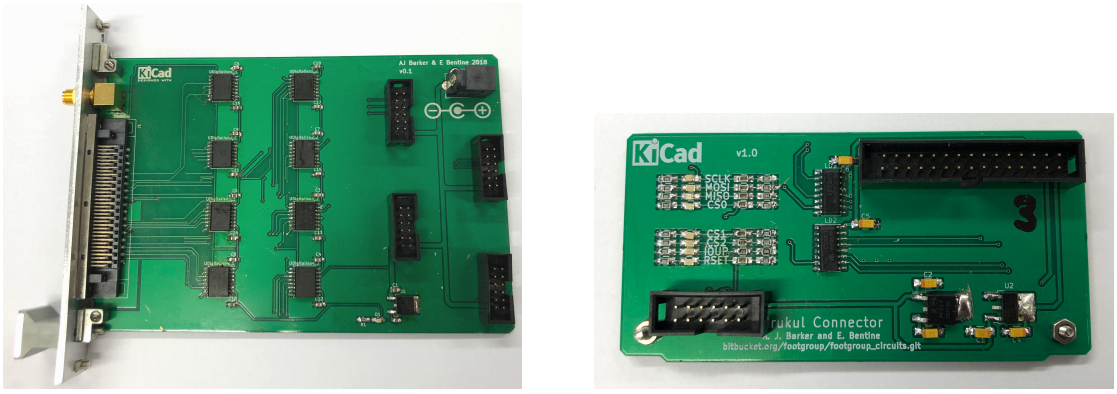

(a) (b)

Figure 3.9: PCBs required to interface between National Instruments digital output and Urukul DDS boards. (a) Digital isolation board for National Instruments SCSI connector to 12-pin IDC headers. (b) Conversion PCB to provide conversion from isolated LVTTL signals to LVDS pairs. Regulated power lines at 12 V and 3.3 V are combined to form a 30-pin EEM connection compatible with the Urukul board.

found in the versioned documentation.

3.4.1.2 Programming the DDS chips

The output of the DDS chips is determined by several programmable registers, and operates within the ranges summarised by table 3.2. Additional programmable registers control the attenuators, switches and LEDs of the Urukul units. To assist users, we have written an interface which includes functions to perform a simultaneous update of amplitude, frequency and phase of the RF output across several chips, as well as functions to initialise and reset each chip. The high-level functions assemble logical instructions, which are communicated to the DDS chips using the aforementioned hardware via Serial Peripheral Interface (SPI). Source code and documentation can be found in *https://bitbucket.org/footgroup/174-urukul*.

Output Frequency	Frequency Resolution	Phase Resolution	Amplitude Resolution
1-400 MHz	0.25 Hz, 32 bit	16 bit / 2π	14 bit / 2 V

Table 3.2: RF output characteristics of Analog Devices AD9910 DDS chips.

A summary of regularly used on-chip registers is as follows.

- Control Function Register 1 (4 bytes, address 0x00): features include power cycling and shift keying;
- Control Function Register 2 (4 bytes, 0x01): features include internal phase-locked loop (PLL) settings and bits to enable amplitude control and latency matching;
- Control Function Register 3 (4 bytes, 0x02): features include internal phase-frequency detector settings;
- I/O Update Rate (4 bytes, 0x04): required to set the output update rate.

We utilise the Single-Tone profile 0, address 0x0E, to set the RF output of each DDS chip. The 8 bytes of the Single-Tone profiles are distributed as shown below.

- 63:62 Open
- 61:48 Amplitude scale factor word
- 47:32 Phase offset word
- 31:0 Frequency tuning word

In later stages of the experimental sequence, amplitudes of RF fields are varied to load atoms into several RF-dressed potentials. A 14-bit register for the output amplitude of each channel permits smooth amplitude ramps which minimise unwanted excitation of the trapped gas.

The implementation of Urukul hardware has significantly extended the RF-generation capabilities of the experiment apparatus. The ability to produce many dressing RF components, as well as increased output amplitude and noise suppression, increases the range of trapping potentials which can be realised. RF outputs have since been used to drive AOMs used in a Bragg diffraction apparatus.

3.5 Other hardware

The power of the RF radiation generated by the Urukul modules is too low to produce RF-dressed potentials. We thus amplify the RF output of the Urukul modules using

22 W amplifiers[11]. The amplifiers are connected to RF antennae which surround the UHV glass cell via an impedance matching apparatus, to maximise the power delivered to the atoms. Many variants of impedance matching circuits have been tested and a coiled coaxial cable design had been used for many years. Experiments detailed within this thesis were performed using a narrow-band match comprising RC filters which is resonant at approximately 2 MHz. Further detail on the nature of the impedance matching apparatus will be provided in the thesis of David Garrick.

Experiments detailed in Chapter 5 concern a mixture of atoms in different hyperfine states. To produce this mixture, we apply a pulse of MW radiation using a patch antenna which is resonant with the hyperfine splitting of ^{87}Rb at approximately 6.8 GHz. The MW radiation is sourced from a commercial synthesizer[12] in series with a 20 W amplifier[13]. A pulse at 6.83468 GHz transfers a fraction of atoms from the $F = 1$, $\tilde{m}_F = 1$ state to the $F = 2$, $\tilde{m}_F = 1$ state. The fraction of atoms transferred, and hence the relative densities of the two states, can be controlled via the MW pulse duration.

3.6 Imaging an atomic cloud

After performing experiments on gases in the TOP or RF-dressed traps, the atoms are imaged and the images analysed to extract properties of the gas such as total atom number, temperature, and phase-space density (PSD). Images can be taken after time-of-flight (TOF) expansion, where the gas has expanded in free fall, or *in situ*, where the atoms remain trapped during imaging.

Absorption imaging is a widely used method of extracting the spatial distribution of cold atoms, and is performed by illuminating the cloud with resonant light. In our case, in combination with a bias field along the direction of imaging, we use light

[11]Mini-Circuits LZY-22+
[12]DS Instruments SG12000PRO
[13]Microwave Amps, AM53-6.4-7-43-43

which is resonant with the $F = 2,\ m_F = 2$ to $F' = 3,\ m_{F'} = 3$ cycling transition. Prior to imaging, atoms are optically pumped to $F = 2,\ m_F = 2$, such that they are in resonance with the imaging light.

Absorption imaging relies on the Beer-Lambert law, which describes the absorption of light as it propagates through a medium [52]. The output intensity $I(x, y)$ as a function of optical density $D(x, y)$, is given by

$$I(x, y) = I_0(x, y)\ \exp(-D(x, y))\ , \tag{3.4}$$

where x, y are spatial coordinates and $I_0(x, y)$ is the incident intensity [52]. The optical density is dependent on the spatial distribution of scatterers $n(x, y, z)$ and their cross-section to absorption $\sigma(I, \delta)$, as follows:

$$D(x, y) = \int \sigma(I, \delta) n(x, y, z) dz\ , \tag{3.5}$$

where z is the axis of propagation of the light. The cross section $\sigma(I, \delta)$ is dependent on the intensity of the incident beam, as well as the detuning from resonance δ, such that

$$\sigma(I, \delta) = \frac{\Gamma}{2}\ \frac{2I(x, y)/I_{sat}}{1 + 2I(x, y)/I_{sat} + 4\delta^2/\Gamma^2}\ \frac{\hbar\omega}{I(x, y)}\ , \tag{3.6}$$

where ω is the angular frequency of the incident light [61]. I_{sat} is the saturation intensity and Γ is the natural linewidth of the atomic transition which, for the ^{87}Rb cycling transition described above, are $1.7\,\mathrm{mW\,cm^{-2}}$ and $\Gamma = 2\pi \times 5.7\,\mathrm{MHz}$, respectively. We use a 1 mW imaging beam collimated to a waist of 3.6 mm, which gives a corresponding intensity of $4.8\,\mathrm{mW\,cm^{-2}}$.

In a typical absorption imaging protocol, the distribution of atoms is extracted by taking three images. First, an absorption image of the atom cloud C_A is taken; secondly, an image C_L is taken with no atoms present; finally, an image C_B is taken

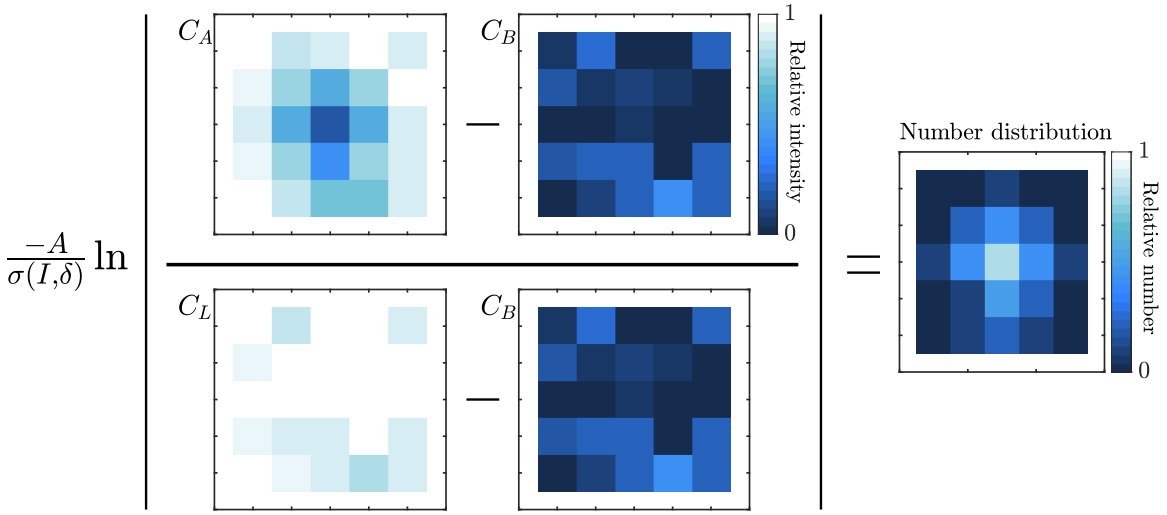

Figure 3.10: Schematic of the absorption imaging analysis described by equation 3.7.

with neither atoms nor light and is used to remove background stray light from the images. All images are taken with a camera sensor, which consequently discretises the continuous distribution of atoms into a distribution over pixels with coordinates (x', y'). The three images are analysed to produce a distribution of atoms $N(x', y')$ as follows

$$N(x', y') = \int_z \int_A n(x, y, z)\, dA\, dz = \frac{-A}{\sigma(I, \delta)} \ln\left(\frac{C_A - C_B}{C_L - C_B}\right) . \tag{3.7}$$

where A indicates the area of a sensor pixel. Equation 3.7 is illustrated in figure 3.10. Furthermore, absorption images are prone to suffer from aberrations and fringes. We utilise the methods of [96, 97], where a reference image $C_{B'}$ is constructed from the principal components of the set of $\{C_B\}$ across many experimental cycles, which acts to further suppress fringes and aberrations in the calculated atomic distributions.

3.6.1 Time-of-Flight expansion

TOF expansion describes a method whereby the atomic cloud undergoes a period of free fall, during which it expands ballistically, before an absorption image is taken.

This method is used to infer the momentum distribution of the cloud, as atoms with higher momentum travel further from the centre of mass. Furthermore, the expansion dynamics of a gas in the quantum regime are distinct from those of a thermal gas [94]. A quantum gas expands anisotropically: even in the absence of inter-particle interactions, a BEC which is confined tightly along one axis expands more rapidly along this axis than the less tightly confined axes. In contrast, the momentum distribution of a classical gas is isotropic. These distinct behaviours produce a bimodal spatial distribution of atoms after TOF expansion: the BEC component is responsible for a dense 'core' of atoms which lies within a broader 'pedestal' of thermal atoms, and is evidence that a condensed fraction has been formed.

3.6.2 Horizontal imaging

To image the spatial distribution of atoms, either *in situ* or after TOF expansion, a 'horizontal' imaging system images perpendicular to the direction of gravity, such that the focal plane is along the trajectory of TOF. A simple construction for an imaging system is a two-lens telescope: a lens of focal length f_1 (the objective lens) is placed a distance f_1 from the object. A second lens of focal length f_2 (the eyepiece lens) is placed a distance $f_1 + f_2$ from the first lens. Finally, a camera is placed a distance f_2 from the second lens; this realises a magnification of $|f_2/f_1|$.

When imaging trapped clouds, or the fringes produced in a matter-wave interferometry experiment, it is desirable to have as high a magnification and resolution as can be achieved. We use an objective lens of focal length 75 mm and a numerical aperture (NA) of 0.18. This places a diffraction limit on our imaging system of $1.22\lambda/\mathrm{NA} = 5.3$ µm, for 780 nm light. We choose an eyepiece lens of focal length 200 mm, which gives a theoretical magnification of 2.67. The true magnification of the imaging system was measured using a free-fall measurement and by fitting the trajectory of a falling atom cloud to give a magnification of 2.81(0.06). In our experi-

mental apparatus, the proximity of the objective lens to the glass cell in the horizontal plane is constrained by immovable current-carrying coils, which bounds the working distance of the objective lens to around 70 mm. The optical apparatus is illustrated in figure 3.11 (a).

We align the imaging system using the method described in reference [98]. We vary the proximity of the objective lens to the UHV glass cell using a translation stage and perform *in situ* absorption imaging on BECs in the shell trap. The optical aberrations associated with misalignment of the imaging system behave as random scatterers, creating diffraction patterns which change predictably as a function of distance from the optimal focus. The power spectral density of Fourier components with wavevector k in the Fourier transform of the absorption images increases as the system is focussed. Figure 3.12 (upper) shows slices of absorption images of the BEC as the system is focussed. For the corresponding images above, the power spectrum of the Fourier components with wavevector k is shown in figure 3.12 (lower), where darker colours indicate higher power spectral density, and displays a peak which is used to identify the focus of the imaging system.

For diagnostic purposes and for imaging larger or hotter clouds, it is desirable to have a secondary imaging system with a lower magnification and larger field-of-view. To achieve this, the telescope includes a servo-driven flip mirror, which can switch between the high-magnification axis and a secondary system with magnification 1.

Both horizontal imaging axes use CCD cameras[14], with pixel size 4.54 µm × 4.54 µm and sensor area of 1936 × 1456 pixels. Cameras are fixed to a home-built aluminium frame with the base of the camera supported by an exchangeable spacer, which allows for repeatable vertical positioning to suit the desired central point of the imaging system. The mount and camera are shown in figure 3.11 (b).

[14]Ximea MD028MU-SY

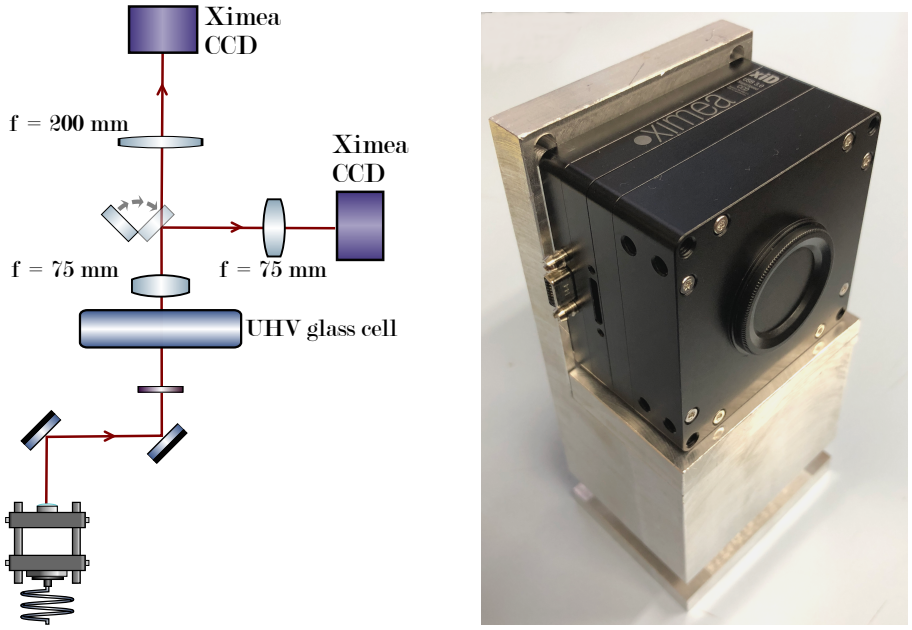

(a) (b)

Figure 3.11: Apparatus used in the horizontal imaging axis. (a) Optical apparatus to realise high magnification (2.81) and low magnification (1) imaging. (b) Ximea CCD camera secured in aluminium mount.

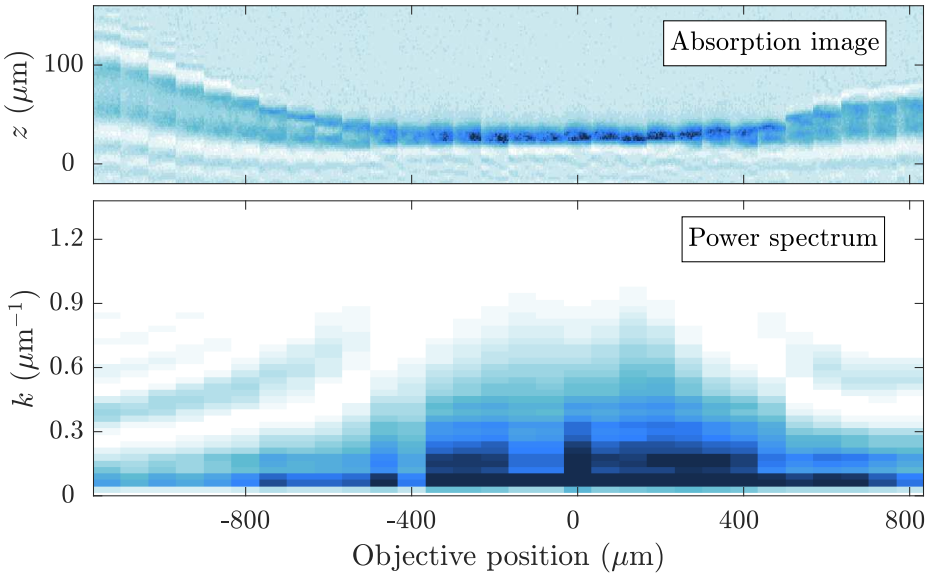

Figure 3.12: Focussing the horizontal imaging system. Upper: slices of absorption images of *in situ* BECs as the objective lens position is varied. Lower: power spectrum of the Fourier components of the corresponding slices, where darker colours indicate higher power spectral density. The x axis is chosen such that a value of 0 indicates the focus.

3.6.3 Vertical imaging

The experiment is equipped with an additional imaging system aligned along the vertical axis which possesses a magnification of 14 and a diffraction-limited resolution of 1.6 µm. Further detail on the objective lens and other components is provided in reference [61]. Recently, the camera has been replaced by a Peltier-cooled, high-gain CCD camera[15], which has greatly improved image quality. This camera features a sensor of 1024 × 1024 pixels and pixel size of 13 µm × 13 µm. This vertical imaging system is used in experiments detailed in Chapter 6.

[15] Andor iKon-M

4

Optimising a quantum gas experiment

This chapter describes the application of three machine learning strategies to optimise the atomic cooling processes utilised in the production of a BEC, and is largely based on reference [42]. For the first time, optimisations of both laser cooling and evaporative cooling mechanisms were performed simultaneously. We compare the performance of an evolutionary optimisation method (Differential Evolution), a regression method based on non-parametric inference (Gaussian Process regression) and a gradient-based function approximator (Artificial Neural Networks). Optimising the cooling processes produces a factor of four increase in the BEC atom number, as compared to intensive manual optimisation, and provides an automated approach that maintains close-to-optimal performance in long-term operation. Furthermore, we show that our optimisation techniques can be tailored towards other experimental aims, such as improving sequence repetition rate or maximising the number of atoms at a given temperature.

4.1 Introduction

Recent developments in Artificial Intelligence and specifically machine learning have provided tools with which a computer can significantly outperform the analytic capability of a human, particularly when data sets are large or when a system relies on many free parameters [99]. As compared to a human, a major advantage of many machine learning methods is that the chosen learner has no preconceptions for how the parameters should affect the final result, and is therefore objectively guided by the data alone. Dramatic advances arising from the application of machine learning methods have been achieved in many scientific fields and contexts, such as supply chain forecasting and healthcare [100, 101]. In this chapter, we present the application of several different machine learning algorithms in the optimisation of a quantum gas experiment.

The techniques used to reach ultracold temperatures usually include a combination of optical cooling and forced evaporative cooling [5, 6, 102]. As outlined in Chapter 3, implementing these cooling processes requires the precise control of magnetic fields, frequencies of lasers, timings and other components of the experiment. Together, the changes of these experimental parameters, referred to as 'settings'[1] form a 'sequence' of instructions which is coordinated by an experimental control system. The space that describes a typical experimental sequence is large and locating the best settings using exhaustive, brute-force searches is unfeasible.

Given the intrinsic complexity, when building a new quantum gas experiment, analytic models are often used to predict optimal values and trajectories for experimental settings. Well-established theory exists to explain several of the typical stages common to cold-atom apparatuses. For example, the cooling of atoms by the radiation forces exerted by laser light has been investigated for decades [56] and forced

[1] This avoids confusion with parameters of machine learning methods or models.

evaporative cooling in optical or magnetic traps is routinely used to realise degenerate gases [103]. The theories describing these stages of cooling contain approximations but are nevertheless accurate when the exact specifications of the experimental apparatus are known. However, in real-life experiments, equipment can suffer from unknown imperfections or external perturbations. Nevertheless, manual optimisation of the experimental settings is often performed by using the theoretical optimum predictions as a starting point, thus partially mitigating these imperfections.

Recently, machine learning techniques have been applied in the field of ultracold quantum matter to optimise individual laser cooling and evaporative cooling stages and to realise significant improvements in the performance of the specific experimental apparatuses [104–106]. The application of these methods in each case, however, was limited to only a subset of the atomic cooling processes and did not consider the transitions between each process, thus increasing the likelihood of an optimisation method finding a local rather than a global optimum.

We avoided this shortcoming by a simultaneous optimisation of both laser cooling and evaporative cooling stages. Additionally, we compare the efficacy and rate of convergence of three common algorithms when applied to our optimisation problem. Exactly what constitutes an optimised quantum gas experiment depends on the user's requirements, for example: quicker experiments with a higher repetition rate produce a greater amount of data in a given time; lower cloud temperatures can improve the precision of spectroscopic measurements, and a larger atom number or higher peak density can improve the signal-to-noise ratio when imaging the BEC. Here, our chosen metric for optimisation consists of maximising the atom number in a BEC, unless stated otherwise.

We define our methods of optimisation in section 4.3 and implement these using an open-source software package (M-LOOP) [106, 107]. The improvements in experimental performance that result from the optimisation of several cooling stages, both

individually and collectively, are then presented. We further utilise Gaussian Process regression to identify sensitive experimental settings; this also highlights likely sources of instability within the experiment. Finally, we modify our optimisation metric to first minimise the sequence time required to produce a BEC, which is of great use when performing tasks such as optical alignment and to collect more data when atom number is not a priority, and later to produce clouds at specific temperatures.

4.2 Implementation

We briefly revisit our experimental apparatus and the several stages of trapping and cooling of an atomic vapour which lead to the production of a BEC [34, 95]; these are detailed further in Chapter 3.

4.2.1 Experimental sequence

An outline of the experimental apparatus and optimisation scheme is illustrated in figure 4.1. In summary, atoms are first laser cooled in a MOT [74] from room temperature to around the Doppler limit (146 µK for ^{87}Rb) [80]. After loading the MOT, the trapped atoms are then subjected to further cooling in the cMOT [73] which acts to reduce the temperature by roughly an order of magnitude [92]. The efficiency of the cooling is dependent on many factors which include the frequency of the laser light and the strength of the applied magnetic field. The cloud is then transported by a moving magnetic field to a UHV glass cell where it is further cooled by forced evaporation.

Evaporation is first performed in a magnetic quadrupole trap and later in a TOP trap [5, 57]. The RF knife is applied to trapped atoms and the frequency is reduced steadily; as the evaporation stage progresses, this reduces the threshold energy at which atoms are removed and thus reduces the cloud temperature. Once a tempera-

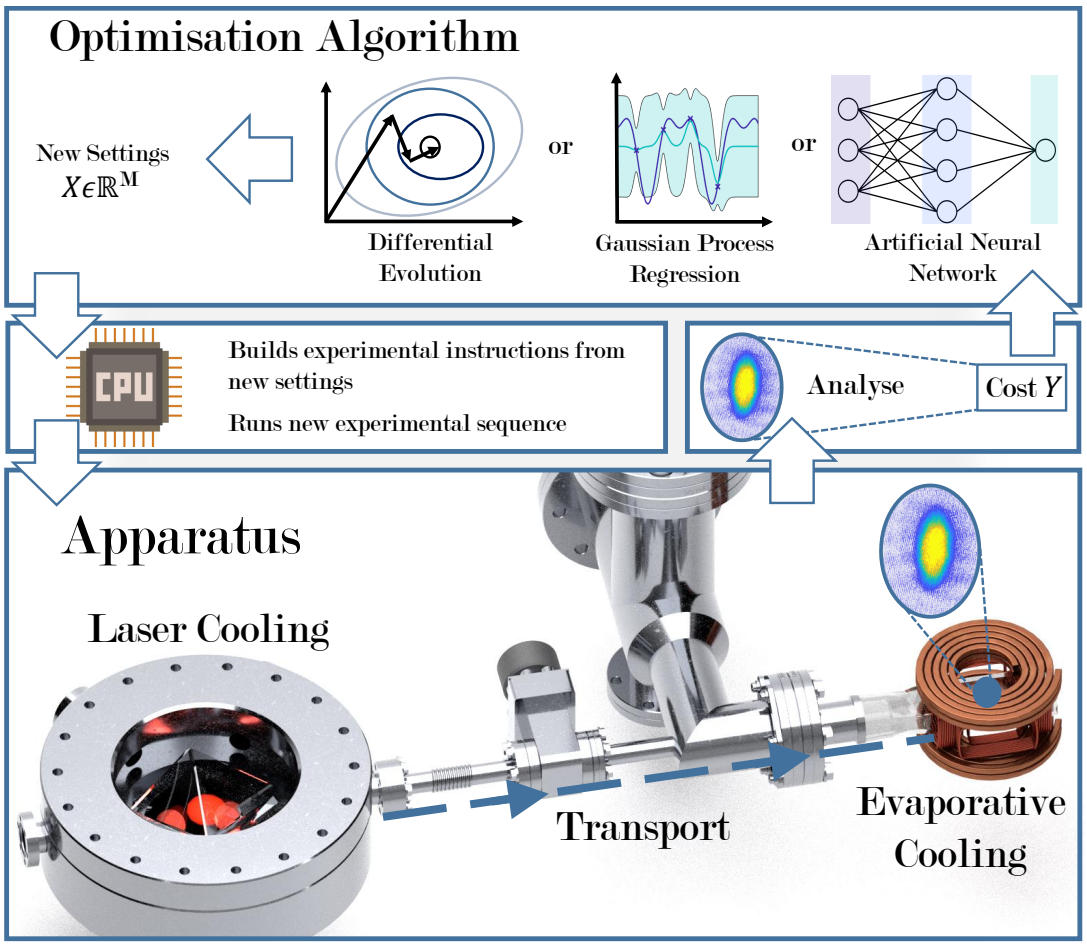

Figure 4.1: The experimental apparatus and the optimisation feedback loop. The atomic vapour is cooled initially using a combination of laser light and magnetic fields in the MOT before further cooling in the cMOT. The gas is transported to a UHV cell and evaporative cooling is subsequently performed. An image of the resulting gas is taken using absorption imaging [52] and is analysed to evaluate a cost function, which is based on the atom number in the cloud. The cost is passed to the chosen optimisation algorithm which produces a new set of experimental settings. These settings are processed by a control computer into a new set of instructions and used in the next sequence.

ture of approximately 50 µK is reached, atoms are loaded into the TOP trap. Here, the static quadrupole field is combined with a rotating bias field. The quadratures of the rotating bias field, B_x and B_y, can be individually controlled to produce an anisotropic field, with the anisotropy expressed by $B_y/B_x - 1$. Evaporative cooling proceeds in the TOP trap using the RF knife as before. This chapter concerns BECs produced in the TOP trap and thus further cooling in the TAAP trap, or loading into the RF-dressed traps, is not required.

Overall, the evaporative cooling processes in both traps are described by a number of settings which vary in time and include: the quadrupole coil current I_{Q}, the RF knife frequency and, in the case of the TOP trap, the amplitude and anisotropy of the TOP field. By adjusting these settings between successive sequences, we are able to optimise the experimental sequence to produce a quantum gas.

After all stages of cooling have been completed, the atomic cloud is released from the trap and undergoes a period of free fall during which it expands ballistically. The expansion dynamics of a gas in the quantum regime are distinct from those of a thermal gas [94], which produces a bimodal spatial distribution of atoms after TOF: the BEC component is responsible for a dense 'core' of atoms which lies within a broader 'pedestal' of thermal atoms (see figure 4.2 c)-d), for example). The TOF method allows us to observe the momentum distribution of the cloud which subsequently provides a means of optimising the production of a quantum gas, as is now detailed.

4.2.2 Cost function for optimisation

In the general scope of optimisation, the ambition is to identify the global optimum, which is often achieved using a systematic approach. In our experiment, the space in which we aim to find a global optimum is spanned by M experimental settings (currents, timings etc.). A point in parameter space is given by a vector of experimental

settings $X \in \mathbb{R}^M$, where each point in space has an associated cost $Y = f(X) \in \mathbb{R}$, generated by a cost function $f(X)$ [108]. Although the settings are continuous variables (up to floating point precision), bounds on each setting are imposed, owing to physical limitations or for safety reasons, hence the set is not strictly $\mathbb{R}^M$.

To optimise the number of atoms in the BEC component, rather than the overall number of atoms in the cloud, we define our cost function to be proportional to $-\log(\tilde{N})$, where $\tilde{N}$ is the number of atoms within a small region-of-interest (ROI) which is chosen to be comparable to the approximate extent of a typical BEC after TOF expansion [94]. For typical trap parameters in the TOP trap ($\omega_r \approx 2\pi \times 60$ Hz and $\omega_z \approx 2\pi \times 150$ Hz) and for BECs of ^{87}Rb with central density of $\sim 5 \cdot 10^{13}$ cm^{-3}, after a TOF of 25 ms, we expect a Thomas-Fermi width of approximately 60 µm (radial) and 90 µm (axial). Typical clouds encountered during the optimisation are illustrated in figure 4.2 (a)-(d). The cost function is less sensitive to the number of atoms in the thermal component which expands to a much larger area. We also choose to base the cost function on the logarithm of $\tilde{N}$, as the value of $\tilde{N}$ can span several orders of magnitude during the optimisation; bad settings may result in no atoms detected whereas BECs contain approximately 10^5 atoms.

Physically, our cost function can be interpreted as measuring the population of atoms with momentum close to zero, which increases as the optimisation progresses towards producing a BEC; the radius of the ROI determines a threshold momentum k_c, where atoms with momentum $k < k_c$ will contribute to $\tilde{N}$. This information may also be extracted using analytic functions which describe the bimodal distribution, however, these contain many free parameters (7, in the case of a bimodal fit along one dimension). This can make fitting temperamental, especially for the low atom numbers present in the early stages of optimisation, and parameters extracted from the fits can throw the learner off course.

We perform an experiment to highlight the value of the simple ROI method. We

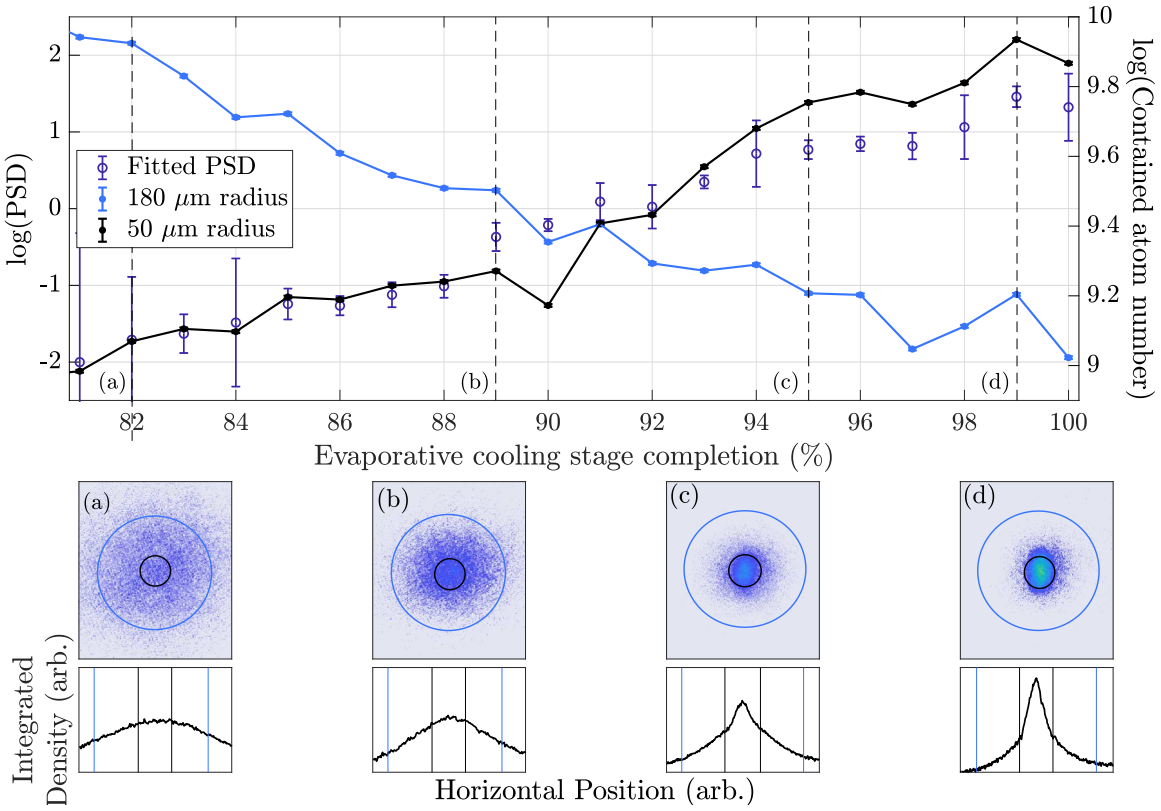

Figure 4.2: Fitted PSD (purple) vs evaporative cooling stage progression. Similarly, the number of atoms contained within regions of size 180 µm (blue) and 50 µm (black) as a function of evaporative cooling stage progression for the same data. Images (a-d, upper) show atomic density distributions after TOF for 82%, 89%, 95% and 99% stage completion, respectively. The counting regions of radius 180 µm (blue) and 50 µm (black) are also illustrated. (a-d, lower) show the density distribution integrated in the vertical axis plotted against horizontal position. The horizontal extent of the 180 µm (blue) and 50 µm counting regions are illustrated by blue and black lines, respectively.

vary the completion percentage of the evaporative cooling stage in the TOP trap and extract the PSD for each percentage using a bimodal fit. As shown in figure 4.2, the PSD extracted from the fit (purple) rises to and above the critical value for Bose-Einstein condensation. In addition, we illustrate the number of atoms contained within a ROI much larger than the extent of the BEC (180 µm radius, blue) and a ROI of comparable size (50 µm radius, black). We divide the number of atoms contained within the larger ROI by 8 for easier comparison with the smaller ROI on the same axis. The number of atoms contained within the smaller ROI increases with PSD, which supports our hypothesis that, after ejecting atoms of higher-than-average energy, the remaining atoms rethermalise to form a colder atomic cloud with a momentum distribution that is more strongly peaked around $k = 0$. Additionally, and as expected, the number of atoms contained within the larger ROI decreases as the evaporative cooling stage progresses and as the total atom number is reduced. Noting the equivalence of the curves, extracting PSD from a fitting procedure would provide similar information to a learner as our atom counting method. However, when the atomic cloud is faint or not visible, as is the case for earlier stages of the evaporative cooling stage, the fit fails. In contrast, the ROI method relies on no fitting parameters and is robust to small or faint clouds, which are encountered regularly during an optimisation routine.

4.2.3 Non-convexity and early stopping

The optimisation feedback loop, outlined in figure 4.1, can be summarised as follows: the machine learner is configured with an initial M-dimensional vector $\mathbf{X}_0$ of experimental settings. We also configure the allowed ranges that each setting can take, to ensure that generated sequences will not damage the apparatus. $\mathbf{X}_0$ is read by an experimental control computer, which defines relevant analog and digital outputs at time steps accordingly. The sequence is run and the resulting image is analysed to

produce a cost Y_0. This pair of settings and cost is then used by the chosen optimisation algorithm to determine the next vector $\mathbf{X}_*$ to be tested. Each new settings/cost pair updates our knowledge of how the cost varies with each setting. Consequently, any model of the variation of the cost with respect to each setting is subject to change with each new settings/cost pair [109].

The cost function described earlier will in general be non-convex and thus it is possible that any optimisation method may not converge to the global optimum. The user must therefore define conditions to terminate the optimisation. We specify 'early stopping' criteria such that the optimisation is terminated after a fixed number of sequences, or when no further improvement to the cost has been achieved in approximately 30 minutes. The likelihood of converging upon the global optimum can be increased by performing many optimisation procedures with varying initial conditions.

4.3 Optimisation methods

We compare the efficacy of three types of optimisation algorithm in the context of our experiment: an evolutionary optimisation method (Differential Evolution) [110], a regression method based on non-parametric inference (Gaussian Process regression) [111] and a gradient-based (parametric) function approximator (an Artificial Neural Network) [99]. To implement the optimisation routines, we utilise an open-source machine learning toolkit: Machine Learning Online Optimisation Package (M-LOOP), which is based on the Python scikit-learn library [106, 107].

We note that the optimisation methods are robust to random variations in cost for a given setting. This is appropriate for an experimental apparatus in which random fluctuations are present, either due to variation in the performance of laboratory equipment or because the results depend intrinsically on random processes (e.g. shot

noise fluctuations in the BEC atom number). This does not fundamentally prevent the algorithms from finding a good solution, but uncertainty in the cost increases the number of experimental sequences required for the solution to converge.

Algorithms can be categorised as 'smart' or 'simple'. Simple algorithms can often quickly find a solution close to the global optimum, as they do not rely on the construction of a complex, underlying model. However, they often take significantly longer to find the true optimum solution, as their methods of searching parameter space are crude, or get stuck in local minima in complex landscapes. We choose to investigate Differential Evolution (DE) as an example of a simple method.

Smart algorithms often construct a model of the cost landscape, which is iteratively edited based on additional data points. Nevertheless, the model is refined as more data is taken, and so smart algorithms can perform a more intuitive search that may arrive at the true optimum sooner. These algorithms are computationally intensive: the computation time for a Gaussian Process (GP), for example, scales as the cube of the number of data points. Furthermore, the model produced by a smart algorithm can be used to probe the sensitivity of the optimum solution to each parameter. In turn, this can help illuminate our physical understanding of the system. As a further motivation for a smart algorithm, our experimental cycle time of around 1 minute constrains the amount of data with which we can reasonably train our model.

In choosing a smart algorithm, we consider some of the more widely utilised methods, as well as their merits and failings. Artificial Neural Network (NN) methods are an obvious candidate as they have been a popular and successful method of approximating complex functions since their development in the 1960s. However, these networks often require vast amounts of data, which raises questions of compatibility with our experimental time constraints. A GP is a Bayesian inferential method which can be applied in a regression context to fit a model of cost vs experimental param-

eters. The modelled cost landscape can then be processed by a minimum-finding method in order to determine the optimal parameter set. However, smart learners often fail for small data sets, as there is insufficient data to train the method, which leads to large variance as the fit is generalised beyond the known data points. As such, we utilise simple methods (DE), to first explore the parameter space and to construct an initial training set which is later used by the smart learner.

4.3.1 Differential evolution

Evolutionary algorithms involve several key stages, which are inspired by biological evolution and natural selection [112]. First, an initial population is generated randomly. New individuals are then produced by mixing features of pre-existing individuals (crossover) and by adding random variation (mutation). Finally, selection is performed by replacing individuals in the population with low fitness by new individuals with high fitness.

In our experiment, the individuals are settings vectors $\mathbf{X}_i$ and the fitness is the associated cost Y_i of each vector. The initial population is a randomly generated set of n vectors $\{\mathbf{X}_1, ..., \mathbf{X}_n\}$ and their experimentally measured costs $\{Y_1, ..., Y_n\}$. Mutation produces a new vector $\mathbf{V} = \mathbf{X}_k + (\mathbf{X}_i - \mathbf{X}_j)$, where $\mathbf{X}_i$, $\mathbf{X}_j$ and $\mathbf{X}_k$ are randomly selected vectors [110]. Crossover is achieved by selecting elements randomly from either $\mathbf{X}_i$ or $\mathbf{V}$ to create a new candidate vector $\mathbf{X}_*$. A sequence is then performed using vector $\mathbf{X}_*$ and the value of the cost function Y_* is measured, producing an additional settings/cost pair $\{\mathbf{X}_*, Y_*\}$. Selection is performed by determining whether $Y_* < Y_i$; if so, $\mathbf{X}_*$ replaces $\mathbf{X}_i$ and the process repeats. Over time, the average cost (fitness) of the set of n vectors (individuals) decreases, as vectors with lower costs replace those with higher costs.

The DE method has low computational complexity and requires a small number of vectors from which to begin. However, the simplicity of the method results in

slow convergence towards a solution. Nevertheless, we utilise this method to build a set of settings/cost pairs which serves as a starting point to initially train the other optimisation methods.

4.3.2 Gaussian Process regression

Bayesian inference provides us with tools to update a posterior probabilility $P(H|E)$ of a hypothesis H given new observations E, as described by Bayes' theorem [111]:

$$P(H|E) = \frac{P(E|H)P(H)}{P(E)} \ , \tag{4.1}$$

where $P(E|H)$ is the likelihood of observing E given H and indicates the compatibility of the observations with the given hypothesis, $P(H)$ is the prior probability of H before making observations, and $P(E)$ is the marginal likelihood.

In general, a GP is a probability distribution over functions which describe a given dataset. GP regression utilises Bayes' theorem to update this probability distribution given new data [113]. A parametric method, for example linear regression, assumes the connection between $\mathbf{X}$ and Y is a linear curve and parameters, such as gradients and the intercept, are tuned to fit the data as well as possible. A major advantage of GPs is they are non-parametric and thus impose little bias to the function form of the relationship between $\mathbf{X}$ and Y prior to fitting to data.

Knowledge about a point in parameter space can be invoked in terms of a kernel function; a kernel is a measure of similarity between two inputs separated by a distance in parameter space. A popular choice is the squared-exponential, or Gaussian, kernel $K(\mathbf{X}_i, \mathbf{X}_j)$:

$$K(\mathbf{X}_i, \mathbf{X}_j) = \exp\left(-\frac{1}{2}\sum_{k=1}^{M} \eta_k \left(\mathbf{X}_i[k] - \mathbf{X}_j[k]\right)^2\right), \tag{4.2}$$

where $\mathbf{X}_i[k]$ represents the (dimensionless) k-th element in the vector $\mathbf{X}_i$, the

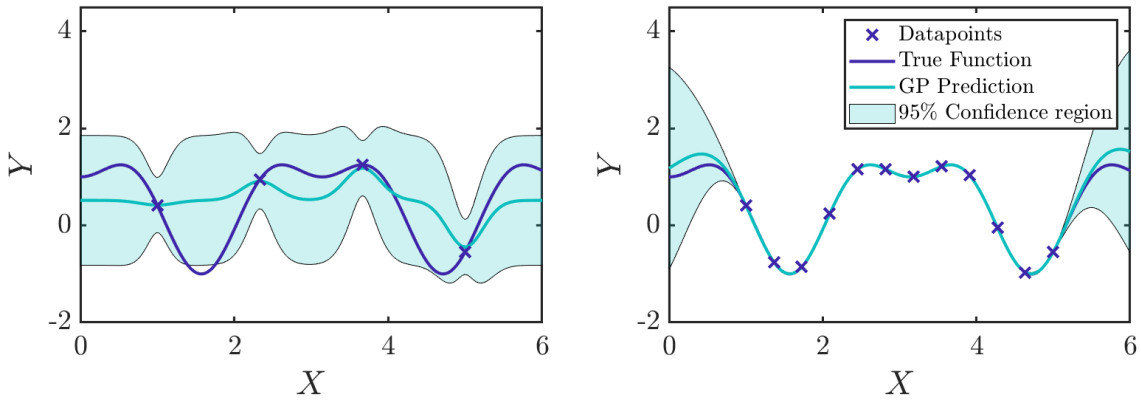

Figure 4.3: Illustration of a GP. Training data (crosses) are produced from an underlying analytic function (dark blue, solid). The learner produces a model, whose mean (green, solid) and 95% confidence interval (filled section) are illustrated. Left: training a model with 4 data points. Right: training with 12 data points.

dimensionless parameters $1/\eta_k$ are the characteristic sensitivities for each setting and the summation runs over all settings k. The η_k are generated when performing GP regression, and provide a measure of how strongly the kernel depends on changes to each of the settings.

In our context, the function that we fit using GP regression is the mapping between the experimental settings and the experimentally measured cost. Given an existing set of settings/cost pairs $\{\mathbf{X}_i, Y_i\}$, we can estimate the cost (and uncertainty) of any settings $\mathbf{X}_*$ according to the GP fit. We can therefore search for new experimental settings with the lowest predicted cost and iterate within our optimisation loop. To facilitate a comparison of η_k across all settings, we normalise each $\mathbf{X}[k]$ with respect to the minimum and maximum allowed values for the k-th setting. Before applying the GP method, a training set of $2M$ settings/cost pairs is constructed using the DE method.

The greatest limitation of a GP is the computational cost involved in training the model, as the required computation time scales as $\mathcal{O}(P^3)$, where P is the number of training data points, hence the method may become impractical for large datasets.

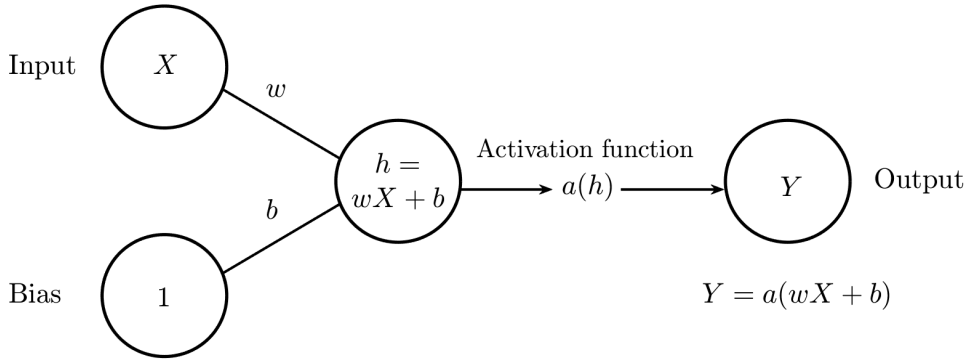

Figure 4.4: The simple perceptron. An input X is combined with a constant bias, which are weight w and b, respectively. An activation function $a(h)$ operates on the combination $h = wX + b$ to produce an output y.

4.3.3 Artificial Neural Networks

NNs are an example of a function approximator which take the form of an interconnected network of nodes [99, 114]. The NN produces a 'black-box' mapping between an input $\mathbf{X}$ and an output Y. In our context, the inputs are settings vectors and the outputs are the associated costs. The mapping is determined by the structure and weights of connections in the network. This connection structure is intrinsically linear however NNs may be extended to approximating non-linear functions by incorporating a non-linear 'activation function' $a(x)$. A neuron calculates the weighted sum of its inputs, $h = \sum (\text{input} * \text{weight} + \text{bias})$, and feeds forward a value depending on some activation function, for instance, if $h > 0$, feed forward h. This process is illustrated in figure 4.4 for a single node with only one input and one output; this network architecture is referred to as a 'simple perceptron'. The activation function described earlier is named the 'Regularised Linear Unit' (ReLU) activation function and suits binary classification, but is not well suited to functions for which inputs can take values across a continuous range. We instead choose the Gaussian Error Linear

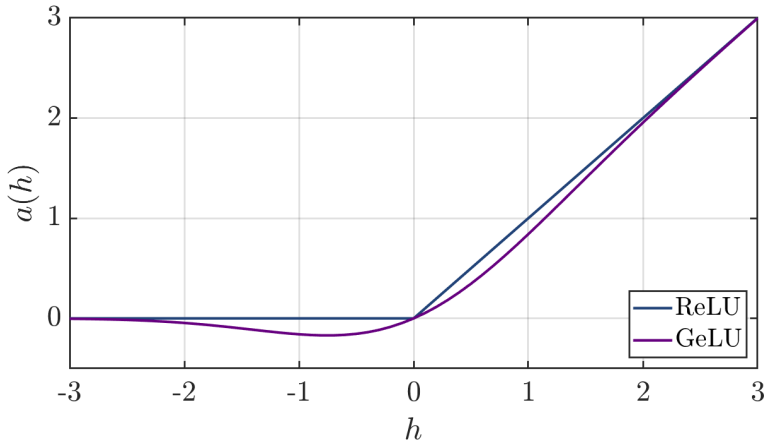

Figure 4.5: The ReLU and GELU activation functions.

Unit (GELU) activation function for each node [115]:

$$a(h) = 0.5h + 0.5h \tanh\left(\sqrt{\frac{2}{\pi}}\left(h + 0.044715h^3\right)\right) . \tag{4.3}$$

This continuous function is a popular choice for data which is subject to normally-distributed stochastic variation, which suits our experimental context [116]. The ReLU and GeLU functions are illustrated in figure 4.5.

In addition, the structure and scale of the NN must be appropriate for the complexity and size of the vector inputs. We choose a network comprised of 3 hidden layers of 8 fully-connected neurons, inspired by [117], which is sufficient for the number of settings that we optimise in this context (a maximum of 35). A deep network comprising hidden layers and multiple inputs is illustrated in figure 4.6.

In supervised learning, a neural network is trained using a set of data comprising previously run inputs and their known outcomes. We build an initial training set of $2M$ settings/cost pairs using the DE method. Training consists of an iterative procedure of passing an input through the network and calculating the agreement, using a loss function, between the predicted output y and the true output y_{true}; this is referred to as forward propagation. We use the squared-error loss function of the

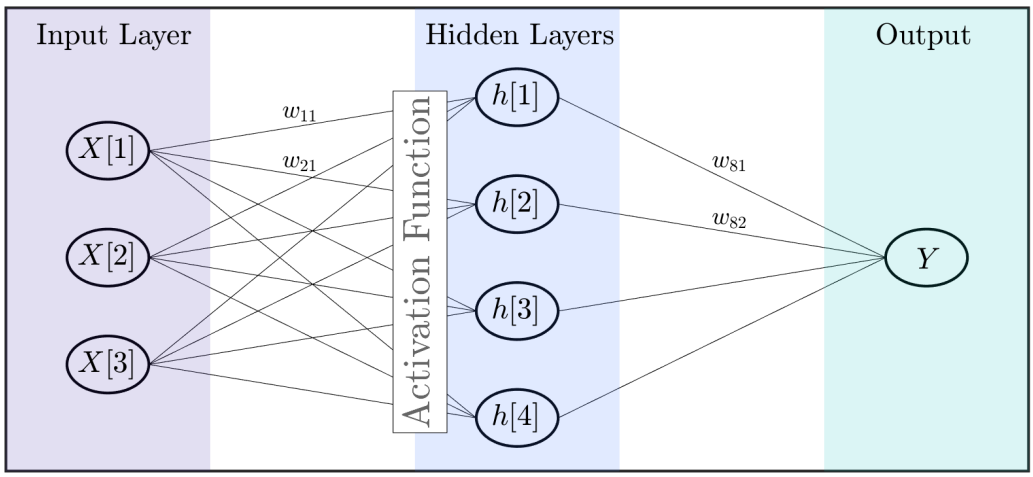

Figure 4.6: Structure of an Artificial Neural Network. Inputs $X[i]$ are connected to nodes in hidden layers, where the weights w_{ij} and inputs are fed through a specific activation function. Finally, outputs from nodes $h[j]$ are fed to a final output node Y.

form

$$L\left(\{y_{\text{true}}, y\}; \{w, b\}\right) = \sum_{i=1}^{P} \left(y_{\text{true},i} - y_i\right)^2 \quad , \tag{4.4}$$

which calculates the sum of the squared deviations between the P true and predicted outputs given the network weights and biases $\{w, b\}$. The weights and biases are updated using a gradient descent method, such that

$$\lambda := \lambda - \alpha \, \frac{\partial L\left(\{y_{\text{true}}, y\}; \{w, b\}\right)}{\partial \lambda} \quad , \tag{4.5}$$

where λ represents the model parameters (weights and biases) and α is the learning rate; this stage of training is referred to as back-propagation.

As an improvement to backpropagation and stochastic gradient descent methods, we utilise the Adam optimisation method to train the NN [118]. In comparison to standard gradient descent methods, the Adam method considers higher-order moments of the loss function with respect to each network parameter [119], which often leads to a comparatively faster learning rate [118]. The method is straightforward

to implement and is computationally efficient; the method is also appropriate for problems with very noisy or sparse gradients.

When training the network, a subset of the overall data set is ignored. Following training, this additional set of data (cross-validation set), where the true outcome of each input is also known, is used to evaluate the accuracy of the model before it is applied to new incoming data. If the accuracy of the model, when predicting the costs associated with the cross-validation set, falls below a threshold, further training is performed.

Once a model has been trained and cross-validated, we use the model to predict the outcome of input data and, in our case, use this correspondence to predict the required input to find an optimum output. Specifically, we use the trained NN to predict optimal settings $\mathbf{X}_*$. A sequence is then run using $\mathbf{X}_*$ and the cost Y_* is measured. This settings/cost pair is then used to refine the NN for future sequences.

4.4 Results

We applied the algorithms presented above to optimise the atomic cooling processes utilised in the production of BECs. We begin with the optimisation of evaporative cooling in the magnetic quadrupole and TOP traps. This optimisation also identifies the settings that most strongly affect the cost function. Similarly, we optimise the cMOT laser cooling stage. We combine the sensitive settings in both the laser cooling and evaporative cooling stages to perform a full optimisation of all cooling processes involved in the production of a BEC. Finally, we alter the cost function to find settings which produce a BEC of a threshold atom number with the shortest achievable sequence duration, and later to maximise the number of atoms at a desired temperature.

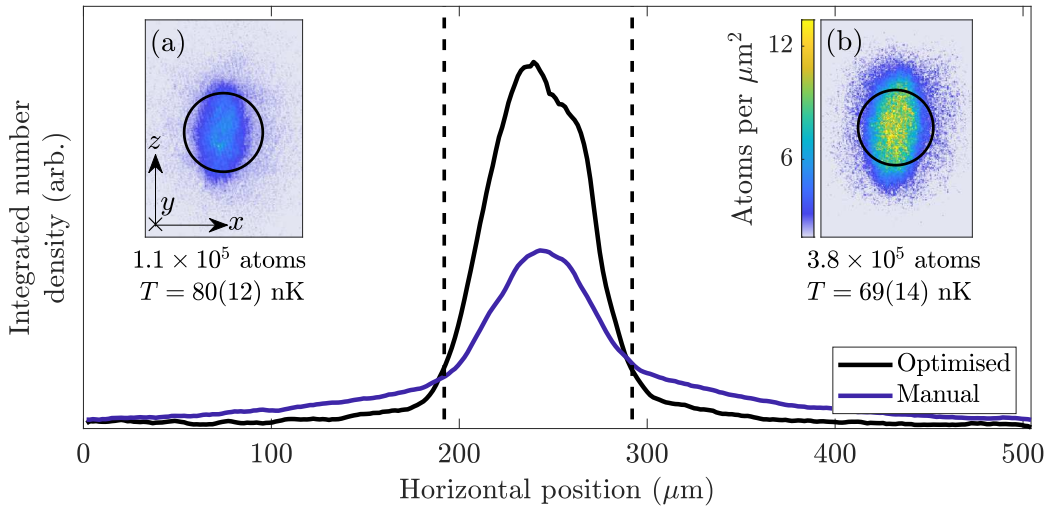

Figure 4.7: Results of optimisation via machine learning vs manual optimisation. We compare the absorption images of a manually-optimised BEC (a) and a BEC where the evaporative cooling stages of both the quadrupole and TOP traps have been optimised using the GP method (b). The BEC atom numbers are shown below the images. The plot shows a direct comparison of the images integrated along the direction of gravity, $\hat{\mathbf{e}}_z$. The ROI, within which atoms are counted in the cost function, is indicated by the straight, dashed lines.

4.4.1 Optimising evaporative cooling

Prior to machine learning optimisation, our manually-optimised settings produce a BEC of 1.1×10^5 atoms, as shown in figure 4.7 (a). This produces a cost of 8.9 when using a circular ROI of radius 50 µm located about the cloud centre after 25 ms of free fall. These settings can be used as a starting point for automated optimisation, leading to rapid convergence towards the optimum settings and providing a useful way to quickly tune the experiment. However, to properly evaluate the different learners, we begin each optimisation using completely randomised settings. These initial settings produce no visible atom cloud. Figure 4.8 shows the cost vs experimental run number. Optimisation is continued until the early stopping criteria are satisfied, which limits the optimisation process to a maximum duration of approximately 3 hours.

Performing one optimisation routine for each method, the GP method converged to a BEC of 3.8×10^5 atoms after 47 sequences, which is illustrated in figures 4.7 (b)

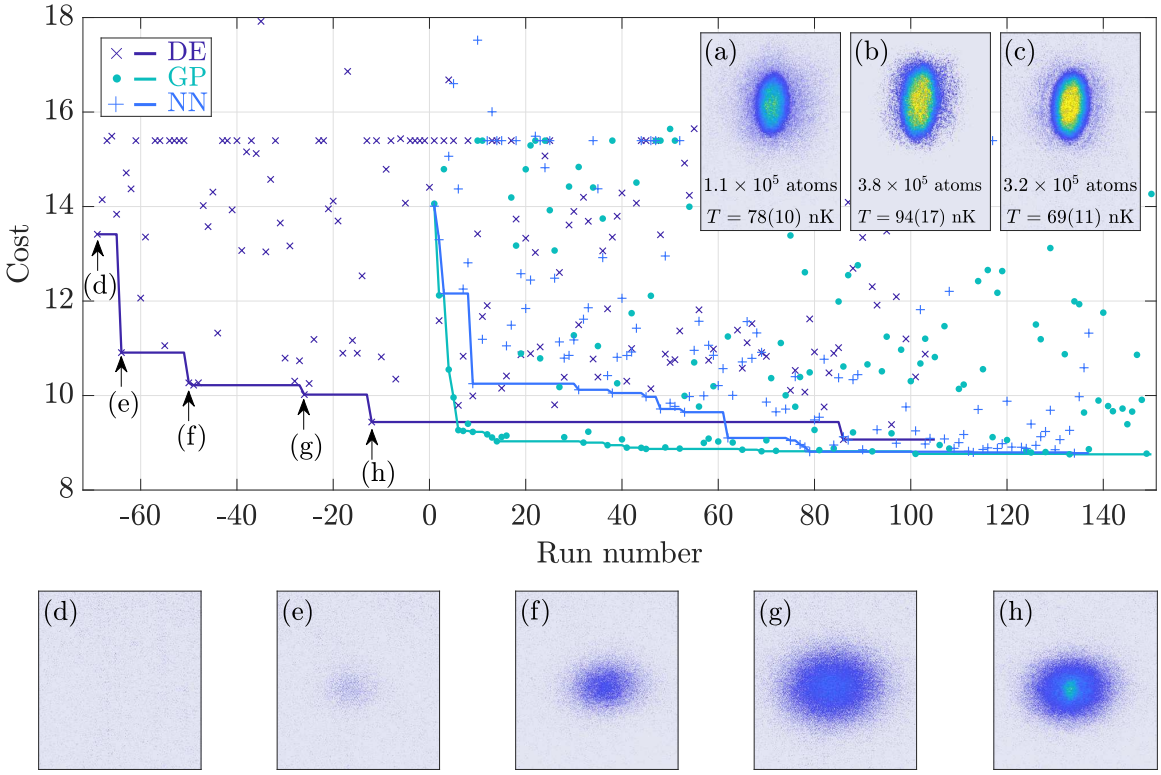

Figure 4.8: Optimising the magnetic quadrupole and TOP evaporative cooling stages beginning from random settings. Data points for the measured cost are illustrated as × (DE), • (GP) and + (NN). In addition, the moving minimum for each of the three methods is indicated by the solid lines. Inset (a)-(c): absorption images of BECs produced using the best settings found for DE, GP and NN-based optimisation respectively. Sequences used in building the training set using the DE method are labelled with negative numbers. Absorption images below correspond to points labelled (d)-(h). These images illustrate the progression of the optimisation from initial settings, which did not produce any trapped atoms, towards finding settings which produce a BEC. The images use the same colour scheme as that used in figure 4.7.

and 4.8 (b). DE did not converge within the time limit but was still successful in producing a small BEC, as shown in figure 4.8 (a). The NN method produced a BEC of 3.2×10^5 atoms after 117 sequences (figure 4.8 (c)) with a rate of convergence which is between those of the GP and DE methods[2]. For both the GP and NN methods, the optimisation procedure resulting in a factor of 3 increase in BEC atom number as compared to the manually-optimised settings. The settings producing the best cost are shown in table 4.1 with the original settings used prior to optimisation shown in braces next to each entry. Figure 4.9 (a) & (b), illustrate the progression of the experimental settings during the optimisation, namely the quadrupole current I_Q and RF knife frequency, respectively. The settings are plotted against the duration of each substage.

Table 4.1: The best settings found for evaporative cooling stages in the magnetic quadrupole (Quad) and TOP traps; these were found using the GP method but are very similar to those found using the NN method. The values shown define points which are linearly interpolated to produce the evaporation instructions. Numbers in parentheses represent the manually-optimised settings used prior to the optimisation. Values shown without parentheses were not included in the optimisation.

	Substage	Duration (s)	I_Q (A)	RF Knife (MHz)	B_x (G)	Anisotropy
Quad	0	0	323 (315)	120		
	1	18	323 (315)	15 (18)		
TOP	2	0	83 (60)	26 (32)	2.6 (3.6)	0 (0)
	3	0.08 (0.08)	142 (131)	29 (26)	19 (18)	0 (0)
	4	8.1 (7.0)	237 (226)	9.1 (9)	6.6 (7.8)	0.06 (0)
	5	1.1 (0.8)	213 (226)	10 (8.5)	6.3 (7.8)	-0.15 (0)
	6	1.8 (1.8)	249 (226)	14 (7.8)	9.9 (7.8)	0.04 (0)
	7	6.3 (3.3)	222 (226)	9.5 (6.7)	9.0 (7.8)	0.09 (0)
	8	5.5 (1.5)	200 (226)	6.9 (6.5)	7.8 (7.8)	0.11 (0)

The cloud density profile after TOF expansion becomes bimodal as the cost function drops below approximately 9.2, indicating the presence of a BEC component. This threshold is achieved after 156 sequences (DE), 14 sequences (GP) and 75 se-

[2]For both the GP and NN methods, the quoted number of sequences does not include the training set of $2M = 70$ sequences which was produced using DE.

quences (NN). As there is a random element to how each method chooses points to evaluate, it is possible that one model may have chanced upon good settings early in the optimisation procedure which then strongly guided its subsequent choices. Repeating the optimisations with many random initialisations is required to fully evaluate the performance of each method. Overall, the relative convergence rates of the methods differ significantly, and as expected, thus no further measurements are necessary in this case.

Given the desirability of short routines, and as illustrated by the relative rates of convergence between the methods, we conclude that the GP regression method is of greatest utility in our experimental context. Our optimisation routine produces a relatively small amount of training data which, consequently, may reduce the suitability of an NN-based method. In a wider context, the slower convergence of the NN, as compared to GP, is representative of the large amount of data required to train a fully-connected network [120].

Within only a few hours, the result of the optimisation procedure is a greater than threefold improvement in the BEC atom number, as compared to a BEC produced with settings which have been improved manually and gradually over many years. This improvement is illustrated in figure 4.7 (a) & (b), which compare BECs produced using the evaporation settings before and after optimisation, respectively. Figure 4.7 also demonstrates the merit of defining a small ROI, which discounts atoms from the broader, thermal fraction of the atomic distribution.

4.4.2 Sensitivities

We utilise the cost landscape fitted by the GP learner to determine the sensitivity of the different settings. As detailed in section 4.3.2, the parameters η_i provide a measure of how steeply the cost function varies about the predicted minimum with respect to each setting. As a heuristic indicator of sensitivity, we define a setting to

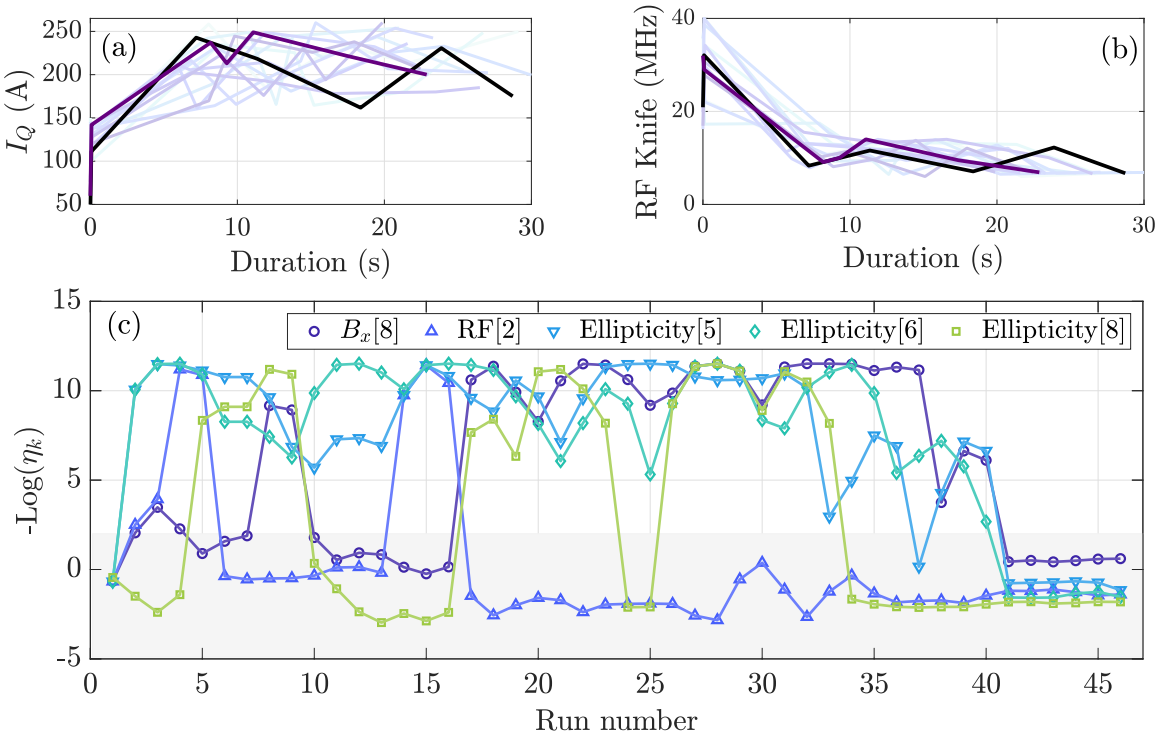

Figure 4.9: (a) & (b) The progression of the quadrupole current I_Q and RF knife frequency settings produced during the optimisation, respectively. The settings are plotted against the duration of the evaporative cooling stage. Darker colours indicate settings produced later into the optimisation procedure. The minimum cost is achieved with the settings shown in black and the manually-optimised settings trajectory in purple. (c) The evolution of the 5 most sensitive η_i as more data is added during the optimisation routine. The settings shown are indexed by a number which indicates the substage of the evaporative cooling stage, as given in table 4.1. The shaded area indicates the region of $-\text{Log}(\eta_i) < 2$ within which a setting is deemed sensitive.

be sensitive if the associated η_i is greater than $\exp(-2)$. Figure 4.9 (c) illustrates the convergence of η_i as more data is added during the evaporative cooling optimisation; this also indicates that knowledge of the parameter space, and hence the accuracy of the GP fit, is improved with more training data. For clarity, only the five most sensitive settings are shown.

We find that the cost is highly sensitive to the final amplitude of the magnetic field in the TOP trap (B_x[8]), as well as the initial (RF[2]) and final (RF[8]) radiofrequencies of the knife. This can be understood as follows: the initial frequency

determines the threshold energy above which atoms are ejected from the trap; this frequency must be sufficiently high so as not to immediately cut away a large number of atoms when the RF knife is first turned on and evaporation begins. A combination of the last knife frequency and TOP amplitude determines the final, lowest energy cut in the evaporation ramp. If this is too high, the cloud is hotter and fewer atoms accumulate in the ground state. If this is too low, the RF knife unneccesarily ejects atoms which would otherwise have contributed to the BEC component. The cost is also sensitive to the final RF knife cut in the quadrupole trap, as this determines the temperature of the atomic cloud when it is loaded into the TOP trap.

Surprisingly, we find the cost is highly sensitive to the TOP field anisotropy during certain substages. This setting was fixed to 0 during previous manual optimisation, as this was expected to yield the best results. However, the optimised settings presented in table 4.1 include anisotropies ranging from -0.15 to 0.11, and thus differ significantly from the isotropic ($\epsilon = 0$) case. When investigating why anisotropy may be beneficial to the cooling sequence, we found the x and y positions of trapped gases in the quadrupole and TOP traps to disagree. This indicates that the rotation axis of the TOP field is not perfectly aligned with the symmetric axis of the quadrupole field, which increases the displacement between the energy minima of an atom in these fields. In addition to any centre-of-mass motion of the cloud, which may be induced as the cloud is transferred from the quadrupole to the TOP trap, other multipole oscillations in the cloud may be excited. We postulate that a non-zero anisotropy in the TOP field may act to overlap the potential minima, or to provide an asymmetric confinement force, so as to eradicate or damp excitations in the cloud which would otherwise affect the efficiency of subsequent evaporative cooling. The anisotropy of the TOP field can also counter-balance any asymmetry in the quadrupole field. These unexpected results produced by the optimisation procedure, which at first seem counterintuitive, can provide hints to the experimentalist as to where imperfections might

exist in the apparatus.

4.4.3 Simultaneous optimisation of laser cooling and evaporative cooling

For the remainder of this chapter, we focus on the GP regression method, as this is the most rapidly converging of the methods tested in our experimental context. We optimise the cMOT stage, approximately doubling the number of laser cooled atoms which arrive in the UHV glass cell after magnetic transport. To achieve this, we discretise the cMOT stage into 8 independent substages and vary the current of the magnetic quadrupole coils I_Q and the detuning from resonance of the cooling light. Figure 4.10 (Laser cooling panel) illustrates the convergence of the four most sensitive η_i of this stage as the optimisation progresses. The most sensitive settings are the initial and final quadrupole currents ($I_Q[1]$ and $I_Q[8]$) and detunings from resonance of the cooling light (Detuning[1] and Detuning[8]).

The number of sequences required for the GP method to converge increases with the number of settings. In addition, the computation time scales as the cube of the number of settings/cost pairs over which the GP fits. Given this, it is advantageous to reduce the number of settings as far as is reasonable without compromising the outcome of the optimisation. Having determined the 18 most sensitive settings across the laser cooling and evaporative cooling stages, we are able to perform simultaneous optimisation of all cooling stages in a reasonable time. We again utilise the DE method to produce a training set of $2M = 36$ settings/cost pairs and the values of insensitive settings in both stages were fixed to those found during the separate optimisation routines.

Using the GP learner, and by optimising only the sensitive settings, we are able to produce a BEC from random initial settings after only 12 experimental sequences (following the 36 runs used in building the training set). The optimisation produces a

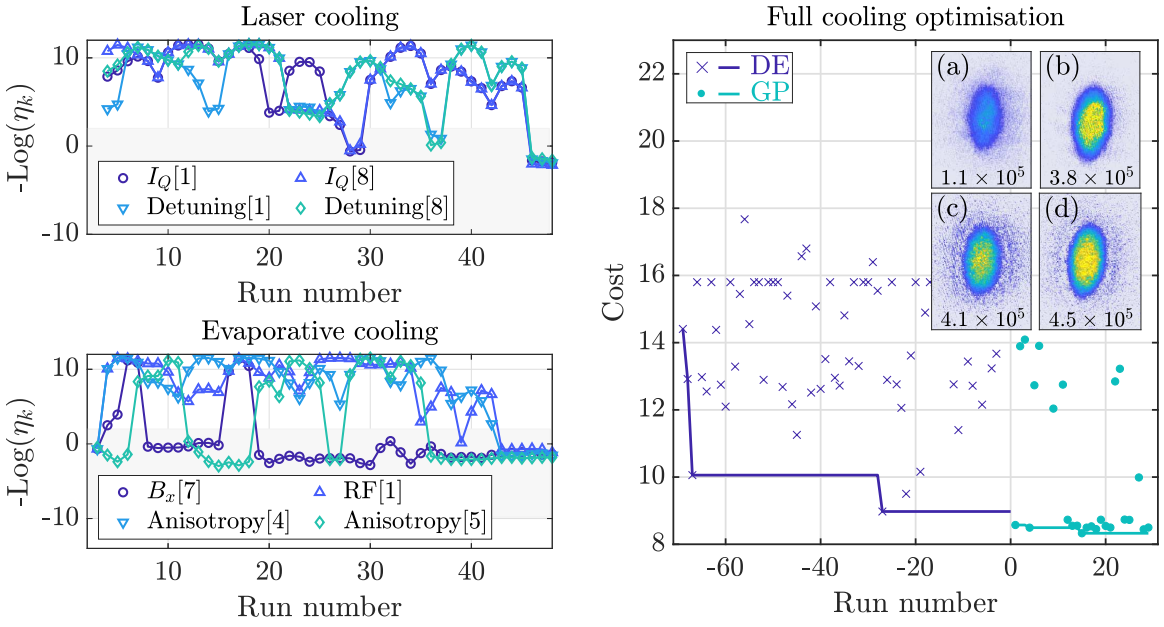

Figure 4.10: Cost vs run number for optimisation of all cooling processes, using the GP method. Laser cooling panel: convergence of the 4 most sensitive η_i during optimisation of laser cooling (cMOT). Evaporative cooling panel: convergence of the 4 most sensitive η_i during optimisation of evaporative cooling. Right: The cost versus run number for the overall cooling optimisation, using the 18 most sensitive settings, for the initial DE method (×) and the subsequent GP method (•). The moving minimum cost is illustrated by the solid line. Sequences used in building the training set using the DE method are again labelled with negative numbers. Insets: (a) - manually optimised BEC, (b) - BEC following evaporative cooling optimisation, (c) - BEC following laser cooling optimisation and (d) - BEC following the full cooling optimisation. Values correspond to the BEC atom numbers in the clouds shown. The images use the same colour scheme as that used in figure 4.7.

BEC with an atom number of 4.5×10^5, which is greater than atom numbers produced in the optimisation of the seperate cooling stages. Figure 4.10 (a)-(d) illustrate the improvements in BEC atom number as we have optimised the stages individually and collectively. This faster optimisation routine, using only the sensitive settings, can allow a user to perform quick and regular re-optimisation to keep an experiment working to the best of its capability.

4.4.4 Tailoring the cost function to other aims

A maximised atom number in the BEC is often desirable and this motivated our earlier choice of cost function. However, depending on the scenario, other quantities may be of greater importance. For example, when performing alignment of optical elements, it is more useful to maximise the repetition rate of the experiment.

4.4.4.1 Minimising sequence duration

We use our optimisation routine to find settings which produce a BEC of a threshold atom number in the shortest possible time. In general, BEC experiments have sequence durations ranging from a few seconds to minutes, depending on the implementation details of each apparatus. We use the cost function

$$f(\tilde{N}) = -\left(1 + \arctan(\tilde{N} - \tilde{N}_0)\right) / \left(1 + \tilde{t}\right) \ , \tag{4.6}$$

where $\tilde{N}_0$ is a threshold number of atoms within our ROI, which we choose to correspond to a BEC of 1×10^5 atoms, and $\tilde{t}$ is the sequence duration. This cost function rewards a short sequence time and penalises settings which do not produce a BEC of a threshold atom number; there is also little reward for producing a BEC with an excess of atoms. With no other changes to the optimisation routine, the optimised settings produce a BEC of 9.6×10^4 atoms and reduce our overall sequence time

from 58 s to 46 s, a time saving of over 20 %. This demonstrates the power of online optimisation to reconfigure an apparatus to achieve the aims of the user.

4.4.4.2 Minimising temperature

We use our machine learner to find settings which minimise the temperature of the ultracold gas. Temperature cannot be made arbitrarily low, as $N \to 0$ for $T \to 0$ in an evaporative cooling process, so we incorporate a threshold number N_0 into the cost function. We define the cost function $f(N, T)$ to be

$$\begin{aligned} &\text{if} \quad N > N_0 \\ &\qquad f(N, T) = \log(T/1\,\mu\text{K}) \\ &\text{else} \\ &\qquad f(N, T) = -0.2 \log(N) \end{aligned} \tag{4.7}$$

where T is the cloud temperature and N is the BEC atom number. Figure 4.11 (a) illustrates this cost as a function of atom number and temperature. For sufficient atom numbers, the cost depends only on temperature and encourages the learner to reduce T. For smaller atom numbers, the fits from which temperature is inferred can fail, and so only the atom number itself is used to determine the cost. We take $N_0 = 5 \times 10^3$ as a lower bound for the number of atoms in the BEC. The prefactor of 0.2 minimises the discontinuity in the cost either side of the threshold atom number, which assists our gradient-based method in finding the optimal parameter set.

As shown in figure 4.11 (d), optimising for temperature produces a 37(12) nK BEC of around 6.5×10^3 atoms. The cost function guides the learner to produce the coldest possible cloud which satisfies the number threshold. The resulting cloud is significantly colder than that produced using the optimisation detailed in section 4.4.1 (see figure 4.11 (c)).

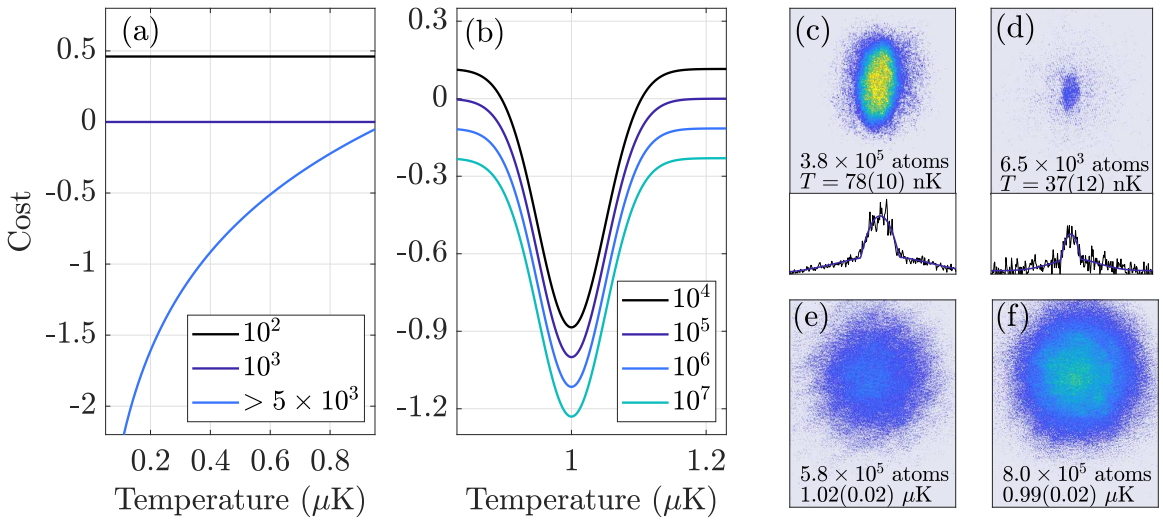

Figure 4.11: Results of optimisations detailed in sections 4.4.4.2 & 4.4.4.3. (a)-(b) Cost vs atom number and temperature for the cost functions presented in sections 4.4.4.2 & 4.4.4.3, respectively. Values in the legend of each plot indicate the BEC atom number and temperature. (c)-(d), upper) Absorption images of BECs produced using the optimisation routines presented in section 4.4.1 & 4.4.4.2, respectively. (c)-(d), lower) Bimodal fits (purple) to the atomic density profiles (black) extracted from the absorption images above.(e)-(f) 1 µK clouds produced using a truncated version of the evaporative cooling routine presented in section 4.4.1 and by the optimisation presented in 4.4.4.2, respectively. Values in the legend of each plot indicate the temperature and total atom number.

4.4.4.3 Maximising atom number at a specific temperature

Other optimisations could also be conceived, such as maximising the atom number of a thermal cloud at a specified temperature. We now use the cost function

$$f(N,T) = -\exp\left(-\left(\frac{T}{T_0}-1\right)^2\right) - \log(N) \quad , \tag{4.8}$$

where T is the temperature, $T_0 = 1\,\mu\text{K}$ is the target temperature and N is the total atom number. This cost function favours the production of a 1 µK cloud with the greatest atom number, and is illustrated in figure 4.11 (b) as a function of temperature for different atom numbers.

Figure 4.11 (f) shows an image of a thermal cloud produced by settings optimised in this way and, for comparison, figure 4.11 (e) shows a 1 µK cloud produced by truncating the evaporative cooling ramp from table 4.1. The 1 µK cloud produced through this optimisation has an atom number that is 38 % larger. Another variant of this scheme could be to minimise T for a thermal gas with a specified atom number, which would be possible with only a minor adjustment to the cost function described above.

4.5 Conclusion

The value of machine learning in finding patterns and optima in data which depends on many parameters is apparent across multiple fields of research [116]. In our specific case, machine learning has provided a means for autonomous experimental optimisation. We have compared the convergence rate of three optimisation methods and, for the first time, we have optimised all cooling stages involved in a quantum gas experiment simultaneously. The optimisation is quick and achieves our aim of increasing the atom number in a BEC, which is beneficial for future experiments. Furthermore,

machine learning methods now form part of the day-to-day operation of the experiment and subsequent studies have concerned optimisation of evaporative cooling in the TAAP trap and other stages of the experimental sequence.

We have used the GP method to identify the sensitive settings within each cooling stage. By restricting the attention of the learner to only consider these sensitive settings, it becomes possible to optimise the experiment as a whole with only a small amount of training time. Optimisation can be performed within an hour, allowing daily optimisation if necessary to maintain peak performance for producing consistent, high-quality data. Long-term drifts which would otherwise degrade the apparatus' performance can thus be easily mitigated, by scheduling regular optimisation routines.

Certain features of our optimal solutions are counterintuitive: improvements arising from an anisotropy TOP field during the evaporative cooling stage were not expected and would not generally be explored. These features may indicate underlying physics, or may allude to the presence of imperfections in the experimental apparatus.

Lastly, the point of convergence, or optimum, may be one for which the sensitivity of any parameter is extremely high. While we hope to find the global minimum of the cost function, it is of little experimental value if a perturbation from the prescribed experimental settings leads to a sharp response in the cost. The stability of the solution can be evaluated by assessing the average cost over multiple runs for each input and building separate models for both the expectation $\mathrm{E}[Y]$ and the variance $\mathrm{Var}[Y]$. These can be jointly optimised to produce a solution which not only works to achieve the user's optimisation aim but also reduces shot-to-shot fluctuations which limit the reliability of an experiment. To date, however, we have observed that the optima are no less stable than the previous, manually-optimised values.

5

Realising a species-selective double well

In this chapter, we present the experimental realisation of a species-selective double-well potential using MRF-dressed potentials. This chapter follows work detailed in reference [36]. We confine an ultracold mixture of ^{87}Rb in hyperfine ground states with $F = 1$ and $F = 2$, and manipulate each state independently through control of the amplitudes and phases of the RF field. This method is widely applicable to atoms which have differing magnetic properties [43,54,65,66] and is a promising technique to investigate impurity physics [121,122] or to realise sub-nK thermometry schemes [123–125]. We perform additional experiments to verify that this particular mixture is collisionally stable, in which we observe no inelastic loss [36]. These experiments were motivated by results of an earlier investigation on this apparatus which identified strong inelastic loss in an RF-dressed mixture of ^{85}Rb and ^{87}Rb atoms [43].

5.1 Introduction

Cold-atom experiments are a valuable tool to investigate many-body quantum systems [1,2]. For example, mixtures of cold atoms have been used to study the superfluid properties of bosons and fermions [7, 126–129], including the immiscibility of quantum fluids [130, 131]. In previous work on our experimental apparatus, mixtures were considered in the context of impurity physics, towards implementing quantum probes of complex systems [65, 132]. Impurity physics, in which a minority species interacts with a large reservoir of a second species, can be studied via the immersion of ancillary probes; this necessitates a means of controlling the separate constituents of the mixture [133]. Furthermore, species-selective control within double-well potentials may be used to identify several physical effects, including the quasiparticle excitation spectrum of a BEC [121], the decoherence of impurities coupled to open quantum systems [122] and to realise sub-nK thermometry [123–125]. Many optical methods of species-selective spatial manipulation have been investigated, including optical tweezers [134, 135], holographic light fields and lattices [136–138]. These methods are well established but are unsuitable when the optical frequencies required to manipulate the separate components are similar, as is the case for the hyperfine states of ^{87}Rb with $F = 1$ and $F = 2$, as scattering resonant light induces significant heating of the mixture. This can be suppressed using high-power lasers detuned far from resonance but comes at the expense of severely reducing the species-selectivity of the potentials.

As discussed in Chapter 2, atoms in a static magnetic field can be confined by the application of a strong RF field [40, 139]. Additionally, dressing atoms with MRF fields significantly extends the range of possible trapping geometries, for example to double-well potentials [34, 58] and lattices [71]. RF-dressed potentials are species-selective for mixtures of atoms with differing magnetic moments, for instance where the magnitude or sign of the Landé g-factor for each constituent is distinct [43, 54,

65, 66]. Exploiting this feature, we implement a species-selective double well using MRF-dressed potentials and manipulate the spatial distribution of the ^{87}Rb $F = 1$ and $F = 2$ mixture constituents.

Recent theoretical [140] and experimental [43] studies have shown that not all mixtures are collisionally stable when confined in RF-dressed potentials. In this chapter, we find our RF-dressed mixture of ^{87}Rb atoms in hyperfine states with $F = 1$ and $F = 2$ to be long-lived, thus highlighting the merit of this atomic mixture for future experiments in RF-dressed potentials.

This chapter is structured as follows. In section 5.2 we briefly revisit the experimental procedure used to produce mixtures of ^{87}Rb atoms in two hyperfine states. In section 5.3 we present species-selective manipulations of a mixture of ^{87}Rb atoms in states with $F = 1$ and $F = 2$ via control of the MRF-dressing fields amplitudes and polarisations. In section 5.4 we show that this mixture is collisionally stable against inelastic loss.

5.2 Experimental methods

We produce cold atomic gases of ^{87}Rb atoms in the state $F = 1$, $\tilde{m}_F = 1$, at approximately 0.4 µK, which are trapped in a RF-dressed potential defined by a single RF field at 2 MHz. We implement our double-well potential by applying MRF fields using current-carrying coil pairs, illustrated in Chapter 3, figure 3.8 (purple coils), which surround the UHV glass cell. Amplitudes and frequencies of the MRF fields are discussed in section 5.3.

To produce a mixture of atoms in different hyperfine states, we apply a pulse of MW radiation using a patch antenna which is resonant with the hyperfine splitting of ^{87}Rb at approximately 6.8 GHz. The MW radiation is sourced from a commer-

cial synthesizer[1] followed by a 20 W amplifier[2]. A pulse at 6.834 68 GHz transfers a fraction of atoms from the $F = 1$, $\tilde{m}_F = 1$ state to the $F = 2$, $\tilde{m}_F = 1$ state. The fraction of atoms transferred, and hence the relative densities of the two states, can be controlled via the MW pulse duration. We identify the relevant transition from a spectrum of MW transitions, as shown in figure 5.1 (d), which is produced by applying a 40 ms MW pulse at a given frequency and measuring the resulting atom number in the $F = 2$ state. The features of this spectrum have been investigated elsewhere [53].

We image both states in the same experimental sequence. First, we image the $F = 2$ cloud using light resonant with the $F = 2$ to $F' = 3$ transition in the D2 manifold (cooling light) [80]. Excitation to untrapped substates of the $F' = 3$ level causes the imaged atoms to fall from the trap. Atoms with $F = 1$, however, are dark to the imaging transition and are thus unaffected during this first image. Next, we pump atoms with $F = 1$ to the $F = 2$ level using light resonant with the $F = 1$ to $F' = 2$ transition in the D2 manifold (repump light) immediately before they are imaged with cooling light. The second image contains absorption from both populations but, as the two images are taken approximately 6 ms apart, atoms ejected during the first image are sufficiently far from the trap centre to resolve the $F = 2$ distribution. Atomic distributions are extracted from both images using the protocol outlined in Chapter 3, section 3.6.

5.3 A species-selective double-well potential

We now describe our species-selective double-well potential, which we demonstrate for a single species, ^{87}Rb, but with atoms in two different hyperfine states with $F = 1$ and $F = 2$. Our experimental implementation follows a theoretical proposal in

[1] DS Instruments SG12000PRO
[2] Microwave Amps, AM53-6.4-7-43-43

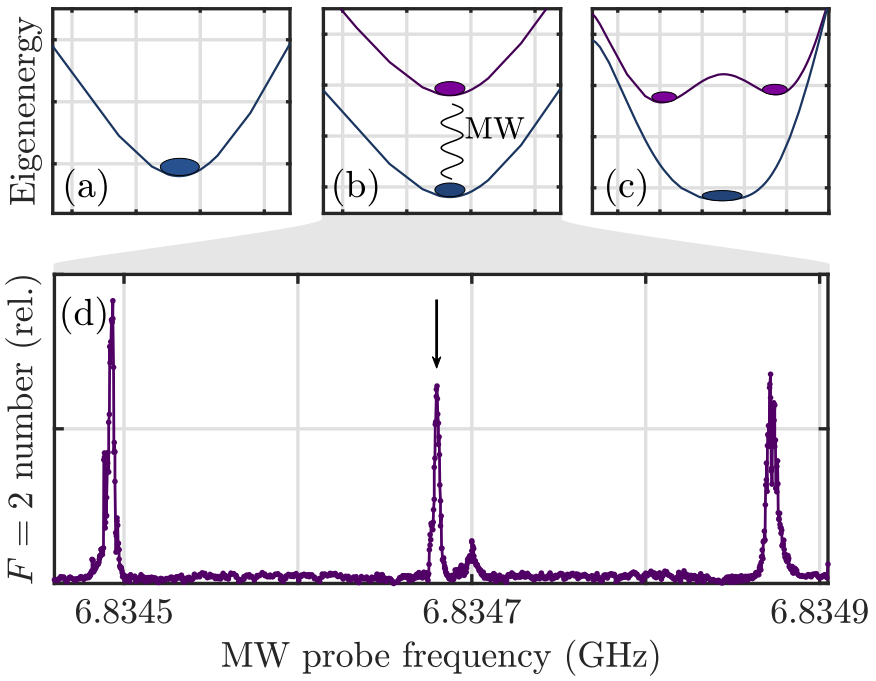

Figure 5.1: (a)-(c) Illustration of a typical experimental sequence where (a) are the dressed eigenenergies of atoms in the $F = 1$, $\tilde{m}_F = 1$ state (dark blue); (b) illustrates the transfer of a fraction of atoms into the $F = 2$, $\tilde{m}_F = 1$ state (purple) following a MW pulse; and (c) shows the potentials for each state as they are independently manipulated. (d) Spectroscopic measurements of the MW transitions between states with $F = 1$, $\tilde{m}_F = 1$ to RF-dressed eigenstates with $F = 2$. The MW transition at 6.834 68 GHz is marked by an arrow.

reference [57].

To create our double-well potential, we apply 3 RF components with frequencies $\omega_i/2\pi = \{1.8\,\text{MHz}, 2\,\text{MHz}$ and $2.2\,\text{MHz}\}$ and amplitudes $(A_i + B_i) = \{326\,\text{mG}, 374\,\text{mG}$ and $440\,\text{mG}\}$, for $i = \{1, 2, 3\}$, which correspond to Rabi frequencies of $\{114\,\text{kHz}, 131\,\text{kHz}$ and $154\,\text{kHz}\}$; these RF fields are linearly polarised along $\hat{\mathbf{e}}_x$. Each RF field component i creates an avoided crossing near the position $\mathbf{r}_i$ where the species-dependent resonance condition $\hbar\omega_i = |g_F|\mu_\text{B}B(\mathbf{r}_i)$ is satisfied, as shown in Chapter 2, figure 2.5. Consequently, the RF field at 2 MHz defines the 'barrier' of the double-well potential.

As the states couple separately to σ^+ and σ^- components of the RF field, changing the polarisation of the 2 MHz field enables the barrier height to be independently controlled for each mixture constituent, for instance, to raise the barrier for one state while simultaneously lowering it for the other. Figure 5.2 (a)-(c) show the deformation of the potentials as the polarisation of the frequency component forming the barrier is changed. We achieve this by the addition of an RF field component at 2 MHz, linearly polarised along $\hat{\mathbf{e}}_y$ and with amplitude $(B_2 - A_2)$, which alters the amplitudes of σ^+ and σ^- components of the RF field and independently modifies the potential energies for $F = 1$ and $F = 2$. Figure 5.2 (d) and (e) show vertical slices of absorption images of the trapped $F = 1$ and $F = 2$ clouds, respectively, which display the expected spatial distribution as the balance of 2 MHz fields along $\hat{\mathbf{e}}_x$ and $\hat{\mathbf{e}}_y$ are controlled.

When no RF field component at the frequency of the barrier is applied along $\hat{\mathbf{e}}_y$, the polarisation is linear and the coupling strength for $F = 1$ and $F = 2$ states is equal[3,4]. As a consequence, raising or lowering the barrier via the amplitude of the linearly polarised 2 MHz RF field along $\hat{\mathbf{e}}_x$ modifies the eigenstates for both states equally. Figure 5.2 (f)-(h) illustrates this effect and the consequent deformation

[3]Up to the small difference in $|g_F|$ arising from the nuclear spin.

[4]A linearly polarised field can be decomposed into equal amplitudes of σ^+ and σ^- polarisation components.

of the potentials as the barrier field amplitude is reduced from 500 mG (175 kHz) to 180 mG (63 kHz), with the corresponding Rabi frequencies shown in parentheses. Figure 5.2 (i) and (j) show vertical slices of absorption images of the trapped $F = 1$ and $F = 2$ clouds, respectively, as a function of the barrier amplitude $A_2 + B_2$, which demonstrates the equivalence of potentials for both states.

This section has described our realisation of a species-selective double-well potential, and how its properties were engineered using the amplitude and polarisation of dressing RF fields. In particular, we formed combinations of single- and double-well potentials for the two mixture constituents, via methods which are applicable to any mixture for which $\mathrm{sgn}(g_F)$ is distinct. Combined with our previous work on methods to manipulate mixtures where $|g_F|$ differs [43, 65], we have a set of manipulations applicable to any mixtures for which the magnetic nature of the constituents is distinct.

5.4 Collisional stability of rf-dressed mixtures

The species-selective manipulations, and their use in future experiments, are only of practical value if the mixture does not suffer large inelastic losses. To begin consideration of this issue we revisit results reported in reference [43], where rapid inelastic loss was observed in an RF-dressed mixture of ^{87}Rb and ^{85}Rb. We then present experimental findings concerning the collisional stability of an RF-dressed mixture of ^{87}Rb atoms in the $F = 1$ and $F = 2$ hyperfine states.

5.4.1 A dressed mixture of ^{87}Rb and ^{85}Rb

Our recent work concerning a mixture of ^{85}Rb and ^{87}Rb indicates that most RF-dressed mixtures are expected to undergo fast inelastic loss [43, 140]. We begin by presenting the discussion in reference [43], which summarises inelastic loss processes

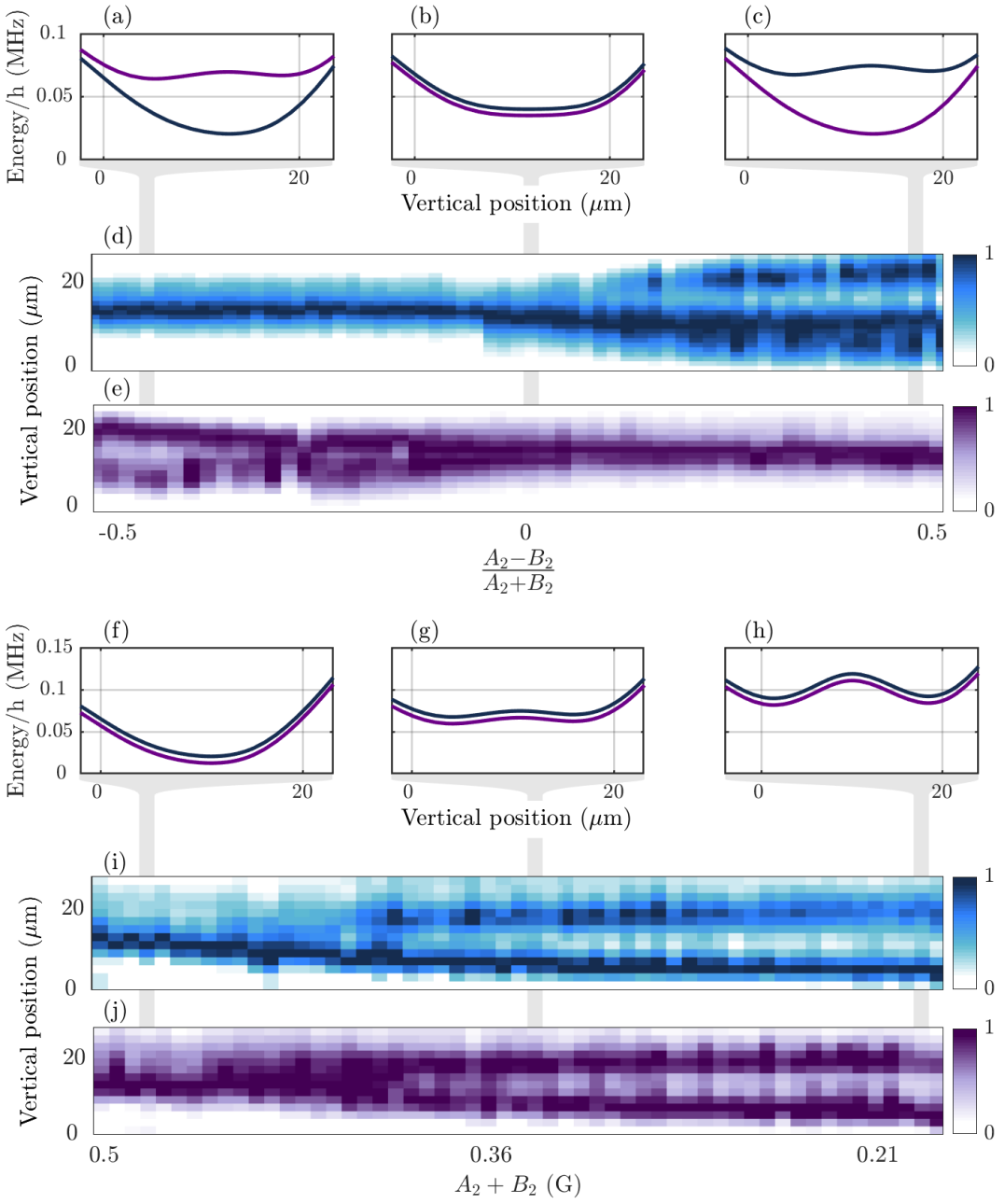

Figure 5.2: A species-selective double-well potential. (a)-(c) Potential energies for atoms with $F = 1$, $\tilde{m}_F = 1$ (blue) and $F = 2$, $\tilde{m}_F = 1$ (purple) for specific values of $(A_2 - B_2)/(A_2 + B_2)$. (d)-(e) *In situ* density distributions of atoms with $F = 1$, $\tilde{m}_F = 1$ and $F = 2$, $\tilde{m}_F = 1$ vs. $(A_2 - B_2)/(A_2 + B_2)$, respectively. The colour axes (right) indicate the relative number density. (f)-(h) Potential energies of atoms with $F = 1$, $\tilde{m}_F = 1$ (blue) and $F = 2$, $\tilde{m}_F = 1$ (purple) for specific values of $(A_2 + B_2)$, where the 2 MHz dressing RF field responsible for the barrier of the potential is linearly polarised. (i)-(j) *In situ* density distributions of atoms with $F = 1$, $\tilde{m}_F = 1$ and $F = 2$, $\tilde{m}_F = 1$ vs. $(A_2 + B_2)$ respectively. For clarity, an offset has been added to the eigenenergies of $F = 1$ in (b) and (f)-(h) to separate the $F = 1$ and $F = 2$ eigenenergies.

in a mixture of RF-dressed atoms. We consider the following mechanisms between atoms dressed with RF radiation:

- Near the avoided crossing, couplings to the RF field enable RF-induced spin-exchange collisions which can transfer atoms to lower energy collision channels;
- On the high-field side of the RF resonance, even in the absence of RF radiation, atoms can undergo RF-free spin relaxation. This process is typically slow;
- Between the avoided crossings, fast loss may occur as a consequence of RF-free spin exchange.

As the g_F factors of ^{87}Rb $F = 1$ and ^{85}Rb $F = 2$ are $-1/2$ and $-1/3$, respectively, the RF resonances occur at different magnetic field strengths. In the limit of small phase shift during the collision, spin-exchange proceeds at a rate which is roughly proportional to the difference between the singlet a_s and triplet a_t scattering lengths squared [94]. The singlet and triplet scattering lengths for ^{87}Rb+^{85}Rb collisions are $a_s = 202\ a_0$ and $a_t = 12\ a_0$, respectively, where a_0 is the Bohr radius, so spin exchange is not suppressed in the mixture and fast losses are expected at these intermediate fields. The two-body inelastic rate coefficients for collisions of RF-dressed ^{87}Rb+^{85}Rb were measured in [43] to be of order $k_2^{87,85} \sim 10^{-11}$ cm^3 s^{-1}, for fields between the RF resonances, and vary as a function of applied magnetic field strength. This finding dramatically limits the practicality of experiments concerning degenerate gases of ^{87}Rb and ^{85}Rb, where atomic number densities may approach 10^{14} cm^{-3}.

Table I of reference [43] shows a_s and a_t for different pairs of alkali metal atoms. These values demonstrate that ^{87}Rb+^{87}Rb is a special case. For most other combinations of alkali-metal isotopes, a_s and a_t are very different hence the rate coefficients for both RF-induced and RF-free spin exchange are predicted to be large. Consequently, while RF-dressed potentials are versatile methods of manipulating atomic species of

differing magnetic character, rapid inelastic loss may limit their experimental practicality.

5.4.2 A dressed mixture of ^{87}Rb atoms in different hyperfine states

For collisions of ^{87}Rb atoms, the rate coefficients for spin exchange are small, even when the process is permitted by selection rules [140]. This special property of this particular isotope has previously been credited to the similarity of the singlet ($a_s = 90.6\ a_0$) and triplet ($a_t = 99.0\ a_0$) scattering lengths, which results in similar singlet and triplet phase shifts from scattering [141]. As detailed in [43], this is a rare feature amongst combinations of alkali atoms, as most combinations have strongly differing a_s and a_t. Inelastic collisions of this mixture of RF-dressed atoms have also been investigated in the context of RF-dressed Feshbach resonances [142], however there has been no experimental study to date of the dependence of inelastic loss processes on the dressing RF field strength.

To verify the collisional stability of this mixture when RF-dressed, we have measured the loss rates of ^{87}Rb atoms with $F = 1$ and $F = 2$ when confined in an RF-dressed potential, first separately and then together.

5.4.2.1 Atoms in states with F=1 alone

Following the approach of [43, 57], for a pure cloud of atoms in the $F = 1$ state, the atom number N_1 evolves as

$$\frac{\partial N_1}{\partial t} = -\alpha N_1 - \int k_2^{1,1} n_1^2 \, \mathrm{d}V - \int k_3^{1,1,1} n_1^3 \, \mathrm{d}V \ , \tag{5.1}$$

where α is one-body rate coefficient, n_1 is the number density, and $k_2^{1,1}$ and $k_3^{1,1,1}$ are the two-body and three-body rate coefficients for of atoms with $F = 1$, respectively.

When inelastic loss is negligible, however, the terms with k_2 and k_3 in equation 5.1 can be discarded, and the atom number N_1 is observed to decay exponentially, at a rate given by α.

To measure the decay, we prepare a cloud of approximately 1.1×10^5 ^{87}Rb atoms with $F = 1$, at a temperature of 0.4 µK, in an RF-dressed potential formed by a 2 MHz RF field and a quadrupole gradient of 139.5 G cm^{-1}. For these measurements, as well as those detailed later in section 5.4.2.2, we image the gases after 15 ms of time-of-flight expansion after holding the atoms in the potential for a variable duration. Figure 5.3 a) (inset) illustrates the time-dependence of N_1 for three dressing RF amplitudes (290 mG, 570 mG and 940 mG). We observe an exponential decay of N_1 in all cases, which consequently shows that inelastic loss is negligible for our range of densities, where the maximum number density across all samples is 1.6×10^{12} cm^{-3}. Furthermore, by fitting the data with simplified versions of equation 5.1, which contain only the two-body or three-body terms, respectively, we place bounds on the rate coefficients of $k_2 < 1.6 \times 10^{-14}$ cm^3 s^{-1} and $k_3 < 7.7 \times 10^{-27}$ cm^6 s^{-1}. An imperfect vacuum in the chamber and technical noise in the apparatus are the dominant causes of the observed decay for this single species.

5.4.2.2 A mixture of atoms in the F=1 and F=2 states

We now consider a mixture of atoms in dressed states with $F = 1$, $\tilde{m}_F = 1$ and $F = 2$, $\tilde{m}_F = 1$. This choice of dressed states ensures both clouds have approximately the same gravitational sag in the potential and thus spatially overlap [65].[5] The number

[5]There exists a small difference in $|g_F|$ between these states and, consequently, there is a minor separation between the spatial locations of the potential minima [54]. In our context, however, this separation is negligible compared to the spatial extent of the trapped clouds.

of atoms with $F = 1$ in the mixture evolves as

$$\frac{\partial N_1}{\partial t} = -\alpha N_1 - \underbrace{\int k_2^{1,1} n_1^2 \, \mathrm{d}V - \int k_3^{1,1,1} n_1^3 \, \mathrm{d}V}_{\text{Negligible}} - \int k_2^{1,2} n_1 n_2 \, \mathrm{d}V - \int k_3^{1,1,2} n_1^2 n_2 \, \mathrm{d}V - \int k_3^{1,2,2} n_1 n_2^2 \, \mathrm{d}V \ . \tag{5.2}$$

where n_2 is the number density of atoms with $F = 2$, and $k_2^{i,j}$ and $k_3^{i,j,k}$ are the rate coefficients for two-body and three-body inelastic collisions of atoms in states $\{i, j, k\} \in \{1, 2\}$, where $\{1, 2\}$ represent the dressed states with $F = 1$ and $F = 2$, respectively. Measurements of $F = 1$ alone (figure 5.3 a) (inset)) have shown terms containing $k_1^{1,1}$ and $k_1^{1,1,1}$ to be negligible, which is indicated in equation 5.2.

We experimentally verify the time-dependence of N_1 in the presence of atoms with $F = 2$. To measure the inter-species rate constants, $k_2^{1,2}$, $k_3^{1,1,2}$ and $k_3^{1,2,2}$, it is sufficient to consider either loss of a small number of $F = 1$ atoms in a $F = 2$ bath, or to reverse the role of the constituents. We use the same experimental parameters as section 5.4.2.1, and the initial densities of atom clouds with $F = 1$, $\tilde{m}_F = 1$ and $F = 2$, $\tilde{m}_F = 1$ are controlled via the MW pulse duration, which determines the number of atoms N_2. MW pulse lengths of $0.15 - 40$ ms are used to vary the initial densities of atoms with $F = 1$ and $F = 2$ between $4 - 16 \times 10^{11}\mathrm{cm}^{-3}$ and $1 - 2 \times 10^{11}$ cm^{-3}, respectively.

Figure 5.3 a) & b) show N_1 and N_2 as a function of hold time, respectively, for an RF-dressed mixture. In measuring the inter-species rate constant it is sufficient to consider either loss of a small number of $F = 1$ atoms in a $F = 2$ reservoir, or to reverse these roles. As RF field strength has been predicted to modify the rate coefficient [140], we also repeat the measurements for three dressing field amplitudes, namely 290 mG, 570 mG and 940 mG. The decay is clearly exponential for all measurements: for both F and for all three field strengths. This implies that inelastic loss remains negligible for this mixture over our range of densities.

Again, by simplifying equation 5.2 to include only the terms with $k_2^{1,2}$, and either $k_2^{1,2,2}$ or $k_3^{1,1,2}$, we determine the upper bounds of $k_2^{1,2} < 2.2 \times 10^{-14}\,\mathrm{cm^3\,s^{-1}}$ and k_3 (all mechanisms) $< 1.2 \times 10^{-25}\,\mathrm{cm^6\,s^{-1}}$.

To further illustrate the lack of density dependence in the observed time-dependent dynamics, figure 5.3 c) shows the $1/e$ lifetimes for $F = 1$, which are extracted from the fitted constants $1/\alpha$, for each dressing RF field amplitude and over a range of initial n_2. Coloured boxes illustrate the $1/e$ lifetimes (and uncertainties) for the $F = 1$ population in the absence of a coexisting $F = 2$ cloud (figure 5.3 a) (inset)). A surprising feature is that the lifetime of $F = 2$ atoms vs. n_1, as shown in figure 5.3 d), rises as n_1 is increased. We speculate this is due to a temperature-dependence of the lifetime $1/\alpha$; longer microwave pulses are required to transfer more atoms from $F = 1$ to $F = 2$ and these pulses induce heating in the sample. Temperature dependence in the lifetimes of trapped gases has been observed elsewhere [143, 144], albeit observations in these case were attributed to two- and three-body effects. As we begin with $F = 1$ and transfer a fraction to $F = 2$, rate coefficients for $F = 2$ alone in the RF-dressed potential are not determined. Additionally, in figure 5.3, the lifetimes and initial densities of atoms with $F = 2$ have a larger standard error than those for $F = 1$; this occurs because the number of atoms with $F = 2$ is small compared to those with $F = 1$, even at maximum, as the imperfect MW transfer leads to atom loss and heating. We speculate this is an artefact which arises from a temperature dependence of the lifetime $1/\alpha$; longer MW pulses are required to transfer more atoms from $F = 1$ to $F = 2$ and these pulses induce heating in the sample. Additionally, lifetimes and initial densities of atoms with $F = 2$ have a larger standard error than those for $F = 1$; the number of atoms with $F = 2$ is small compared to those with $F = 1$, even at maximum, as the imperfect MW transfer leads to atom loss.

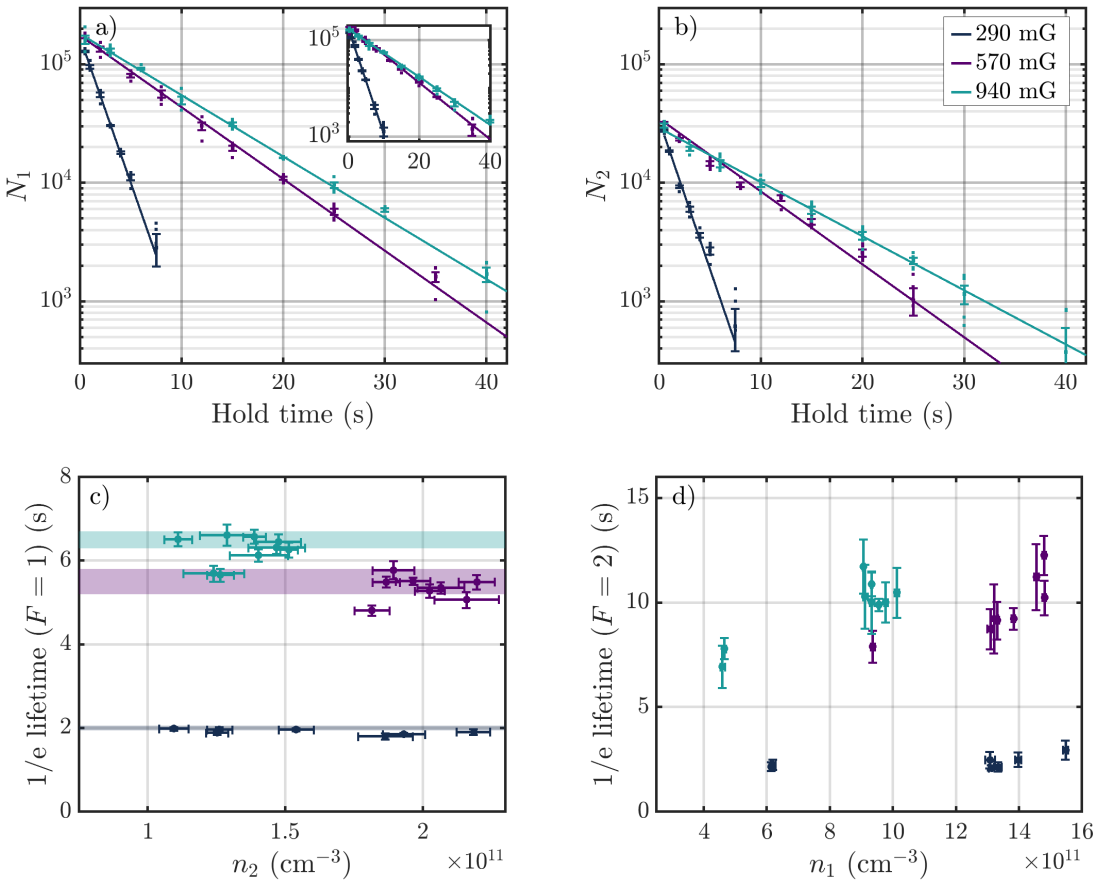

Figure 5.3: Decay of the number of atoms in states with $F = 1$, $\tilde{m}_F = 1$ and $F = 2$, $\tilde{m}_F = 1$ in an RF-dressed mixture. Results are shown for clouds held in a single-frequency, linearly polarised RF-dressed potential, for dressing RF amplitudes of 290 mG (▬), 570 mG (▬) and 940 mG (▬). a) N_1 vs. hold time for a mixture of atoms with $F = 1$ and $F = 2$, as described in section 5.4.2.2. The lines indicate fitted curves which represent exponential decay. Inset: exponential fits to N_1 vs. hold time in the absence of atoms with $F = 2$, for three dressing RF amplitudes, as discussed in section 5.4.2.1. b) N_2 vs. hold time for a mixture of atoms with $F = 1$ and $F = 2$. Individual measurements in a) & b) are illustrated by points, and vertical error bars indicate the standard error, centred about the mean, for 6 repeated measurements at each hold time. c) Measured $1/e$ lifetimes for $F = 1$ as a function of the initial number density of $F = 2$. Shaded regions represent the lifetimes of $F = 1$ atoms alone when trapped in an identical potential, which are extracted from the fitted curves in figure 5.3 a), (inset). d) Measured $1/e$ lifetimes for $F = 2$ as a function of the initial number density of $F = 1$. The vertical error bars in c) & d) correspond to the uncertainty in the fitted rate coefficient, while horizontal error bars indicate the uncertainty in the initial number density, of which some are narrower than the width of data points.

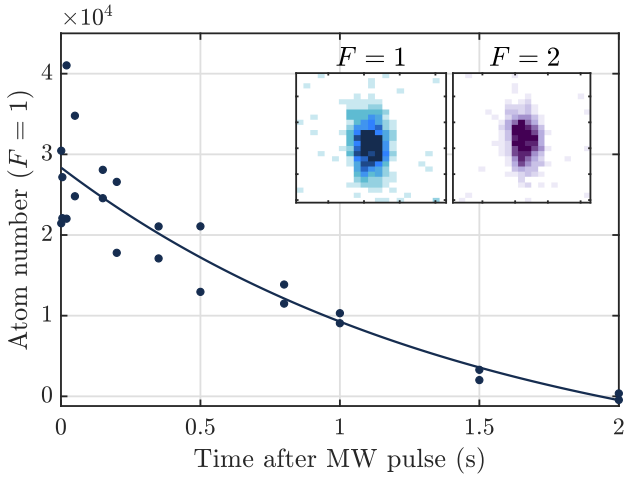

Figure 5.4: Decay of an RF-dressed degenerate mixture of ^{87}Rb atoms with $F = 1$ and $F = 2$. Atom number of ^{87}Rb atoms with $F = 1$ is shown (blue dots) with an exponential fit (blue line). Both states have number densities of the order 10^{14} cm^{-3}. Inset: *in situ* absorption images of ^{87}Rb atoms with $F = 1$ (left) and $F = 2$ (right), where the ROI is the same for both images.

5.5 Conclusion and outlook

We have experimentally realised selective manipulations of a mixture of ^{87}Rb atoms with $F = 1$ and $F = 2$ using MRF-dressed potentials. These manipulations are made possible by the distinct g_F factors of the constituents. We have demonstrated combinations of single- and double-well potentials for mixture constituents, which are realised through control of the polarisations and amplitudes of dressing RF fields. Furthermore, the scales of spatial variation can straightforwardly be tuned by the choice of dressing field frequencies and magnetic field gradient and could ultimately permit sub-µm manipulations. This approach is not affected by the diffraction limit, as is the case for optical dipole-force traps. In a wider context, the spatial dependence of resonance frequencies lies at the heart of Magnetic Resonance Imaging.

We began this investigation with caution: a previous experiment had revealed the existence of fast inelastic loss processes in an RF-dressed mixture of ^{87}Rb and ^{85}Rb, which severely limits the practicality of that particular mixture. We do not observe

inelastic loss for a mixture of ^{87}Rb atoms in RF-dressed states with $F = 1$ and $F = 2$ over the range of densities and dressing field strengths used in these experiments. The long lifetimes of RF-dressed mixtures of ^{87}Rb in different hyperfine states make this a highly promising choice for future experiments, which may involve impurity physics or studies of out-of-equilibrium dynamics. Furthermore, the lifetime remains favourable for clouds of higher atomic number density. A preliminary measurement has shown that the lifetime of a mixture of BECs in states with $F = 1$ and $F = 2$ is of order 1 s, as shown in figure 5.4, although further investigation is required to determine whether immiscibility affects the overlap of the clouds [145].

6

Two-dimensional Bose gases

In this chapter, we discuss Bose gases in the quasi-2D regime and the onset of superfluidity via the Berezinskii-Kosterlitz-Thouless (BKT) transition. We present a microscopic description of the ground state and realise a Bose gas satisfying necessary constraints for 2D dynamics in the apparatus presented in Chapter 3. We investigate the confining potential and perform a calibration of absolute atom number. Lastly, we discuss a scheme to probe the out-of-equilibrium dynamics of the gas and present preliminary results.

6.1 BKT physics in 2D Bose systems

Major developments in the field of quantum matter have permitted experiments where the effective dimensionality of the trapped gas can be reduced to one or two dimensions [24, 39, 146]. Quantum mechanics in reduced dimensions is fundamentally different: fluctuations in both the magnitude and phase of the wave function are increasingly important in the character of the ground state [146]. These fluctuations are strong enough to prevent the formation of long-range order via a global phase, which characterises the onset of Bose-Einstein condensation in 3D systems. In 2D or fewer, this effect is described by the Mermin-Wagner theorem, and consequently Bose-Einstein condensation in homogeneous systems does not occur [147]. Nevertheless, Bose-Einstein condensation in 2D harmonically-trapped gases at finite temperature is permitted, which can be proven using a similar argument to Einstein's statistical proof of condensation in 3D systems [148]. However, in the case of interactions between the atoms, as is the case in our apparatus, true long-range order is forbidden and Bose-Einstein condensation is instead replaced by the BKT superfluid transition [149–153]. BKT theory was developed as an explanation of the formation of superfluid state in a 2D bosonic system [22, 23], and has been applied to early observations of superfluidity in liquid ^{4}He films [154] and applications in the 2D ultracold gas community are of ongoing interest [24]. Many experiments to date have considered the ground state, however far less is known about the general description of out-of-equilibrium dynamics within these systems and their relaxation to equilibrium.

Initially, experiments concerning out-of-equilibrium dynamics with cold atoms have focussed extensively on one-dimensional (1D) systems [26] and recently have been extended to 3D [29,155] and 2D systems [156,157]. Investigations performed thus far have raised many open questions, including those concerning out-of-equilibrium behaviour close to a critical point [158, 159], which is particularly interesting as the

equilibrium states are expected to be described by universal scaling laws [28, 29, 32, 160–162]. We focus our investigation on 2D systems which have strong phase fluctuations, as in 1D systems, but they also exhibit a critical point associated with the BKT transition to a superfluid phase.

The results presented in this chapter are part of a broader investigation which formed the basis for an EPSRC Grant entitled *Investigating non-equilibrium physics and universality using two-dimensional quantum gases* (EP/S013105/1). Further detail regarding the experimental milestones, motivation, and theorised out-of-equilibrium behaviour is also contained in the thesis of Kathrin Luksch [62].

In this chapter, we first present the theoretical description of a Bose gas in the 2D regime, including the energy and length scales which characterise the dimensionality of the gas. We then outline an experimental sequence which realises an equilibrium Bose gas in the BKT regime. We characterise the confining potential and discuss properties of the equilibrium gas. We go on to discuss experiments to probe the out-of-equilibrium dynamics of 2D Bose gases via matter-wave interference in Chapter 7 but, first, we present an alternative scheme to realise an out-of-equilibrium distribution, as well as preliminary results.

6.2 Theory of a 2D Bose Gas

The equilibrium properties of a 2D Bose gas are defined by several distributions, including the spatial and momentum distributions, and macroscopic quantities such as chemical potential and temperature. To describe our system in these terms, we must first consider the conditions which lead to the 2D regime, and to derive expressions for relevant quantities. This derivation follows reference [37] and further information can be found in [163]. We begin by considering the Gross-Pitaevskii equation for a weakly-interacting Bose gas in a cylindrically-symmetric external trapping potential

$V_{\text{ext}}(r, z)$, where r and z are the radial and axial coordinates, respectively. For a wavefunction $\psi(r, z)$, this reads

$$\left(-\frac{\hbar^2}{2M}\nabla^2 + V_{\text{ext}}(r, z) + g|\psi(r, z)|^2\right)\psi(r, z) = \mu\ \psi(r, z)\ , \tag{6.1}$$

where g is the interaction strength and μ is the chemical potential. We identify the first term in equation 6.1 as the kinetic energy contribution, the second term as the potential energy and the final non-linear term as the mean-field energy which arises from interactions within the trapped gas. In our experimental context, we consider a harmonic trapping potential of the form $V_{\text{ext}}(r, z) = \frac{1}{2}M\omega_r^2 r^2 + \frac{1}{2}M\omega_z^2 z^2$, where ω_r and ω_z are the radial and axial trap (angular) frequencies, respectively. Exploiting the symmetries of the confining potential, we may express the wave function in a separable form whereby $\psi(r, z) = R(r)Z(z)$, where $R(r)$ and $Z(z)$ are the radial and axial distribution functions, respectively. We normalise the wave function such that $\int |Z(z)|^2\ dz = 1$ and $\int |R(r)|^2\ d^2\mathbf{r} = N_0$, where N_0 is the temperature-dependent atom number of the condensed fraction.

To achieve 2D confinement, we must effectively remove one spatial degree of freedom[1]. Removing a degree of freedom, in this context, requires the axial component of the wave function to be the ground state of the confining potential and occupation of excited states to be energetically prohibited. All relevant energy scales must thus be less than the harmonic oscillator spacing in the axial direction, such that $\mu, k_B T, \hbar\omega_r \ll \hbar\omega_z$, which implies that the gas must be significantly more tightly confined in the axial direction than the radial direction ($\omega_z \gg \omega_r$). In practice, $\mu, \hbar\omega_r < \hbar\omega_z$ and $k_B T \sim \hbar\omega_z$ are sufficient for 2D dynamics [163].

When $\mu < \hbar\omega_z$, the mean-field contribution to axial dynamics can be ignored and

[1]For a cylindrical potential, symmetry requires we must remove the axial (z) degree of freedom.

$Z(z)$ is a solution of the time-independent Schrödinger equation:

$$\left(-\frac{\hbar^2}{2M}\frac{\partial^2}{\partial z^2}+\frac{1}{2}M\omega_z^2 z^2\right)Z(z)=EZ(z)\ . \tag{6.2}$$

We note that the eigenstates of equation 6.2 are those of a quantum harmonic oscillator. For $\mu, k_BT \ll \hbar\omega_z$, the occupation of excited axial states is effectively frozen out, both via thermal excitations and excitations driven by interactions, and so the axial wave function component is the lowest energy harmonic oscillator eigenstate. For an ultracold gas, we may also assume the kinetic energy in the gas a result of motion in the radial plane is negligible compared to the interaction and potential energies; this assumption is an application of the Thomas-Fermi approximation [163]. With $Z(z)$ as the lowest energy eigenstate of the axial potential, we may average equation 6.1 over the axial direction to derive the radial density distribution and the Thomas-Fermi radius

$$n(r)=|R(r)|^2=\frac{\mu_{2\mathrm{D}}}{\tilde{g}}\left(1-\frac{r^2}{R_{\mathrm{TF}}^2}\right) \quad , \quad R_{\mathrm{TF}}=\sqrt{\frac{2\mu_{2\mathrm{D}}}{M\omega_r^2}}\ , \tag{6.3}$$

respectively, where we have defined the 2D chemical potential $\mu_{2\mathrm{D}}=\mu-\hbar\omega_z/2$. The reduced interaction strength $\tilde{g}=g\sqrt{M\omega_z/2\pi\hbar}$ arises as a consequence of averaging equation 6.1 over the axial direction. Inserting the interaction strength due to s-wave collisions $g=4\pi\hbar^2 a/M$, we thus find an expression for the interaction strength and chemical potential of the gas in the 2D regime:

$$\tilde{g}=\frac{\sqrt{8\pi}a}{a_z}\ ;\ \mu_{2\mathrm{D}}=2\hbar\omega_r\left(\frac{aN_0}{a_z\sqrt{2\pi}}\right)^{1/2}, \tag{6.4}$$

where $a_z=\sqrt{\hbar/M\omega_z}$ is the axial harmonic oscillator length. This discussion determines the energy scales $\mu_{2\mathrm{D}}$, $\hbar\omega_z$ and k_BT which define the dimensionality of the gas with respect to the experimental parameters. We now consider the onset of the superfluid transition in the 2D regime.

6.2.1 The BKT transition in dilute gases

In low-temperature 2D Bose gases, density fluctuations are frozen out and phase fluctuations or quantised vortices are the dominant contribution to the dynamics. A quantised vortex is a phase singularity, where the phase winding about its core is an integer multiple of 2π per full revolution. The BKT phase transition is characterised by the binding of quantised vortices of opposite phase windings about their cores [163], which occurs below a critical point, and leads to the onset of a superfluid fraction; while the system is not described by a global phase, as is the case for Bose-Einstein condensation in 3D, the onset of bound vortices describes quasi-long-range order in the system. The binding of quantised vortices has been observed directly [164] and via the atomic distributions in matter-wave interference experiments [24].

The occurence of superfluidity is characterised by a universal jump in the superfluid PSD $\mathcal{D}_s$ from 0 to 4, where $\mathcal{D}_s = n_s\lambda^2$ for superfluid density n_s and de Broglie wavelength λ [165]. This condition is based on the superfluid density, and thus the location of the critical point is to be determined from macroscopic properties of the trapped ensemble, including the total PSD $\mathcal{D} = n_{2\mathrm{D}}\lambda^2$, where n_{2D} is the trap-averaged density. For $\tilde{g} \ll 1$, numerical simulations have shown at the critical point

$$\mathcal{D}^{\mathrm{BKT}} \approx \ln\left(380/\tilde{g}\right) \;\; ; \;\; \left(\frac{\mu}{k_B T}\right)^{\mathrm{BKT}} \approx \frac{\tilde{g}}{\pi}\ln\left(13.2/\tilde{g}\right) \;\; , \tag{6.5}$$

where the superscript 'BKT' indicates the critical value [158].

The onset of superfluidity also has important consequences for the correlations within the gas. We consider the first-order correlation function $g_1(\mathbf{r}, \mathbf{r}') = \langle\psi^\dagger(\mathbf{r})\psi(\mathbf{r}')\rangle$. In a 2D superfluid, g_1 decays algebraically at long distance $r = |\mathbf{r} - \mathbf{r}'|$, such that $g_1(r) \propto r^{-\alpha}$. The exponent α is related to the PSD of the superfluid by $\mathcal{D}_s = 1/\alpha$ [150]. For a thermal gas, as is discussed later, g_1 decays exponentially, thus the nature of the fluid can be determined via the functional form of g_1. Armed with this

array of conditions for 2D dynamics and a prediction for the critical point, we present a realisation of the BKT state in our apparatus.

6.3 Experiments on 2D Bose gases

The goal of the experimental sequence is to produce a 2D atomic gas in the RF-dressed trap which satisfies the constraints defined above, namely: $k_B T \ll \hbar\omega_z$, $\mu_{2D} \ll \hbar\omega_z$, and $\omega_r \ll \omega_z$, as well as the required conditions for superfluidity. We begin with a typical BEC sequence, where atoms are first evaporatively cooled in the magnetic quadrupole and TOP traps to around 0.6 µK, as described in Chapter 3. Further evaporative cooling is performed in the TAAP trap produced by a circularly-polarised dressing field of frequency 2 MHz and Rabi frequency 200 kHz, with a quadrupole magnetic field of gradient 188 G cm^{-1}. Evaporative cooling is again performed to reduce the temperature to approximately 70 nK which results in a BEC of 2×10^5 atoms. The amplitude of the rotating bias field is then ramped down to zero to produce a harmonic trap with frequencies $\omega_z = 2\pi \times 650$ Hz and $\omega_r = 2\pi \times 25$ Hz in an RF-dressed trap.

With these trap frequencies, the trapped cloud is still in the 3D regime. To compress the gas further, we ramp down the amplitude of the dressing field so that it corresponds to a Rabi frequency of 38 kHz. To avoid the excitation of centre-of-mass motion, we counteract the change in gravitational sag arising from the ramp in dressing field amplitude by ramping the magnetic quadrupole gradient to 195 G cm^{-1}. This ramp is performed over approximately 50 ms. This sequence produces a gas of 1.2×10^4 atoms in a harmonic confining potential with theoretically-predicted trap frequencies of $\omega_z = 2\pi \times 1.5$ kHz and $\omega_r = 2\pi \times 27$ Hz. These predicted trap frequencies satisfy $\omega_r \ll \omega_z$ and are similar to those presented in other realisations of 2D Bose gases [37]. We therefore expect the confined gas to exhibit 2D behaviour, subject to

satisfying the remaining constraints. We now turn our attention to the requirement that $\mu_{2D} \ll \hbar\omega_z$.

6.3.1 An absolute calibration of atom number

The 2D chemical potential is directly related to the atom number in the gas, which in turn defines the critical PSD for the BKT transition. In the absence of a direct observation of the binding of vortices or unmistakeable superfluid phenomena, an absolute calibration of atom number is required to establish whether we are in the BKT regime. It is not necessary to perform this calibration for a 2D cloud specifically, hence we utilise the known relationships between T, N, the condensed number N_0 and the critical temperature T_c for Bose-Einstein condensation in 3D. For a harmonically trapped gas in the 3D regime, we expect

$$\frac{N_0}{N} = 1 - \left(\frac{T}{T_c}\right)^3 \quad , \tag{6.6}$$

where T_c is the critical temperature for condensation [94]. For an ideal, non-interacting gas, the critical temperature is given by $T_c^{\text{ideal}} \approx 0.94\hbar\bar{\omega}N^{1/3}/k_B$, where $\bar{\omega}$ is the geometric mean of the trap frequencies. In our system, inter-particle interactions shift T_c from the ideal gas value. Using expressions presented in reference [166], we expect $T_c \approx T_c^{\text{ideal}}\left(1 - 1.33N^{1/6}a/a_z\right)$.

We vary the final RF knife frequency during a stage of evaporative cooling in the TOP trap, which consequently varies N and T. The choice of the TOP is also motivated by technical limitations which prevent a large dynamic range of temperatures in our other trap architectures. Trap frequencies in the TOP trap have been measured in previous calibrations to be 60.5 Hz (radial) and 149 Hz (axial). We extract the temperature using a Gaussian fit to the thermal wings of the distribution after TOF expansion and extract N_0/N using a bimodal fit, as illustrated by figure 6.1 (lower)

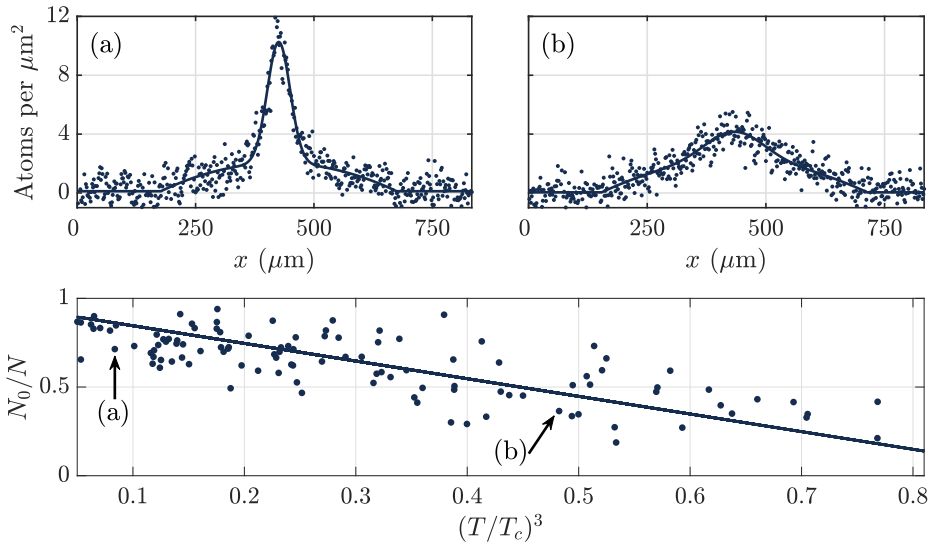

Figure 6.1: An exact calibration of atom number via the onset of Bose-Einstein condensation in the TOP trap. a)-b): density distributions and bimodal fits to points marked by arrows in the plot below. Lower: N_0/N vs. $(T/T_c)^3$, where we measure N/N_0 and T from a bimodal fit after TOF expansion.

for two temperatures.

Figure 6.1 (upper) illustrates N_0/N vs. $(T/T_c)^3$ and a linear fit to the data. Noting equation 6.6, we fix the gradient and intercept of the fit to be -1 and 1, respectively, and the only free parameter is a constant scale factor which multiplies all atom numbers. We maximise the R^2 correlation coefficient of the fit and find the optimal scale factor to be 1.09(0.04). We attribute the variance of the data to shot-to-shot variation when imaging the gases, as well as the nature of the bimodal fit which is used to extract N_0 and N: the bimodal model has 7 free parameters and can consequently overfit to intrinsic noise in the density profiles.

The extraction of atom number using the method presented in chapter 3 relies on a known detuning of the imaging light, as well as its intensity. It is very possible that these experimental parameters have drifted since their last calibration and is therefore the most likely cause of the fitted scale factor not equal to unity. Nevertheless, our measurement confirms that our determination of atom number is sufficiently precise, with possible inaccuracies on the order of 10%, which would not strongly

affect our conclusions. We now experimentally verify the characteristics of the highly-anisotropic confining potential and the trapped gas.

6.3.2 Characterising the potential and the trapped gas

We return to the highly-anisotropic RF-dressed potential described in section 6.3 to measure the trap frequencies and to determine the nature of the trapped gas. To extract the trap frequencies, we use the same method as presented in Chapter 2 section 2.3, where a vertical kick is applied to the trapped gas by a sudden jump in quadrupole current. The centre-of-mass position is illustrated in figure 6.2, for both axial (upper) and radial (lower) oscillations, from which we extract trap frequencies of 1.36(0.02) kHz and 27(1) Hz, respectively. This serves as confirmation that $\omega_r \ll \omega_z$, thus we now verify the remaining conditions for 2D dynamics, specifically $\mu_{2\mathrm{D}} \ll \hbar\omega_z$ and $k_B T \ll \hbar\omega_z$, are also satisfied. In this potential, we calculate

$$\tilde{g} = \frac{\sqrt{8\pi}a}{a_z} = 0.087 \ , \tag{6.7}$$

where $\tilde{g} \ll 1$ defines a weakly-interacting gas. From a bimodal fit to the density distribution along x after TOF expansion, as illustrated in figure 6.3 (left, lower), we extract a superfluid fraction of 0.7(0.1) for a gas of approximately 1.2×10^4 atoms. Consequently, we find $\mu_{2\mathrm{D}}/\hbar\omega_z = 0.32 < 1$. From the same fit, we measure the temperature of the gas to be 52(2) nK and thus $k_B T/\hbar\omega_z = 0.80$. At this temperature, we calculate the fraction of atoms occupying the ground state is $g_2(1)/\sum_{j=0}^{\infty} g_2(e^{-jk_B T/\hbar\omega_z}) = 0.80$, where $g_2(z)$ is the second-order polylogarithm function[2]. It is therefore a reasonable assumption to ignore the influence of excited axial states on the ground state [167].

For a trapped system, the onset of the BKT transition arises when the peak density in the system surpasses the critical value, in analogy to the onset of Bose-

[2]This expression applies for an ideal gas, where $\mu = 0$, and thus is an approximation for our system.

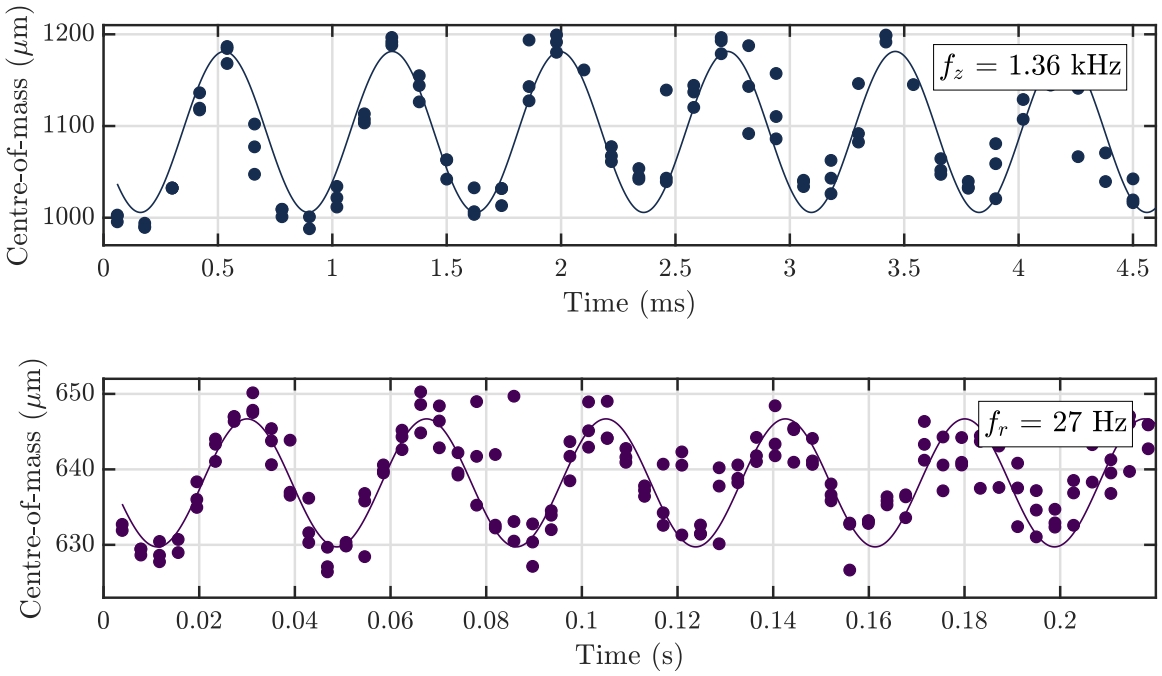

Figure 6.2: Measurement of the axial (upper) and radial (lower) trap frequencies in the highly-anisotropic RF-dressed potential defined by a Rabi frequency of 38 kHz and a quadrupole gradient of 195 G cm^{-1}. We measure the trap frequencies to be 1.36(0.02) kHz (axial) and 27(1) Hz (radial).

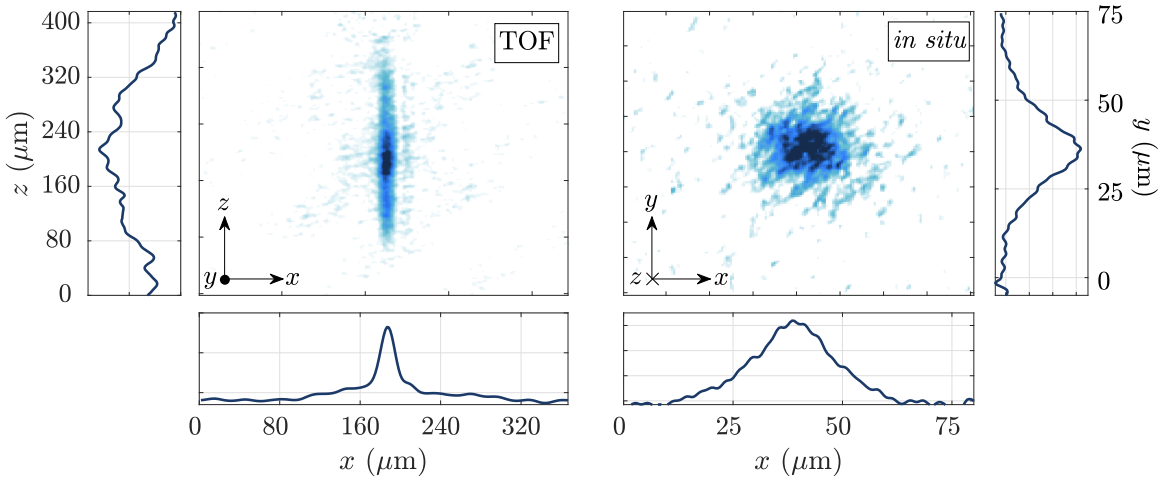

Figure 6.3: Absorption images of a 2D Bose gas. Left: absorption image following 20 ms of TOF using the horizontal imaging axis. Right: *in situ* absorption image using the vertical imaging axis. The integrated density profiles along both axes are shown.

Einstein condensation in trapped gases. For $\tilde{g} = 0.087$, the critical phase-space density required for the BKT transition is

$$\mathcal{D}_{\mathrm{BKT}} = \log\left(\frac{380}{\tilde{g}}\right) = 8.4 \ . \tag{6.8}$$

For experimental parameters defined above, we calculate a peak PSD of $\mathcal{D} = 250$ and a trap average of $\mathcal{D} = 72 > \mathcal{D}_{\mathrm{BKT}}$. We thus expect a significant superfluid fraction, which is consistent with the bimodal profiles of both the TOF and *in situ* distributions (see figure 6.3).

Having satisfied all of the necessary conditions, we are confident that we have realised a BKT phase in our apparatus. Further study is required to prove this definitively, via measurement of unmistakeably superfluid phenomena, such as scissors mode oscillations [168, 169] or the direct observation of vortex pairing [164].

6.4 Out-of-equilibrium dynamics

In Chapter 7, we present a method of investigating the out-of-equilibrium dynamics of 2D Bose gases using matter-wave interference. Before discussing this method and corresponding experimental results, we consider an alternative means of creating an out-of-equilibrium distribution in a 2D system. We also discuss techniques to observe the subsequent time evolution of the position and momentum distributions as the system equilibrates, and present preliminary results.

In general, to ensure dynamics remain largely 2D, we should make a perturbation to the radial spatial or momentum distributions, but avoid significant excitation in the axial direction. This can be achieved by exploiting the energy level structure of the RF-dressed trap. We first consider a typical RF spectroscopy scheme, where an RF probe excites a transition between the trapped $F = 1$, $m_F = 1$ state to an untrapped state, such as those with $m_F = 0$ [34, 58]. The probe RF field is

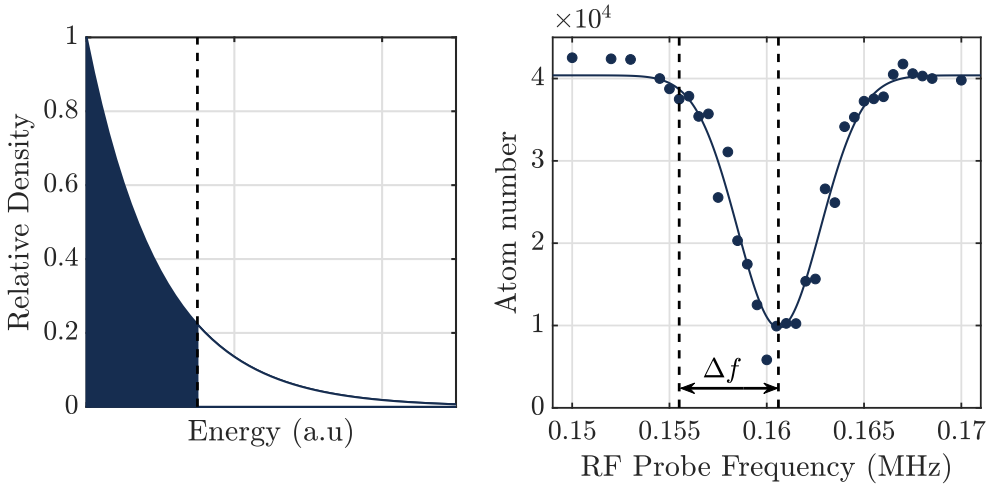

Figure 6.4: RF spectroscopy in the shell trap. Left: cartoon of the role of an off-resonant pulse. The distribution of atoms vs potential energy is truncated by the application of a probe, which excites atoms to untrapped states. Right: RF spectroscopy using a weak probe. The frequency of the probe relative to the resonance Δf is varied in successive experimental sequences and the atom number measured. The rightmost dotted line indicates the RF resonance.

resonant when it matches the energy separation between the potential minimum, where the atoms are trapped, and the untrapped $m_F = 0$ state; this corresponds to the point of largest atom loss as the frequency of the probe is varied. The characteristic lineshape of the RF spectogram, as shown in figure 6.4 (right), arises as the chemical potential, or indeed thermal energy of the gas, broadens the distribution of potential energies [57, 63].

Figure 6.5 (left) shows a cutaway of the potential energy surfaces in the shell trap. For atoms at the trap minimum at $x = 0$, an axial displacement Δz increases their potential energy and consequently a higher RF frequency is required to excite the transition to $m_F = 0$. This is illustrated in figure 6.5 (top right). As atoms move azimuthally around the shell, the vectorial coupling between the atom and the RF field is weakened and Rabi frequency is reduced. Consequently, the energy separation between $m_F = 1$ and $m_F = 0$ states is less than at resonance and the probe RF frequency required to excite the transition to $m_F = 0$ is lower. This is illustrated in figure 6.5 (bottom right), where the colours correspond to the paths in figure 6.5 (left).

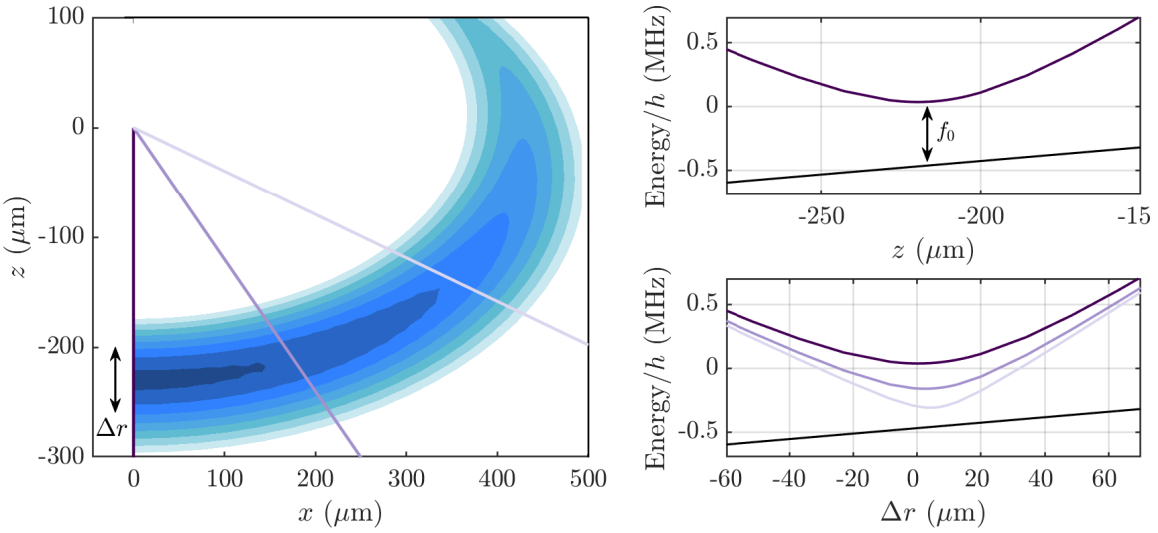

Figure 6.5: Left: a cutaway of the potential energy surfaces of the RF-dressed trap for the $F = 1$, $\tilde{m}_F = 1$ dressed state, in the $x - z$ plane. Lower potential energies are indicated by darker colours. Δr is defined as the displacement along the paths indicated and the potential energies along the corresponding coloured line are illustrated in the lower right panel. The upper right panel shows the potential energy as a function of z for the dark purple path and the black line indicates the potential energy of the $\tilde{m}_F = 0$ eigenstate. f_0 indicates the resonant RF probe frequency for atoms trapped at this position.

To summarise, at the trap minimum, RF probe frequencies which are higher than the spectrogram resonance frequency cut away in the axial direction, as the energy separation between trapped and untrapped states grows with displacement from the trip minimum along z. Whereas for an RF probe with a frequency lower than resonance of the RF spectrogram, atoms which are ejected are those which are displaced from the trap minimum in an azimuthal direction. Applying an RF probe which is lower in energy than the resonance of the spectrogram thus acts to cut into the atomic distribution radially.

We thus propose a experiment where a 'cut' is made by applying a short, strong pulse of RF radiation at a frequency Δf detuned from the RF spectroscopy resonance. The pulse is short if $t_{\text{pulse}} \ll 2\pi/\omega_r$, such that the atoms can be assumed to be immobile during the pulse, and is strong such that a significant (>20%) fraction of atoms are ejected. The trapped gas is consequently put out of equilibrium and the subsequent dynamics, in both position and momentum space, can be investigated as the cloud relaxes.

We can readily extract the position distribution $n(r)$ of the gas via an analysis of the density distribution for an *in situ* cloud. To extract the momentum distribution $n(k)$, we follow the methods of reference [170, 171], where the potential is suddenly relaxed and the interacting gas expands for a quarter of a period ($T/4$) in the relaxed trap before an image is taken. We realise this by performing a sudden, non-adiabatic change of the dressing RF amplitude, from a Rabi frequency of 38 kHz to 300 kHz, thus changing the predicted trap frequencies to 530 Hz (axial) and 6 Hz (radial). The sudden change in confinement excites a monopole mode in the trapped gas, as illustrated by the *in situ* absorption images shown in figure 6.6 (upper). The angular frequency of the breathing mode ω_B is predicted to be approximately $2\omega_r$ [172]. An extensive treatment of the monopole mode dynamics incorporates shifts to the oscillation frequency due to quantum anomalies [173,174], as well as those arising from

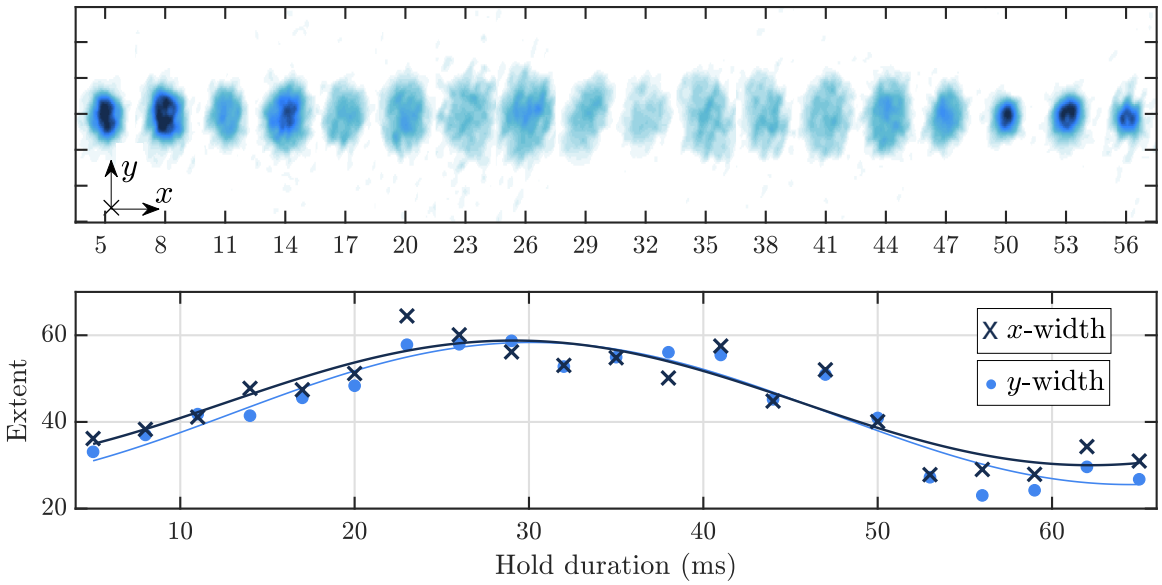

Figure 6.6: In-plane expansion in the relaxed trap. Upper: *in situ* absorption images taken using the vertical imaging system following expansion in the relaxed potential. Images correspond to hold durations of 5 ms - 56 ms, in 3 ms intervals. Lower: spatial widths of the cloud along the x (crosses) and y (dots) axes, extracted using a Thomas-Fermi fit to the density distribution. The solid lines indicate sinusoidal fits to the data points from which we extract breathing mode frequencies of 14.2(1.5) Hz (x) and 13.5(2.3) Hz (y).

the presence of the third dimension in an imperfect, quasi-2D system [175] In this context, however, we are only concerned with the apparent oscillation frequency and hence $T/4$ expansion duration as a means of determining the momentum distribution, rather than the relationship between the oscillation frequency and other experimental parameters. We extract the cloud widths along the x and y axes using a parabolic Thomas-Fermi fit and determine $T/4$ from the observed oscillations (as shown in figure 6.6 (lower)).

Absorption images taken *in situ* or after $T/4$ expansion in the relaxed trap are analysed further to determine $n(r)$ and $n(k)$. For all r, we extract the fraction of atoms located in an annulus of radius r and width dr from the centre of mass, which determines $n(r)$, as illustrated in figure 6.7. The same analysis is applied to clouds after $T/4$ expansion to determine $n(k)$. The distributions are normalised, such that

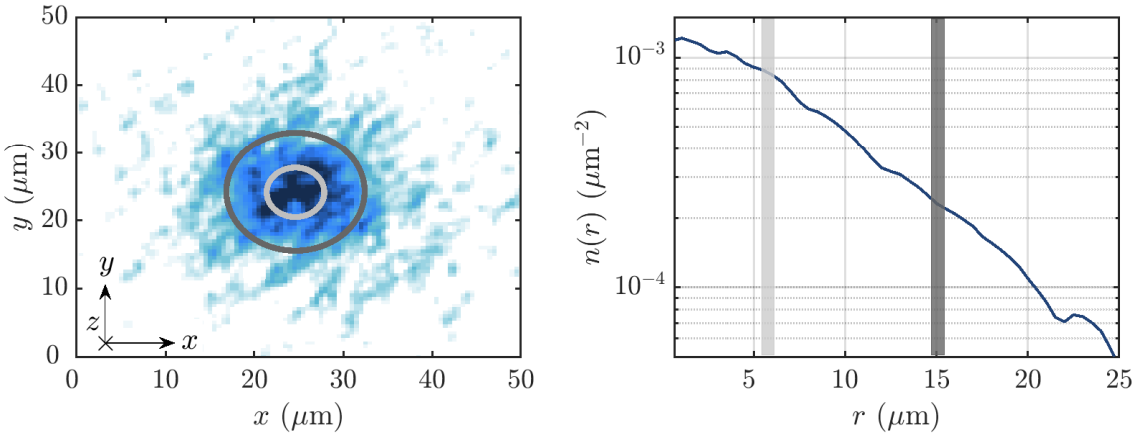

Figure 6.7: Analysing the atomic distribution. Left: *in situ* absorption image using the vertical imaging system. Light grey and dark grey annuli indicate regions at radii of 6 µm and 15 µm from the centre of mass, respectively. Right: normalised radial density distribution, where the dark grey and light grey strips correspond to annuli shown in the leftmost figure.

they integrate over all r or k to unity.

We have now established a method of perturbing the cloud and extracting the position and momentum distributions. We briefly discuss our qualitative expectations for the time evolution of these distributions following the RF pulse.

For a pulse close to the RF resonance, for instance $\Delta f = -1\,\mathrm{kHz}$, the atoms that are ejected come predominantly from the superfluid component, as $\mu_{2\mathrm{D}}/h \sim 1\,\mathrm{kHz}$. This dramatically reduces the superfluid density and may place the BKT phase in a superheated state; this consequently may drive the system to equilibrate to a normal fluid. A more detuned pulse, for example $\Delta f = -4\,\mathrm{kHz}$, will eject mostly thermal atoms, as $\mu_{2\mathrm{D}}/h \ll 4\,\mathrm{kHz}$. The ejection of these atoms takes away thermal energy, thus cooling the gas, and hence we expect the superfluid component to remain.

Given the motivations discussed in section 6.1, the proposed experiments mentioned above are interesting as they provide insight into the relaxation of the gas when its superfluid density is suddenly quenched, which may drive the system to cross the BKT transition dynamically. We now present our preliminary results from

performing this type of measurement.

6.4.1 Results

We apply a 1 ms pulse $\Delta f = -1$ kHz detuned from the RF resonance to the 2D gas described above. We calculate a Fourier width for the pulse of $0.36\,\text{kHz} < \mu_{2\text{D}}/h$, as the pulse has a square amplitude profile as a function of time[3]. It is therefore reasonable to expect the pulse forms a local reduction in the superfluid density, as the pulse is much shorter than the timescales of radial atomic motion, as $2\pi/\omega_r \sim 40\,\text{ms}$. We hold the gas in the trap and then take an *in situ* absorption image or an image after $T/4$ evolution in the relaxed trap. We analyse the position $n(r)$ and momentum distribution $n(k)$ as a function of time after the out-of-equilibrium pulse, as shown in figure 6.8 (upper panels). The experiment is repeated for an RF pulse with $\Delta f = -4$ kHz detuning, where the results are illustrated in figure 6.8 (lower panels).

Comprehensive analysis of the data is still in progress, however, the preliminary results agree with some of our expectations. For the $\Delta f = -1$ kHz pulse, we see the distributions progressively broaden in both position and momentum space. This is consistent with the hypothesis that the pulse removes a significant fraction of atoms from the superfluid state, perhaps such that $\mathcal{D} < \mathcal{D}^{\text{BKT}}$ and the system consequently relaxes to a thermal state. However, in the momentum distribution following the $\Delta f = -4$ kHz pulse, we see the superfluid component is preserved, although the distribution does broaden slightly in time. This may arise because of monopole excitation of the trapped gas following the RF pulse, or the proposed cooling dynamics may be outweighed by residual heating of the trapped gas due to other mechanisms. We see little effect on the position distribution following the pulse which is not unphysical; the superfluid component appears as a less sharp feature in the bimodal *in situ* den-

[3]This is calculated from approximating the width of the pulse in Fourier space as the separation between the first-order zeros of the sinc function.

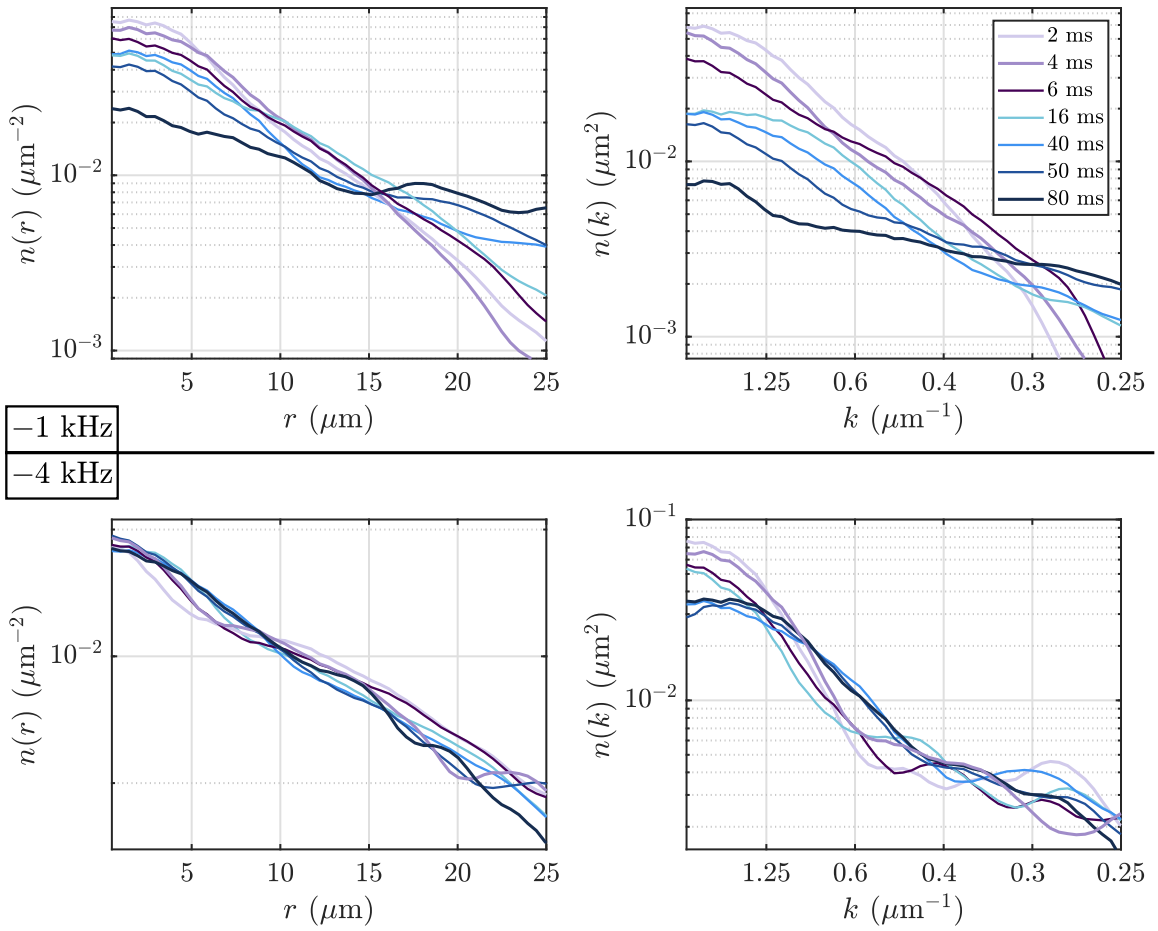

Figure 6.8: Preliminary results of probing out-of-equilibrium dynamics in a 2D Bose gas. Upper panels: $n(r)$ and $n(k)$ following a -1 kHz detuned RF pulse, as extracted from *in situ* imaging or $T/4$ expansion in a relaxed trap, respectively. Lower panels: $n(r)$ and $n(k)$ following a -4 kHz detuned RF pulse, as extracted from *in situ* imaging or $T/4$ expansion in a relaxed trap, respectively. Colours denote hold times following the pulse, as indicated by the legend (top right). All distributions are normalised such that the area contained is unity.

sity distribution than in the distribution after TOF (see, for instance, figure 6.3). Our conclusions remain qualitative, in the absence of additional data, however this method shows promise, and will be valuable as a corroborating measurement for experiments discussed in Chapter 7. Time constraints and required upgrades to the experimental hardware prevented the acquisition of additional data; it will also be necessary to make further measurements of the time evolution of a gas in the absence of an RF pulse, to quantify the effects of heating and other disturbances which may occlude the out-of-equilibrium dynamics.

6.5 Outlook

We have determined experimental parameters that produce a 2D Bose gas in this apparatus. We have characterised the confining potential for the gas and performed a calibration of absolute atom number. Furthermore, using expressions derived and tested elsewhere, we satisfy necessary criteria to realise a BKT phase, which we observe as a superfluid fraction in the density distribution of the gas.

Following work to produce a 2D gas in our apparatus, we discussed a method to produce an out-of-equilibrium distribution, which would allow us to investigate the relaxation dynamics and fulfil motivations discussed in section 6.1. To realise an out-of-equilibrium distribution, we exploited the energy level structure of the RF-dressed trap in combination with RF spectroscopy techniques. Imaging of the distribution of atoms in position and momentum space was achieved using *in situ* imaging of the gas along the vertical axis and expansion following a sudden relaxation of confinement, respectively. As such, our results rely heavily on the fidelity of the vertical imaging system. While this imaging system was sufficiently focussed for much of the work presented in this chapter, further improvement is necessary to observe the binding of vortices or to identify the functional form of g_1; the momentum distribution $n(k)$ is

related to g_1 via the Fourier relationship

$$g_1(\mathbf{r}) = \int d^2k \; e^{i\mathbf{k}\cdot\mathbf{r}} n(k) \; . \tag{6.9}$$

However, as was noted in reference [176], the measured $n(k)$ is the convolution of the momentum distribution with the finite resolution of imaging. Misfocusing in the vertical imaging system acts to further broadening of the apparent momentum distribution for small k, thus leading to a steeper decay of g_1 which may occlude the expected transtion from algebraic to exponential decay as the system traverses the BKT critical point.

Finally, the preliminary out-of-equilibrium dynamics in both the position and momentum distributions following RF pulses display qualitatively distinct behaviour. We see the superfluid fraction is retained for pulses which remove mostly thermal atoms, whereas the distribution broadens towards a thermal distribution when a significant amount of the superfluid fraction is ejected. The resolution of the imaging system is insufficient to resolve sharp features in the momentum distribution from the out-of-equilibrium pulse or to identify theoretically-proposed timescales for the relaxation dynamics [177,178]. Consequently, improving the resolution of the vertical imaging system will be necessary to enable further study using this scheme. While significant improvements were achieved by replacing an older camera with a newer, higher sensitivity camera (see Chapter 3), the system suffers from many technical issues, such as dust accrual on relatively inaccessible optics. Despite this limitation, the out-of-equilibrium distribution is produced using a simple method and, in this sense, may be a more stable environment to investigate the relaxation dynamics of the gas than methods discussed in Chapter 7.

When time permits the acquisition of further data, a study of the time evolution of an unperturbed gas is necessary as a control sample with which to compare out-

of-equilibrium dynamics, as discussed earlier. Furthermore, by tailoring evaporative cooling parameters prior to the final experimental stages which produce the 2D gas, it may be possible to freely tune the atom number and temperature, such that the gas can be brought close to the BKT critical point prior to the RF pulse. This is an especially interesting direction as, close to the critical point, the dynamics of the system are expected to scale with a universal set of exponents [179–181]. Universal dynamics have been observed elsewhere in the evolution of system parameters; for instance, the time-dependent behaviour of the structure factor and dimensionless quantities following a quench were found to scale with universal exponents in references [29] and [33], respectively.

7

Matter-wave interferometry

This chapter presents experiments on the matter-wave interferometry of Bose gases released from double-well potentials. Many of these results are presented in [44] and represent significant improvement over the preliminary results of interference described in reference [57]. We begin by demonstrating matter-wave interference of 3D Bose gases originally confined in double-well potentials, and verify the expected scaling of the fringe wavelength with the TOF and spatial separation between the wells. We demonstrate the onset of coherence as the final barrier height is reduced. Using a different combination of RF fields, we present a quasi-2D double-well potential and demonstrate the versatility of the potentials to load a specified fraction of atoms into each well. Finally, we discuss proposed experiments to probe dynamical phase transitions and the time evolution of the phase distribution.

7.1 Introduction and motivation

The experiments detailed within this chapter are the basis for an extended programme of investigation towards understanding the out-of-equilibrium dynamics of 2D quantum systems. Similarly to Chapter 6, further motivation, as well as the experimental work plan for matter-wave interference experiments, is described in the EPSRC Grant entitled *Investigating non-equilibrium physics and universality using two-dimensional quantum gases* (EP/S013105/1) and in the thesis of Kathrin Luksch [62]. Our study has been inspired by experiments concerning 1D systems, as well as theoretical works [20, 41, 182]. In those 1D experiments, interferometry was performed by splitting a 1D quasi-BEC into two 1D quantum gases which were out of equilibrium. These experiments have elucidated the effects of strong phase fluctuations present in 1D systems, as well as the nature of prethermalisation [20, 25], and the time scales of relaxation [25]. Subsequent experiments have investigated quantum tunnelling between the two trapped gases [183–187].

In 2D, as discussed in Chapter 6, there exists a superfluid phase transition characterised by the onset of quasi-long-range order (the BKT transition). Theoretical works have proposed that out-of-equilibrium dynamics close to the critical point can be probed through the time evolution of a 2D Bose gas after it is split into two parallel components [188]; this is analogous to the 1D experiments discussed earlier [20, 182]. Splitting the 'parent' cloud into two 'daughter' clouds constitutes a non-adiabatic change (quench) of the density which can leave the daughter clouds in a 'superheated' state, where their PSD is below the critical value for superfluidity. The gases will subsequently cross the BKT phase transition dynamically, from superfluid to normal fluid, in an analogy to the reverse of the Kibble-Zurek mechanism which describes the onset of structure in many contexts [178, 189–191]. The dynamics of a homogeneous 2D quasi-BEC following a quench, including the onset of coherence

and the formation of topological defects which obeyed a Kibble-Zurek scaling, were observed in reference [156].

An advantage of our protocol is that splitting the gas gives us access to the relative phase between the two daughter BECs, as explored in detail in 1D experiments. Measurement via absorption imaging of a single system prevents direct observation of the phase of the wave function of a quantum-mechanical object. This is not a major limitation for 3D BECs, as these systems are characterised by a global phase. In reduced dimensional systems (1D and 2D), however, fluctuations play a defining role in the nature and dynamics of the trapped gas, which is manifested in the density and phase distributions. Thus an experiment which aims to fully consider the out-of-equilibrium dynamics of such systems, or to investigate the role of fluctuations, is ill-equipped to do so without access to the phase.

This chapter is structured as follows: in 7.3, we discuss the analysis methods applied to the matter-wave interference pattern of BECs released from a double-well potential. In 7.4, we verify the expected nature of the interference fringes as we change TOF and the spatial separation between the trapping wells. In 7.5, we analyse the coherence of the splitting procedure. In 7.6, we reduce the spatial separation of the wells and increase the strength of confinement, which reduces the effective dimensionality of the BECs. In 7.7, we tune our potential to imbalance the population of atoms in each well which influences the contrast of the interference pattern. In 7.8, we briefly discuss a method of tomographic imaging which has been recently implemented on the experiment to improve the contrast of matter-wave interference patterns [192], as well as subsequent experimental schemes to investigate the out-of-equilibrium dynamics following a quench.

7.2 Experimental methods

A BEC of $1 - 2 \times 10^5$ atoms of ^{87}Rb in the $F = 1$ level is loaded into an RF dressed potential formed by a single RF component. The RF amplitudes used in the double-well sequence vary across the different experimental contexts presented in this chapter. We begin by presenting the realisation of a double well with primary RF of frequency 1.8 MHz and amplitude 325 mG, with a quadrupole gradient of 165 G cm^{-1}. This RF field, referred to as the primary RF component, defines the uppermost well in the double-well potential. The primary component, as well as all other RF fields described within this chapter, is linearly-polarised along $\hat{\mathbf{e}}_x$. An additional RF field at 2.0 MHz is applied with amplitude 143 mG; this RF field is referred to as the 'barrier' RF component. The amplitudes of the 2.0 MHz field and an additional (secondary) RF field at 2.2 MHz are steadily ramped up to 465 mG and 440 mG, respectively, over 100 ms to form a broad single well into which the trapped atoms redistribute. The amplitude of the 2.0 MHz field is then ramped down over 100 ms, causing the barrier to increase in energy, to form a double-well potential, where the primary and secondary RF fields define the trapping wells.

The separation between the potential minima is strongly dependent on the magnetic quadrupole field gradient, as well as the separation in frequency between the three RF components [34, 57, 58, 61, 62]. Finer control of the separation between the two wells is implemented via the amplitude of the central field, as shown in figure 7.1 (left). The double-well potential A (blue) is formed with a barrier RF amplitude of 314 mG and B (purple) with 185 mG, to realise spatial separations between the minima of the potential wells of 7.1 µm and 12.9 µm, respectively. Similarly, the well can be 'tilted' by adjusting the amplitudes of the primary and secondary RF fields, and can be tuned to deliberately imbalance the relative population of atoms in each well, as we discuss later [34].

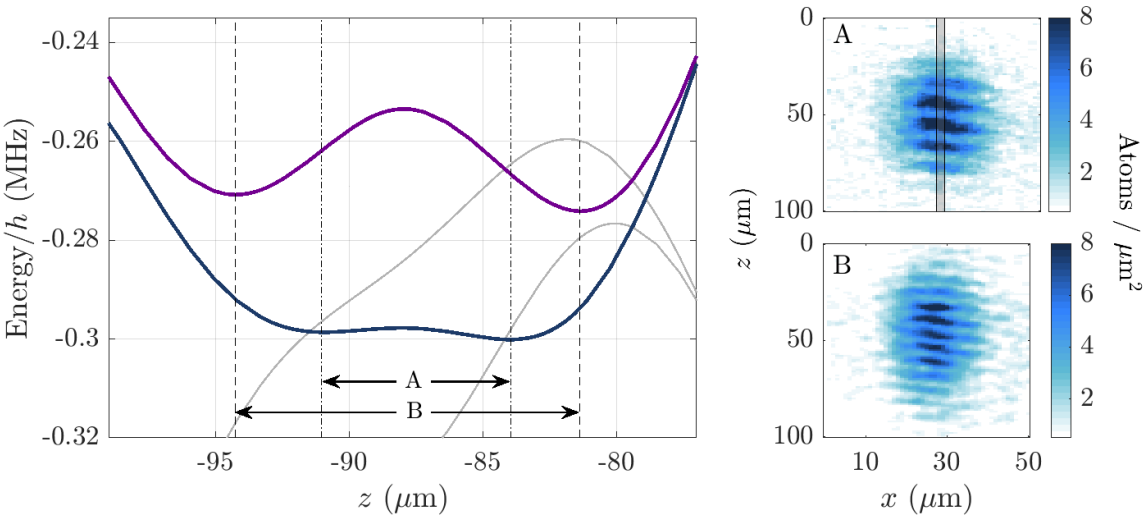

Figure 7.1: Left: MRF-dressed eigenenergies for atoms dressed with RF components at 1.8 MHz, 2.0 MHz and 2.2 MHz, where the 1.8 MHz and 2.2 MHz fields have amplitudes 325 mG and 440 mG, respectively. The 2.0 MHz RF field amplitude can be controlled to raise or lower the central barrier and to modify the spatial separation between the wells. Barrier amplitudes of 314 mG and 185 mG realise well separations of 7.1 µm and 12.9 µm for the $\tilde{m}_F = 1$ states labelled A (blue) and B (purple), respectively. Dashed-dotted and dashed lines mark positions of the potential minima for the configurations corresponding to A and B, respectively, and light grey lines indicate the energy of states with $\tilde{m}_F = -1$. States with $\tilde{m}_F = 0$ are not shown. Right: absorption images of the matter-wave interference patterns produced by BECs initially confined in the potentials A and B after 25 ms of TOF. The grey box in A indicates the strip of pixels used in further analysis of the fringe wavelength and phase, as discussed in section 7.3.

To observe interference, we release the clouds by turning off the dressing RF field while leaving the quadrupole field on, such that the atoms in each well are projected into m_F states [57,62]. The $m_F = 0$ components from each trapped gas are unaffected by the magnetic field and overlap as they fall in TOF. An interference pattern is observed in the density distribution as a consequence of the superposition of the two matter-waves of the separate degenerate gases. This experimental protocol realises repeatable matter-wave interference, and is a significant improvement on preliminary results of interference obtained in reference [57]. The dependence on spatial separation between the wells, an analogue to the slit spacing in an optical diffraction experiment, is apparent in the absorption images A and B in figure 7.1, which show the density distribution of atoms after release from potentials marked A and B, respectively.

7.2.1 Fundamental frequencies

To ensure the potential is static, there must exist a common fundamental frequency between the dressing RF components. For three, or more, RF components, the relative phase between the fields modifies the potential, as shown in references [34, 62]. In a practical context, the available range of frequencies is discretised according to the bit-depth of the programming register of the DDS chips. For the AD9910 DDS chips, the output frequency is discretised by a 32-bit frequency tuning word (FTW), where the output frequency is given by

$$f_{\mathrm{Out}} = f_{\mathrm{SysClock}} \times \frac{\mathrm{FTW}}{2^{32}}, \tag{7.1}$$

where f_{SysClock} is the on-chip clock frequency, which we choose to be 400 MHz. This equation is inverted to calculate a FTW given a user-specified output frequency, such that

$$\mathrm{FTW} = \mathrm{round}\left(2^{32} \times \frac{f_{\mathrm{Out}}}{f_{\mathrm{SysClock}}}\right) , \tag{7.2}$$

where the 'round' indicates rounding to the nearest integer. This discretisation means that requesting an output frequency of 1.8 MHz actually produces an output frequency of 1.800 000 02 MHz. Consequently, when three or more RF components are required, the FTWs may not have a large common factor, which defines the fundamental frequency, due to rounding or discretisation. If the true fundamental frequency is comparable to the trap frequencies, this may lead to a time-dependent modulation of the potential and induce heating or atom loss.

This modulation can be avoided by choosing a common fundamental which is exactly divisible into the programming register. As an example, we choose a common fundamental described by a FTW of 2147484 (decimal) or 10000011000100100111 00 (binary, most significant bit first), which realises a separation of $\Delta f = 0.200\,000\,033$ MHz. and the frequencies of the RF components are subsequently defined as $\{9, 10, 11\} \times \Delta f = 1.800\,000\,295$ MHz, 2.000 000 328 MHz and 2.200 000 361 MHz. The importance of setting the frequencies in this way was first appreciated around November 2019. In previous work, this issue may have been obscured by other sources of noise and heating.

Later, we introduce a double-well potential with approximately 2.5 µm spatial separation. In this case, we choose a FTW of 536870 (decimal) or 10000011000100100110 (binary, most significant bit first) which defines a common fundamental frequency of $\Delta f = 0.049\,999\,915$ MHz. The frequencies of the RF components are $\{39, 40, 41\} \times \Delta f = 1.949\,996\,687$ MHz, 1.999 996 603 MHz and 2.049 996 518 MHz.

7.3 Analysis methods

We now consider the interference pattern produced by free-falling, overlapping BECs initially confined in a double-well potential. BECs in three-dimensions can be characterised by a global phase, with a wave function of the form $\psi(\mathbf{r}, t) \sim \sqrt{n(\mathbf{r}, t)}\exp(i\theta(t))$,

where $\mathbf{r}$ is the position and t is the time since the beginning of free expansion (TOF). The combined wave function can be expressed $\psi(r,t) = \sqrt{N_1}\ \psi_1(\mathbf{r},t) + \sqrt{N_2}\ \psi_2(\mathbf{r},t)$, where $\psi_{1,2}(\mathbf{r},t)$ and $N_{1,2}$ refer to the two BEC wave functions and their expected atom numbers, respectively. As the clouds are released from the double-well potentials, they overlap and interfere. The resulting density distribution is given by

$$\begin{aligned} n(\mathbf{r},t) = |\psi(\mathbf{r},t)|^2 &= |\sqrt{N_1}\ \psi_1(\mathbf{r},t) + \sqrt{N_2}\ \psi_2(\mathbf{r},t)|^2 \\ &= N_1|\psi_1(\mathbf{r},t)|^2 + N_2|\psi_2(\mathbf{r},t)|^2 + \underbrace{2\sqrt{N_1 N_2}\ \mathrm{Re}[\psi_1(\mathbf{r},t)\ \psi_2^*(\mathbf{r},t)]}_{\text{Interference term}}, \end{aligned} \tag{7.3}$$

where Re denotes the real part. We follow the discussion in [94], where inter-particle interactions are neglected and the free-falling clouds are modelled as Gaussian distributions of a well-defined phase. The interference term thus varies as

$$\mathrm{Re}[\psi_1(\mathbf{r},t)\ \psi_2^*(\mathbf{r},t)] \propto \exp(-r^2/R_t^2)\ \cos\left(\frac{\hbar}{M}\frac{\mathbf{r}\cdot\mathbf{d}}{R_0^2 R_t^2}t + \phi_1 - \phi_2\right) \tag{7.4}$$

where r is the radial coordinate, R_0 is the initial spatial extent of each cloud, R_t is the width of the wave packets at time t as given by $R_t^2 = R_0^2 + (\hbar t/MR_0)^2$, $\phi_{1,2}$ are the phases of the two condensates and $\mathbf{d} \parallel \hat{\mathbf{e}}_z$ is their initial spatial separation. The assumption that the clouds can be modelled as Gaussian wave packets does not fully capture the experimental context, even when interactions are neglected: each daughter cloud is a BEC at finite temperature, and thus the density distribution after TOF will be bimodal [193]. Furthermore, the incoherent thermal component appears as a background distribution that reduces the contrast of the fringes [194]. Nevertheless, equation 7.4 is sufficient to characterise the experiments detailed within this thesis.

For times such that $t \gg 1/f_z$, where f_z is the axial trap frequency, the gases

expand to much greater than their initial extent; in this limit, $R_t \approx \hbar t/MR_0$. Consequently, the distributions originating from each well, described by $N_{1,2}|\psi_{1,2}(\mathbf{r},t)|^2$, cannot be distinguished from one another. The density distribution is thus described as a function of position z by

$$n(z,t) = g(z,t)\left(1 + A(t)\,\cos\left(\frac{2\pi z}{\lambda(t)} + \phi\right)\right) \ , \tag{7.5}$$

where $g(z,t)$, in the limit of no interactions, is a Gaussian envelope function, $A(t)$ is the contrast of the fringes, and $\phi = \phi_1 - \phi_2$ is the phase difference between the condensates. $\lambda(t)$ is the fringe wavelength (the distance between successive maxima), which is given by

$$\lambda(t) = \frac{ht}{Md} \ , \tag{7.6}$$

where $d = |\mathbf{d}|$. Both clouds are assumed to have the same trapping conditions and initial spatial extent, as characterised by the oscillation frequencies for atoms within each potential well. In our system, these trap frequencies in the two wells are not equal because the amplitudes of RF fields which realise the trapping wells must necessarily differ to counteract the difference in gravitational potential energy. For a barrier RF amplitude of 314 mG and the experimental parameters described earlier, a numerical simulation predicts a well separation of 7.1 µm, with axial trap frequencies of approximately 730 Hz (primary well) and 640 Hz (secondary well). Throughout experiments described in this chapter, the relative difference in trap frequencies remains $< 15\%$.

Given a 2D atom number distribution across pixels extracted from an absorption image, we find $n(z,t)$ by taking the central 'strip' of pixels, which is located at the centre-of-mass position x_{CoM} along $\hat{\mathbf{e}}_x$; this is illustrated in figure 7.1 (A). Several analysis methods are used in the following sections: we extract the fringe wavelength λ, contrast A and phase ϕ using a fit model of the form of equation 7.5. The fringe coherence is evaluated by extracting the relative phase difference between

the maximum of the Gaussian envelope and the fringes, and comparing this phase difference over many experimental cycles. This accounts for shot-to-shot variation in the centre-of-mass position of the cloud.

In section 7.6, we examine matter-wave interference of quasi-2D Bose gases. In the quasi-2D regime, axial motion is frozen out, and atoms occupy the lowest harmonic oscillator eigenstate in this axial potential. Consequently, expansion along $\hat{\mathbf{e}}_z$ is characterised by the expansion of a Gaussian wave packet, and thus is applicable to the discussion presented above [150]. However, in contrast to 3D BECs, 2D systems in the BKT regime are not characterised by a global phase, and phase and density fluctuations are present at any non-zero temperature. We discuss the role of these fluctuations and their influence on the contrast of the matter-wave interference pattern in section 7.5.

A limitation of our scheme is that we necessarily integrate along the imaging direction $\hat{\mathbf{e}}_y$. Integration along the imaging axis reduces the contrast, as the column density includes incoherent thermal atoms. Furthermore, in the presence of phase fluctuations, the contrast will decay as a function of integration length. These limitations prevented further analysis of phase correlations in earlier experiments [24].

7.4 Interferometry of three-dimensional BECs

We begin by investigating the matter-wave interference pattern after TOF. The qualitative behaviour of the fringes is as expected: fringes form perpendicular to the initial displacement, as shown in figure 7.1. We verify the expected nature of the matter-wave interference pattern as a function of TOF and well separation d, as described by equation 7.6, using approximately 3×10^4 atoms in each well. We vary the TOF and extract the wavelength of fringes using the analysis presented in section 7.3. Figure 7.2 (a) illustrates the linear relationship between TOF duration and the fitted λ,

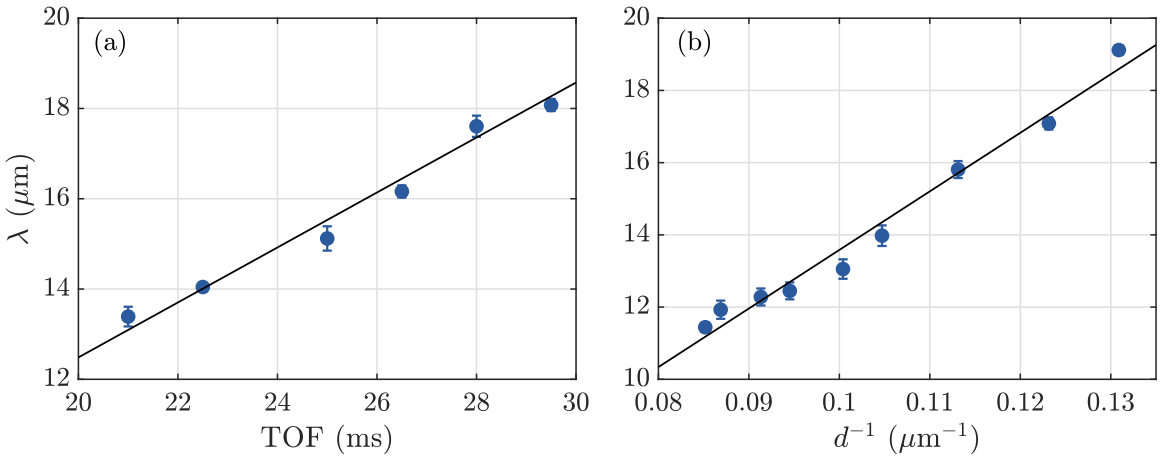

Figure 7.2: Wavelength of matter-wave interference fringes as a function of TOF and well separation. (a) The TOF is varied between 21 ms-29.5 ms. (b) The well separation d is varied via control of the barrier RF field amplitude for a constant TOF of 25 ms. d is calculated using a numerical simulation of the double-well potential for each barrier RF amplitude.

as expected. From the gradient of the fitted curve, we extract the well separation as 7.4(0.4) µm, which is consistent with the numerical simulation which predicts a separation of 7.1 µm.

We now investigate the relationship between d and λ, where we expect $\lambda \propto 1/d$ according to equation 7.6. We use a fixed TOF of 25 ms and vary the well separation via the amplitude of the 2 MHz field which forms the barrier of the double-well potential. We vary the barrier amplitude between 220-360 mG, which corresponds to a range of predicted well separations from 11.6-7.0 µm. Figure 7.2 (b) illustrates the fringe wavelength as a function of inverse well separation, which shows the expected linear relationship between λ and d^{-1}. The range over which d is varied is constrained by the range of barrier amplitudes, and similarly the range of TOF is limited by the field-of-view of the imaging system. Nevertheless, we observe the expected behaviour of λ, however, further investigation is required to claim the experimental procedure is coherent.

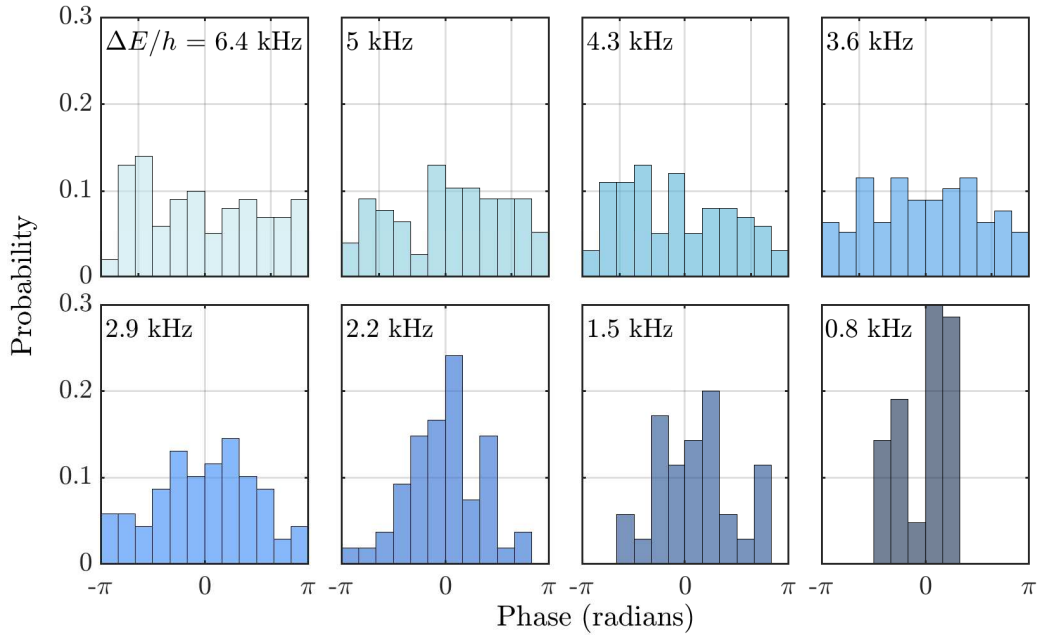

Figure 7.3: Distribution of the phase across matter-wave interference patterns. We vary the barrier RF amplitude and consequently the separation in energy ΔE between the minimum of the primary well and the peak of the barrier. This is indicated in the top left of each panel. We hold the BECs for 50 ms before imaging the distribution after 21 ms of TOF.

7.5 Coherent splitting

For experiments outlined in section 7.1, the splitting procedure must be coherent, as defined by a repeatable relative phase between the daughter clouds following the split. To evaluate the coherence, we follow the method presented in reference [41], where the fringe phase is measured across many separate experimental cycles to construct a distribution of phases. Furthermore, we repeat the series of measurements for a range of the barrier heights, where the peak of the barrier is between $\Delta E/h = 800$ Hz to 6.4 kHz above the potential energy of the primary well. We hold the clouds in the double-well potential for 50 ms before release and take an image after 21 ms of TOF.

Figure 7.3 illustrates the distribution of phases across 30 experimental runs as a function of barrier height, which shows a progressive peaking of the distribution for lower barrier heights. We have verified the distribution for faster (50 ms) and

slower (200 ms) splitting procedures. We hypothesise that the observed behaviour is due to the imperfect amplitude stability of the RF fields or, perhaps less likely, as a consequence of phase-locking via tunnel coupling or a residual fraction of atoms which are sufficiently energetic to traverse the barrier. We now explain the possible origin of each of these scenarios and the mechanisms which lead to the onset of coherence.

The potential energy of the wells E determines the rate of phase winding for the trapped gases, via the familiar functional form $\exp(-iEt/\hbar)$. The potential energies for the wells are controlled via the amplitudes of the RF dressing fields, as discussed in Chapter 2. For a very high barrier, where ΔE is large, the potential energy of the primary well is strongly decoupled from the amplitude of the secondary RF field, and vice versa. Consequently, fluctuations in the amplitudes of the primary or secondary RF fields imprint onto the phase of the trapped gas in their respective wells, but have little influence on the other well. Amplitude fluctuations thus lead to a randomised relative phase between the gases, producing a uniform distribution of matter-wave interference fringe phases across experimental cycles; this is consistent with our observations. However, for a close-to-flat double-well potential, where ΔE is small, the wells are not decoupled and fluctuations in the amplitude of any of the RF fields affects the potential energy of both wells. Amplitude fluctuations are shared as 'common-mode' noise which do not influence the relative phase between the gases and subsequently the phase of the matter-wave interference fringes.

If the onset of coherence occurs as a result of tunnel coupling, which is a phenomenon observed elsewhere [41, 184], this suggests that tunnelling dynamics may be directly observable, via oscillations in the *in situ* number distribution or the phase of the matter-wave interference pattern as a function of hold time. This investigation is the subject of ongoing work, but is currently limited by the repeatability of loading similar numbers of atoms into each well: fluctuations in the RF amplitudes affect the relative potential energies of the wells, both at the point of loading from the broad

single well into the double well and during the subsequent time evolution. While RF amplitude variation across many experimental cycles has been measured to be <1% via spectroscopic measurements, greater stabilities of order <0.1% are required for investigations of tunnelling dynamics: the chemical potential of trapped gases is ∼1 kHz, thus fluctuations in Rabi frequency and hence the relative potential energies of the wells must be much smaller. Numerical estimates of amplitude stability requirements over a range of tunnelling rates are given in reference [57]. Improvements to RF amplitude stability will be realised by the incorporation of an active feedback circuit, which will be detailed in the thesis of David Garrick. Nevertheless, the currently obtained RF amplitude stability is sufficient for stable trapping in low RF amplitude potentials, where quasi-2D confinement may be realised.

7.6 Two-dimensional potential wells

The strength of confinement, described by the trap frequencies, can be increased by reducing the amplitude of the dressing RF fields and increasing the quadrupole field gradient [37], as discussed in Chapters 2 and 6. We apply linearly-polarised RF fields at approximately 1.95 MHz, 2 MHz and 2.05 MHz (see section 7.2.1) with amplitudes 97 mG, 57 mG and 120 mG, respectively, and use a magnetic field gradient of 165 G cm^{-1}.

Numerical methods outlined earlier predict a well separation of 2.2 µm and trap frequencies of 1.35 kHz (primary) and 1.21 kHz (secondary). The trap frequencies have since been verified via experimental measurements of the trap frequencies. This well separation is verified by variation of the TOF to be 2.1(0.1) µm, as shown in figure 7.4 (left); we also vary the well separation via the barrier RF amplitude (figure 7.4 (right)). We verify that this splitting procedure is coherent, via the phase of the interference pattern across several experimental cycles, and observe a peak

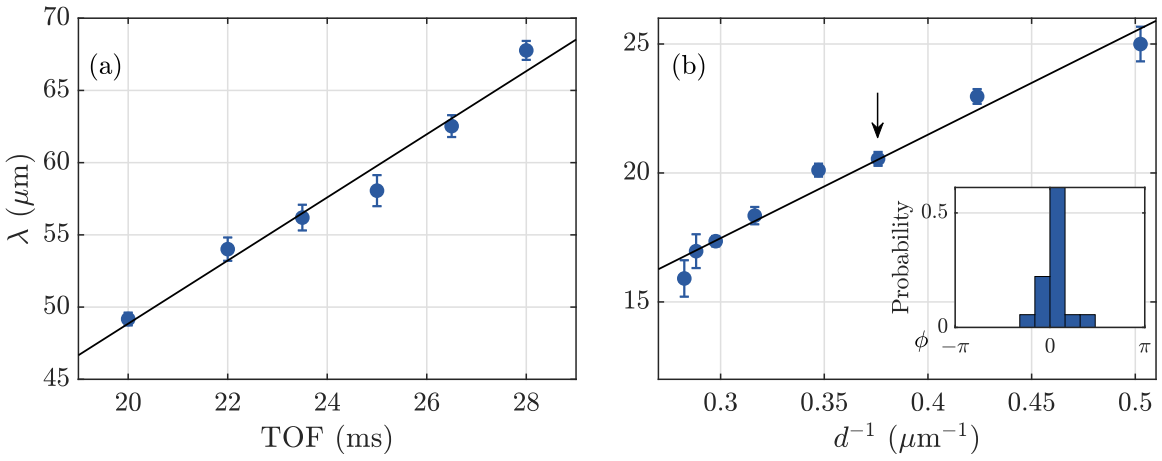

Figure 7.4: Wavelength of matter-wave interference fringes of 2D clouds as a function of TOF (a) and inverse well separation (b). Inset: the phase distribution across 20 experimental sequences with well separation indicated by the arrow.

distribution which is illustrated in figure 7.4 (right, inset).

The experimental realisation of a 2D double-well potential, where the splitting procedure is coherent, is a critical step towards investigations of the out-of-equilibrium dynamics of 2D systems. The coherence ensures the relative phase between the gases following the quench is repeatable, which is necessary to examine the evolution of the relative phase during subsequent time evolution. First, we consider the correlations in the matter-wave interference pattern and examine differences between the 3D and 2D cases.

7.6.1 Phase correlations

We outline the method proposed by Polkovnikov *et al.* [180], where off-diagonal correlations functions can be extracted from analysis of the contrast of the matter-wave interference pattern. As discussed earlier, in the presence of phase fluctuations, the integrated matter-wave interference pattern over a length L_x will decay with the integration length. The stronger the fluctuations, the faster the integrated contrast will decay. We define an average integrated contrast over several experimental cycles

$$A^2\left(S\right) \approx \frac{1}{S^2}\left\langle \left| \int_S \psi_1(\mathbf{r})\psi_2^*(\mathbf{r})d^2r \right| \right\rangle \ , \tag{7.7}$$

where S is the integration area defined by the integration length along the imaging direction L_y and the length L_x along $\hat{\mathbf{e}}_x$, as illustrated in figure 7.5 (left). In the absence of tunnelling between the two potential wells, $\psi_1(\mathbf{r})$ and $\psi_2(\mathbf{r})$ are statistically independent. We also assume $\psi_1(\mathbf{r})$ and $\psi_2(\mathbf{r})$ are those of a uniform density system. Similarly, the integration length L_y is constant, as we integrate over the full atomic distribution. Given these assumptions, equation 7.7 simplifies to

$$A^2\left(L_x\right) \approx \frac{1}{L_x}\int_0^{L_x} dx\ \left|g_1\left(x\right)\right|^2 \tag{7.8}$$

where $g_1(x)$ is the first-order correlation function and $x = |\mathbf{r} - \mathbf{r}'|$ for points $\mathbf{r}, \mathbf{r}'$ along the x axis. This treatment can be extended to include higher moments of the distribution to extract higher-order correlation functions. The first-order correlation function, however, is sufficient to qualitatively discriminate between the superfluid and normal states. In the normal state, $g_1(x)$ is rapidly exponentially decaying, and so $A^2(L_x) \propto L_x^{-1}$. In the superfluid state, $g_1(x)$ decays slowly with an algebraic functional form: $g_1(x) \propto x^{-\alpha}$, where $\alpha = 1/\mathcal{D}_s$ and $\mathcal{D}_s$ the superfluid PSD, thus $A^2(L_x) \propto L_x^{-2\alpha}$ [24].

Figure 7.5 (right) illustrates the squared contrast as a function of integration length L_x for the matter-wave interference interference of Bose gases in the 3D regime (blue) and 2D regime (purple). Exponential fits of squared contrast of the form $A^2(L_x) \propto L_x^{-1}$ (solid) and algebraic fits of the form $\langle A^2(L_x)\rangle \propto L_x^{-2\alpha}$ (dashed) are presented for both cases.

The root mean squared error (RMSE) of the fits for the 3D cloud are 0.0051 (algebraic) and 0.0014 (exponential). We thus find the decay of $A^2(L_x)$ in the 3D case to be more strongly described by exponential decay. Although we expect long-

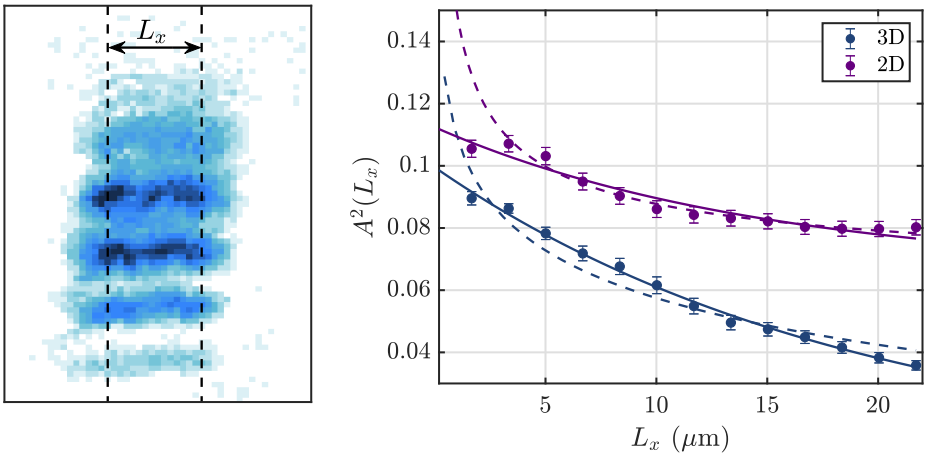

Figure 7.5: Decay of matter-wave interference contrast as a function of integration length. Left: matter-wave interference pattern of gases in the 2D regime, where the integration length L_x is indicated by the arrows. The image is first rotated such that the integration occurs parallel to the mean direction of the fringes. Right: squared contrast $A^2(L_x)$ as a function of integration length L_x, for gases in the 3D regime (blue) and 2D regime (purple). Data points are fitted with an exponential decay (solid) and algebraic function (dashed).

range order in this system, we attribute the decay of contrast to the contribution of the incoherent thermal component as the integration length is increased.

In the 2D case, we find the RMSE of the fits to be 0.0017 (algebraic) and 0.0027 (exponential). This suggests the functional form of $A^2(L_x)$ is better described by algebraic decay, which is consistent with the presence of a condensed component as discussed earlier, although additional data acquisition and analysis is required to affirm these conclusions. From the algebraic fit, we find the exponent $\alpha = 0.24(0.09)$. The onset of superfluidity is characterised by a universal jump in $\mathcal{D}_s$ from 0 to 4 [165], thus the exponent $\alpha = 0.25$ is expected at the point of the phase transition [195]. This may suggest our system is close to the BKT critical point, which is possible, as the gas may suffer from heating and atom loss during the splitting procedure. However, integration along L_y reduces the peak contrast, both via the contribution of the coexisting thermal component and integration over phase fluctuations which may be present in the clouds. Furthermore, this is not a uniform system, and thus decay

of the contrast is also driven by the reduction in superfluid density further from the centre of the clouds [194]. Residual excitation in the axial dimension may also affect the scaling of the contrast, as it has been shown to affect other coherent properties of the 2D gas, including modes of oscillation [175].

The qualitative verification of matter-wave interference for 2D Bose gases, via the coherence of the protocol and expected phase correlations, fulfils several experimental aims defined earlier. The coherence of the process permits further investigation of time dynamics, as the initial state is well defined. However, future experiments, such as tunnelling or out-of-equilibrium dynamics experiments, also require repeatable and tunable occupation of the wells. We now discuss the capabilities of the MRF-dressed potentials to tune the occupation of the wells during the splitting procedure.

7.7 Tunable centre of mass position

The double-well potential can be tilted via control of the relative amplitudes of the dressing fields which form the primary and secondary wells [34]. As a consequence, atoms can be loaded preferentially into either of the two wells. Figure 7.6 (a) illustrates absorption images of the *in situ* density distribution of atoms as a function of secondary dressing RF amplitude. This figure clearly indicates the preferential loading of atoms into the secondary well when the potential energy is lower than the primary well, and vice versa. Prior to imaging, the atom clouds were forced apart by raising the barrier suddenly. This is necessary to resolve the population in each well, as the scale of separation is comparable to the resolution of our imaging apparatus, and blurring remains apparent even with this procedure. As discussed earlier, RF amplitude fluctuations cause the number of atoms loaded into each well to vary across many experimental cycles, which prevents the direct observation of tunnelling dynamics with the current apparatus. However, for the experiments detailed below,

it is sufficient to consider the average occupations across many experimental realisations.

Figure 7.6 (b)-(c) illustrate the centre-of-mass position of the BECs as a function of secondary RF amplitude, where the barrier height is comparable to the chemical potential of the BECs (b) and 5 times greater (c). The centre-of-mass positions are fitted with a sigmoidal function. The plots show the distribution of atoms is able to spread almost evenly across the flat well in (b), whereas the high barrier in (c) prevents most of the atoms from occupying the region between the wells and causes a sharper jump in the centre of mass.

We now consider the matter-wave interference patterns which are produced after TOF expansion. Maximal contrast is expected to be achieved by having a balanced distribution of atoms across the two wells, which is deduced by differentiation of equation 7.4[1]. The model presented earlier does not account for finite-T systems, and we expect the thermal component of each trapped gas will act to reduce the maximum constrast below that of a $T = 0$ gas. Nevertheless, assuming equal thermal fractions and trap parameters, the maximum contrast is achieved by an equal number of atoms in each well, and imbalancing the populations should result in a lower interference contrast A.

[1]We note that if the number in each well is exactly $N/2$, the relative phase uncertainty diverges, as described in reference [196].

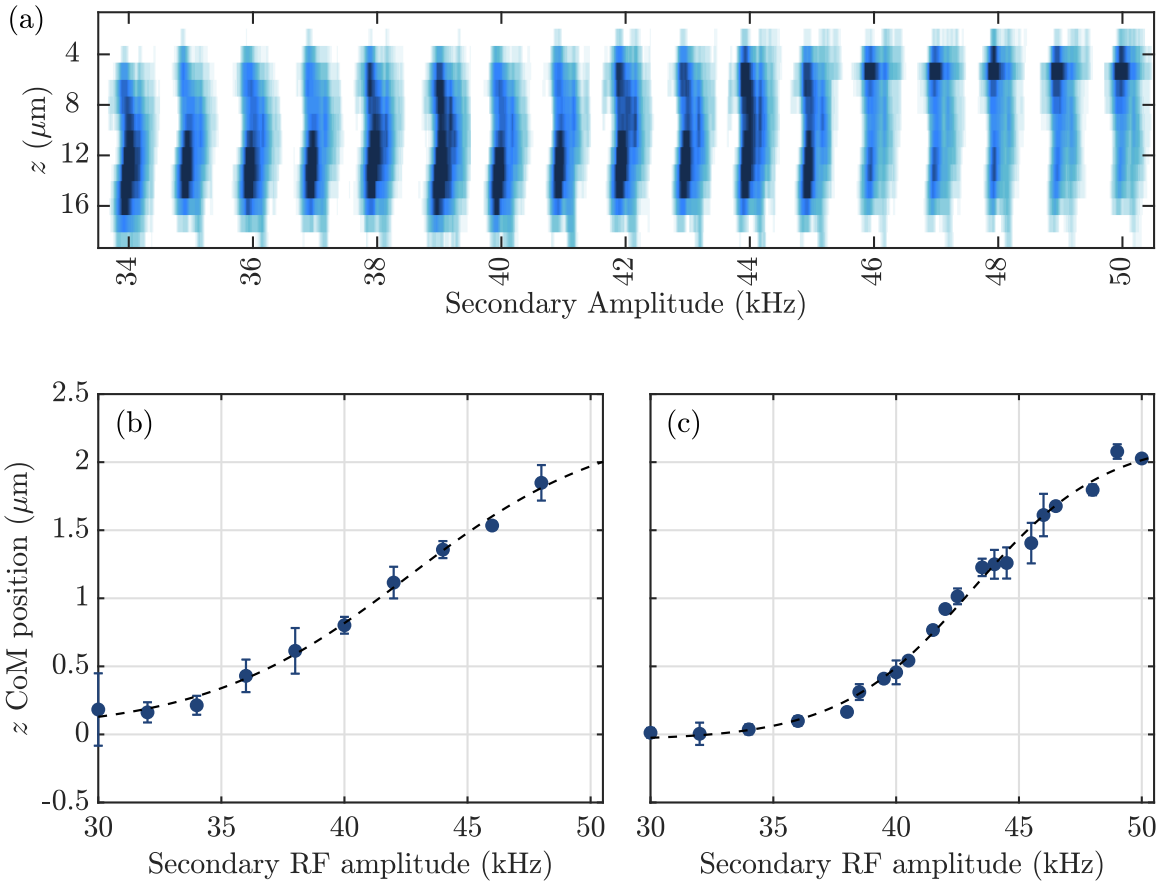

Figure 7.6: Tuning the relative populations in each well. (a) We vary the amplitude of the RF field responsible for the secondary well and imbalance the spatial distribution of trapped atoms. Images are taken *in situ*, where the BECs remain trapped by the potential, following a jump in barrier height which forces the clouds further apart. The imaging resolution is similar in scale to the separation between the wells and hence images suffer from a considerable amount of blurring. The population clearly moves from being predominantly trapped in the secondary well, which is lower in position, to the primary well, as the potential energy of the secondary well is raised. (b)-(c) Centre-of-mass positions of the trapped BECs as a function of secondary RF amplitude for barrier amplitudes of 28 mG (close to flat) and 8 mG (high barrier), respectively.

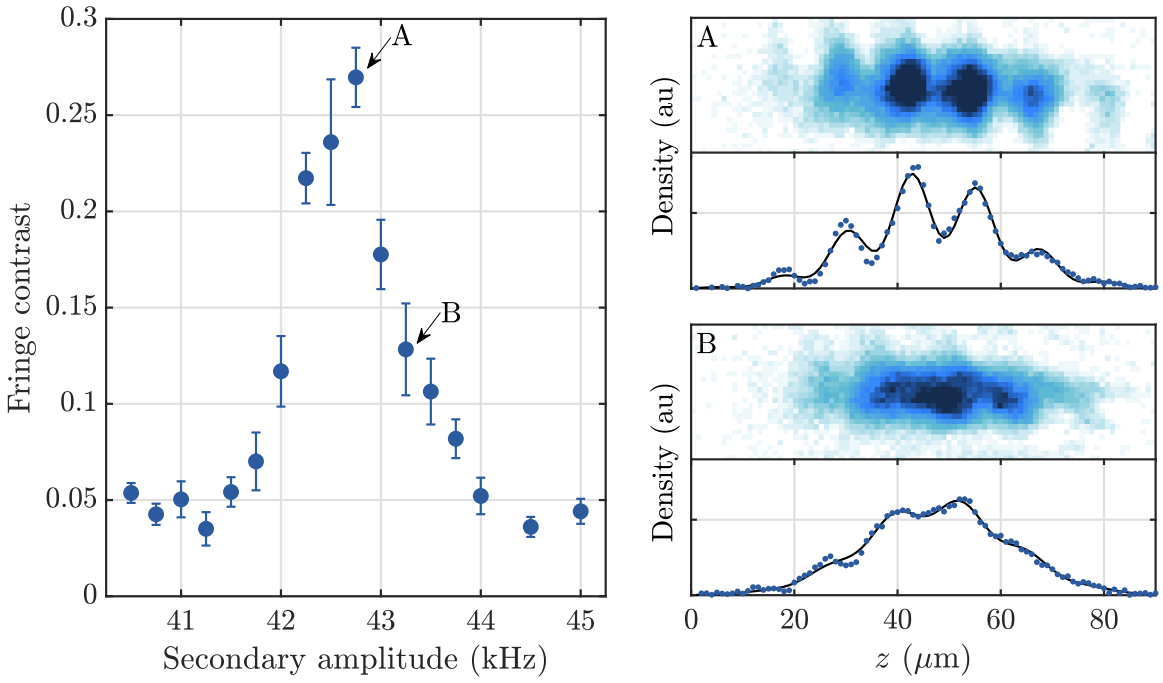

Figure 7.7: Variation of the contrast of matter-wave interference as a function of the amplitude of the RF field for the secondary well. A, B, upper: absorption images of matter-wave interference after 12 ms of TOF for secondary RF field amplitudes which correspond to Rabi frequencies of 42.75 kHz and 43.25 kHz, respectively, which are marked by arrows in the leftmost figure. A, B, lower: fits to the corresponding absorption images, from which we extract the contrast. The colour scheme is the same as in figure 7.6.

Figure 7.7 (left) illustrates the variation in A as a function of secondary RF amplitude. This clearly shows a peak where the population is balanced, which is corroborated by the observations of figure 7.6. Figure 7.7 (A & B) illustrate the absorption images (upper) for secondary RF field amplitudes marked A & B in figure 7.7 (left), and the fits of the central density profile from which we extract the contrast.

Our results demonstrate our ability to manipulate the *in situ* distribution of atoms across the double well via control of the RF field amplitudes. The balance of atoms

across the two wells is reflected in the contrast of the matter-wave interference pattern. In future experiments, the relationship between relative occupations and fringe contrast will be utilised in investigations of tunnelling dynamics in 2D systems, in a manner similar to experiments presented in references [184, 186, 197].

7.8 Outlook

Our experimental results demonstrate repeatable matter-wave interference of Bose gases confined in double-well potentials. Consequently, we observe that our splitting procedure is coherent for certain choices of experimental parameters, which is characterised by the repeatability of the matter-wave interference fringe phases across many experimental sequences.

Tunnelling dynamics will provide a means to investigate the coherent dynamics of the system, although it is not applicable for out-of-equilibrium experiments where the two clouds are intended to evolve independently. Our closest well separation of approximately 2 µm is similar to experiments elsewhere that observe tunnelling dynamics with oscillation frequencies of approximately 2-32 Hz [184,186,197]. Further reduction in the distance between the wells may improve the visibility of tunnelling dynamics however stability of the RF amplitudes and consequently the occupations of the wells remains the limiting factor at the present time. A comprehensive study of achievable tunneling frequencies in this apparatus, as well as the required RF amplitude stability, is presented in reference [57]. Additionally, for our experimental geometry of pancake-shaped Bose gases stacked on top of each other, the functional form of coherent oscillatory dynamics is not fully known and thus invites further experimental and theoretical efforts.

As the tunnel coupling can be tuned via the amplitude of the barrier, the experiment can serve as an experimental realisation of the 2D Sine-Gordon Hamiltonian,

both in and out of equilibrium, which is a subject of widespread interest in the theoretical community [198,199]. Nevertheless, tunnel coupling is not required for most of our experimental proposal concerning the time evolution of 2D Bose gases following a quench. We now discuss recent technical developments and propose subsequent studies.

7.8.1 Tomographic imaging

As we discussed in section 7.6, a major limitation of our experimental protocol was the integration of the matter-wave interference pattern along the imaging direction, which acts to reduce the contrast and the resolution with which correlations across the sample can be probed. We briefly discuss recent experimental advances on the apparatus towards solving these issues. A Digital Micromirror Device (DMD) has been recently added to the experimental apparatus by Shinichi Sunami [192]. This device comprises an array of mirrors which can be independently controlled to realise arbitrary intensity patterns and is widely used in the cold-atom community to imprint arbitrary optical potentials. Further detail on the implementation of the DMD and experimental results will be presented in subsequent theses [192].

In the proposed experimental scheme, the DMD is used in combination with the vertical imaging optics to selectively repump only atoms in a thin sheet of thickness L_y, normal to the imaging direction, as illustrated in figure 7.8 (left). The absorption image captures only the integrated density along $\hat{\mathbf{e}}_y$ over distance L_y, rather than the full width of the cloud. This method prevents the reduction in fringe contrast due to fluctuations in the phase of the fringes along the direction of the imaging system. The high visibility interference fringes in reference [200] were obtained by a similar technique, however, the optical apparatus in that case was fixed and did not offer the spatial versatility of a DMD.

Using the same analysis methods as section 7.5, the full distribution of the con-

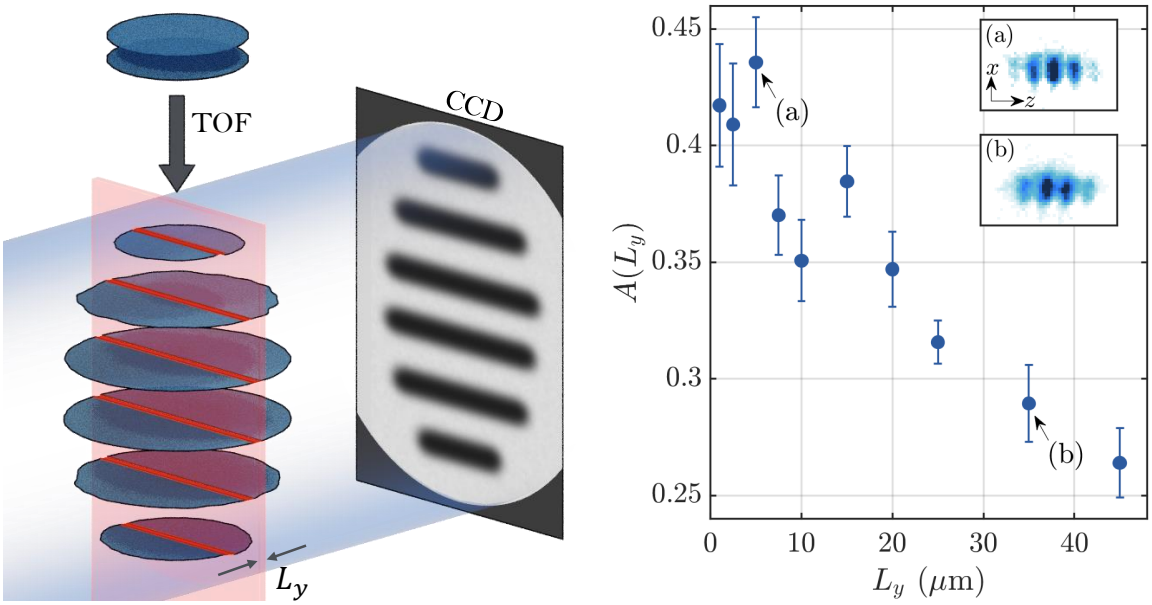

Figure 7.8: Left: schematic of the tomographic imaging experimental sequence. We begin with BECs trapped in a double-well potential before performing TOF expansion. Atoms in a state with $F = 1$ are optically pumped to $F = 2$ by a sheet of repumping light with thickness L_y. We then image atoms with $F = 2$ with cooling light, producing an absorption image. Right: preliminary results where we vary the thickness L_y of the repumping sheet and measure the contrast of matter-wave interference patterns. Inset (a)-(b): absorption images taken with L_y =2 µm and 10 µm, respectively.

trast $A(L_x, L_y, t)$ can be constructed, where t indicates the hold time before TOF. Quantum mechanics is intrinsically probabilistic: observables are characterised by distributions and thus are not limited to only their expected values. The methods presented above allow us to extract the distribution of contrast across the sample, which provides a proxy view into the underlying correlations and coherence within the sample. These experiments are the subject of ongoing work and discussion with theoretical collaborators.

7.8.2 Out-of-equilibrium dynamics

As discussed earlier, following the quench, if the PSD of the daughter clouds falls below the critical value for the BKT or BEC transitions, the system will cross the transition dynamically [188]. The time evolution can be probed readily by investigating functional form of g_1 as the system evolves: for PSDs above the critical point, g_1 decays algebraically as a function of distance, as opposed to exponentially in the normal fluid; this is a consequence of the unbinding of vortices within the sample [177]. This method provides a extremely valuable view into the evolution of correlations in the phase distribution which could otherwise not be observed in a measurement of a single cloud. Preliminary experimental results have shown that, as the daughter clouds are held for long times in the double-well potential prior to release, the functional form of $A^2(L_x)$ vs L_x evolves from algebraic decay, synonymous with a superfluid state, to exponential decay indicative of the normal fluid. Further investigation is necessary to verify that the PSD of the two daughter clouds following the quench is indeed below the critical value for the BKT transition. Nevertheless, this is qualitative indication that the daughter clouds evolve from a superheated state and progress towards equilibrium, which is an extremely exciting development and provides a basis for extensive further studies.

8

Conclusion

The results detailed in this thesis pave the way for an exciting period of future work on this apparatus. Using machine learning, we have tuned the parameters of the experiment to greatly enhance the atom numbers of BECs produced by the apparatus. Furthermore, machine learning methods are now firmly embedded into the day-to-day operation of the apparatus and have since been used to improve magnetic transport, as well as the fringe contrast in matter-wave interference experiments. Additional machine learning techniques for feature selection, for example Principal Component Analysis (PCA) or Convolutional Neural Networks, may be of great use in processing matter-wave interference fringe patterns in future out-of-equilibrium experiments, or in further characterisation of the BKT phase and its excitations. PCA, for instance, has been deployed elsewhere to identify the Bogoliubov modes and the superfluid transition in a 2D Bose gas [201, 202].

The latter part of this thesis focuses on MRF-dressed potentials, which were used

to realise a species-selective double-well potential, the coherent splitting and matter-wave interference of a quantum gas, and to perform out-of-equilibrium experiments using a Bose gas in the 2D regime. We used the species-selective double-well potential to demonstrate spatial manipulation of hyperfine states of ^{87}Rb, which forms a promising first step towards realising sub-nK thermometry schemes [123–125], or probing the excitations within a superfluid via an immersed impurity [121, 122]. The scales of spatial manipulation can be reduced to the sub-µm level, which diffraction-limited optical methods would struggle to achieve, and can be as easily lengthened through control of the RF fields and magnetic field gradient. While several future experimental directions are proposed in the relevant chapters, we briefly consider an additional application of the species-selective double well, as well as future directions for probing the out-of-equilibrium dynamics of 2D Bose gases.

8.1 A gravitational gradiometer

Cold atoms have been used in many contexts as probes of gravitational field strength, acceleration or rotation [196, 203, 204]. We propose an application of the species-selective double well as a gravitational gradiometer, via the schematic shown in figure 8.1.

For the purpose of this explanation, we refer to the states with $F = 1$, $\tilde{m}_F = 1$ and $F = 2$, $\tilde{m}_F = 1$ as $|1\rangle$ and $|2\rangle$, respectively. The experimental protocol is as follows: $|1\rangle$ is transferred to $(|1\rangle + |2\rangle)/\sqrt{2}$ via a $\pi/2$ pulse. The amplitude of the $B_2 - A_2$ field is raised to split $|1\rangle$ across the double well, such that 50% of the population is transferred into each well over a time ΔT. The gravitational field strength $|g|$ is illustrated in figure 8.1, where we assume a linear variation in the magnitude over the range of the separation $2\Delta z$ between the two wells, such that the difference between the top and the bottom is $2\Delta|g|$. We also assume the duration of the $\pi/2$ pulse $\delta T \ll \Delta T$. At

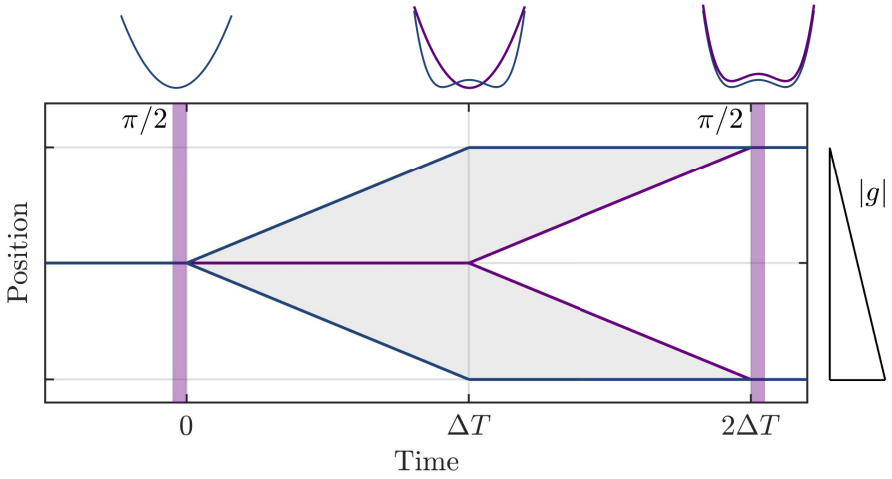

Figure 8.1: A gravitational gradiometer for atoms with $F = 1$ and $F = 2$. A cloud of atoms with $F = 1$ are transferred to a balanced superposition of $F = 1$ and $F = 2$ via a MW $\pi/2$ pulse. The $F = 1$ cloud is split into the double well over a time ΔT, and the $F = 2$ cloud is split similarly ΔT later. A second $\pi/2$ pulse is applied and the final populations analysed to deduce $\Delta|g|/\Delta z$. The gravitational field strength is indicated (right). This figure is adapted from an earlier version by Elliot Bentine.

time ΔT, after the $|1\rangle$ cloud has been split, the state is $\psi(\Delta T) = |1\rangle^u + |2\rangle^m + |1\rangle^l$, where

$$
\begin{aligned}
|1\rangle^u &= \frac{1}{2\sqrt{2}} \exp\left(\frac{-iM(|g| + \Delta|g|)\Delta z \Delta T}{2\hbar}\right)|1\rangle \\
|2\rangle^m &= \frac{1}{\sqrt{2}} \exp\left(\frac{iM|g|\Delta T}{\hbar}\right)|2\rangle \\
|1\rangle^l &= \frac{1}{2\sqrt{2}} \exp\left(\frac{iM(|g| - \Delta|g|)\Delta z \Delta T}{2\hbar}\right)|1\rangle
\end{aligned}
$$

and the superscripts u, m, l refer to upper, middle and lower wells, respectively. The amplitude of the $B_2 - A_2$ field is then lowered while the $B_2 + A_2$ field is reduced to zero over a time ΔT, which also forms a double well for $|2\rangle$. During this procedure, the split $|1\rangle$ clouds remain at $\pm\Delta z$. Finally, a $\pi/2$ pulse is applied, such that $|1\rangle \to (|1\rangle + |2\rangle)/\sqrt{2}$ and $|2\rangle \to (|2\rangle - |1\rangle)/\sqrt{2}$. The populations $n_1^{u,l}$of the $|1\rangle$ state in each

well are thus given by $n_1^{u,l} = |\langle 1|\psi^{u,l}\rangle|^2$, to yield

$$n_1^u(\Delta T, \Delta z) = \frac{1}{8}\left(1 - \cos(A^+(\Delta T, \Delta z))\right) \ ,$$
$$n_1^l(\Delta T, \Delta z) = \frac{1}{8}\left(1 - \cos(A^-(\Delta T, \Delta z))\right) \ ,$$

where we have defined $A^+ = M(|g|+\Delta|g|)\Delta z \Delta T/\hbar$ and $A^- = M(|g|-\Delta|g|)\Delta z \Delta T/\hbar$. The oscillations in the population of the $|1\rangle$ state can be probed as a function of ΔT or Δz to determine $\Delta|g|/\Delta z$. Furthermore, the scheme may be extended by the addition of other RF components, which may form triple wells or lattices. The number of wells defines the highest-order derivatives of $|g|$ which may be detected, thus an extension to three wells will permit detection of $d^2|g|/dz^2$. A full formulation of this scheme is left for future discussion, as well as considerations regarding the stability requirements on RF amplitudes which may be difficult to fulfil.

8.2 Out-of-equilibrium dynamics of 2D systems

We discussed future directions for the experimental schemes presented in Chapters 6 and 7 in their respective chapters. In summary, in Chapter 6, we performed a radial perturbation of the cloud by exploiting the energy level structure of the shell trap. Significant further investigation is required to attribute our preliminary observations to predicted relaxation mechanisms, such as phonon propagation and the unbinding of vortices [178]. We note further that our current realisation of this scheme concerns a gas which is already condensed, and dynamics may consequently drive the system to thermalise, thus losing its quasi-long-range order. The scheme could be easily repeated for a thermal gas, such that the out-of-equilibrium dynamics may act to condense the gas and consequently drive the formation of quasi-long-range order. This is related to the archetypal Kibble-Zurek mechanism, which concerns the characteristic timescales and length scales of the formation of order when crossing a phase

transition [189, 205].

An advantage of the RF pulse method of forming an out-of-equilibrium distribution, as opposed to splitting a gas using the double-well potential scheme outlined in Chapter 7, is there are significantly fewer experimental components: only 1 dressing RF field is required and there are no complications with tomographic imaging or shot-to-shot variations in the proportions of atoms loaded into the double well. However, the method does not as easily allow us to investigate the phase fluctuations, which are directly observable using matter-wave interference and provide a rich source of information on the time evolution of 2D systems. Despite the experimental complications, a matter-wave interference approach is likely to reveal a deeper wealth of information regarding the dynamics of the system, and ultimately permit the reconstruction of probability distributions for observables, thus capturing the true essence of quantum mechanics.

An additional experimental direction is to investigate vortices in the out-of-equilibrium trapped gas, which may observed via in-plane expansion or in the matter-wave interference pattern after TOF, which will provide insight into the formation of phase singularities as the distribution relaxes. The existence of a free vortex is signalled by a π phase slip in the matter-wave interference pattern, as was observed in reference [24]. While preliminary at this stage, in some absorption images we observe an indication of this characteristic, as shown in figure 8.2 (left). The characteristic 'zip' pattern is observed, particularly in the top left of the distribution. This image were taken without tomographic imaging, and thus suffers from blurring due to integration over the thermal component. We fit the distribution using a 2D Gaussian function and plot the residuals in figure 8.2 (right), which are scaled by the average density within a 8×8 pixel region about the point to boost signals in lower density regions; we also add a guide (red) to indicate the zip pattern. Experiments of this nature, which focus on the binding or unbinding of vortices as the gas equilibrates will provide valuable

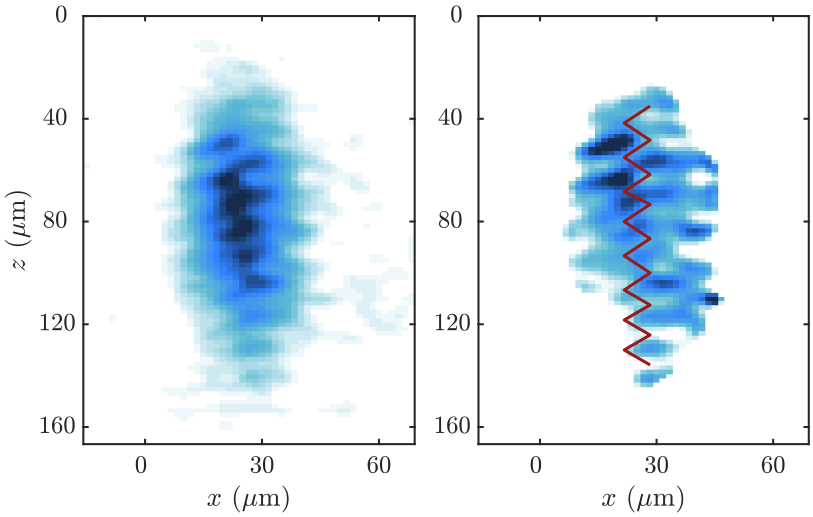

Figure 8.2: Signature of unbound vortices in Matter-Wave Interference patterns. Left: matter-wave interference pattern of 2D clouds after 12 ms TOF. The alternating 'zip' pattern is increasingly apparent towards the top of the cloud. Right: plot of residuals between the density distribution (left) and a 2D Gaussian fit of the density distribution. A red line is added as a guide to highlight the zip pattern.

information concerning the evolution of the phase distribution in time, including the onset of phase defects, and the relevant time scales.

A

Simulating a finite-temperature quantum gas

I simulate the density profiles of a pure BEC and a BEC coupled to a finite-temperature thermal component. I solve the coupled Hartree-Fock equations for the BEC and the single-particle excited states occupied by the thermal component using numerical methods. The simulation predicts the *in situ* density distribution, and can be applied to time-dependent processes, such as TOF expansion. The framework can be extended to include time-dependent potentials, such as a moving optical lattice used in a Bragg diffraction experiment.

A.1 The Hartree-Fock approximation

We assume, in the Hartree-Fock approximation, that the many-body, ground-state wave function $\psi(\mathbf{r}_i, \mathbf{r}_j, \ldots, \mathbf{r}_N)$ of the BEC is a fully-symmetrised combination of single-particle wave functions $\phi(\mathbf{r}_i)$ [94, 206]. Furthermore, we consider an effective pair-wise interaction $g\,\delta(\mathbf{r}-\mathbf{r'})$ between atoms at $\mathbf{r}$ and $\mathbf{r'}$. Incorporating all pair-wise combinations, the total energy of N bosons is

$$E = \frac{N(N-1)}{2V}\, g \approx \frac{1}{2} V n^2 g \quad , \tag{A.1}$$

where $n = N/V$ and V is the volume of the gas. The condensate wave function is normalised such that the number density $n(\mathbf{r}) = |\psi(\mathbf{r})|^2$. Including an external potential $V_{\text{ext}}(\mathbf{r})$, to first order in $1/N$, the energy of the system is

$$E(\psi) = \int d^3\mathbf{r} \left[\frac{-\hbar^2}{2M} |\nabla\psi(\mathbf{r})|^2 + V_{\text{ext}}(\mathbf{r})|\psi(\mathbf{r})|^2 + \frac{1}{2} g |\psi(\mathbf{r})|^4 \right] . \tag{A.2}$$

Equation A.2 can be minimised using the method of Lagrange multipliers: the energy is minimised with respect to variations in $\psi(\mathbf{r})$ and subject to the constraint that the total atom number is constant. This leads to the time-independent Gross-Pitaevskii equation [207, 208]:

$$-\frac{\hbar^2}{2M}\nabla^2\psi(\mathbf{r}) + V_{\text{ext}}(\mathbf{r})\,\psi(\mathbf{r}) + g|\psi(\mathbf{r})|^2\,\psi(\mathbf{r}) = \mu\,\psi(\mathbf{r}) \ , \tag{A.3}$$

where the chemical potential is represented by the eigenvalue μ, $g\,|\psi(\mathbf{r})|^2$ represents the mean-field interaction and $g = 4\pi\hbar^2 a/M$, which is the strength of s-wave interactions in the 3D regime [94]. In the Thomas-Fermi limit, we neglect kinetic energy, leading to the familiar Local-Density Approximation (LDA) result for the BEC num-

ber density $n_0(\mathbf{r})$, where

$$n_0(\mathbf{r}) = \frac{\mu - V_{\text{ext}}(\mathbf{r})}{g} \ . \tag{A.4}$$

We impose an additional boundary condition such that the wave function decays to zero at the walls of the trap or at the limit of the simulated spatial region.

A.2 Coupled Gross-Pitaevskii equations

Following the discussion of Pitaevskii and Stringari [206], at finite temperature, thermal depletion significantly modifies the ground state occupancy. The Hartree-Fock approximation provides a formulation for the densities of the BEC and thermal components. We begin from the many-body Hamiltonian

$$\hat{H} = \int d\mathbf{r} \ \psi^\dagger \left(-\frac{\hbar^2 \nabla^2}{2M} + V_{\text{ext}} \right) \psi \quad + \quad \frac{g}{2} \int d\mathbf{r} \ \psi^\dagger \psi^\dagger \psi \psi \ , \tag{A.5}$$

where

$$\psi(\mathbf{r}) = \sum_i \phi_i(\mathbf{r}) \hat{a}_i \tag{A.6}$$

in the basis of single-particle wavefunctions ϕ_i and where $\hat{a}_i$ is the single-particle annihilation operator. The Hartree-Fock approximation assumes that, in equilibrium, the many-body wavefunction can be decomposed into single-particle excitations with average occupation number

$$n_i = \left\langle \hat{a}_i^\dagger \hat{a}_i \right\rangle \ . \tag{A.7}$$

We note further that terms in the Hamiltonian which are quadratic in field operators, for example $\left\langle \hat{a}_i^\dagger \hat{a}_i^\dagger \right\rangle$ vanish. We express the BEC and thermal component wave functions and occupations as

$$n_0(\mathbf{r}) = N_0 |\psi_0(\mathbf{r})|^2 \text{ and } n_T(\mathbf{r}) = \sum_{i \neq 0} n_i |\phi_i(\mathbf{r})|^2 \tag{A.8}$$

respectively. In the derivation of these expressions, it was assumed that the condensed number $N_0 \gg 1$. The average occupations of thermal states n_i are found by minimising the grand canonical energy $E - TS - \mu N$ which leads to the standard result for bosons:

$$n_i = \frac{1}{\exp \beta(\epsilon_i - \mu) - 1} \ . \tag{A.9}$$

where $\beta = 1/k_B T$ and ϵ_i are the excited state energies. The mechanism of Bose-Einstein condensation proceeds as a macroscopic occupation the ground state of a system described by coupled Gross-Pitaevskii-like equations, where

$$\left(-\frac{\hbar^2}{2M} \nabla^2 + V_{\text{ext}}(\mathbf{r}) + g \left[n_0(\mathbf{r}) + 2 n_T(\mathbf{r}) \right] \right) \psi_0(\mathbf{r}) = \mu \, \psi_0(\mathbf{r}) \tag{A.10}$$

applies to the condensate and

$$\left(-\frac{\hbar^2}{2M} \nabla^2 + V_{\text{ext}}(\mathbf{r}) + 2g \left[n_0(\mathbf{r}) + n_T(\mathbf{r}) \right] \right) \phi_i(\mathbf{r}) = \epsilon_i \, \phi_i(\mathbf{r}) \tag{A.11}$$

to the single-particle excited states. We solve these equations in a self-consistent manner subject to the normalisation constraint

$$N = \int d\mathbf{r} \ n(\mathbf{r}) = \int d\mathbf{r} \left(n_0(\mathbf{r}) + n_T(\mathbf{r}) \right) \ . \tag{A.12}$$

We assume that states ϕ_i are orthogonal and ignore small corrections which arise from this assumption.

A.2.1 Single-particle excited states

To construct the density distribution of the BEC and the thermal component, we must solve the coupled Gross-Pitaevskii equations for each thermal excited state. The relative occupation of each state, as described by equation A.9, is defined by

the temperature of the system. To calculate the eigenstates and eigenvalues of the single-particle Hamiltonian, as required by equation A.11, it is more convenient to use discrete methods, rather than pseudo-spectral methods which are introduced later. We solve the following Hamiltonian

$$\hat{H} = \int d\mathbf{r}\ \psi^\dagger \left(-\frac{\hbar^2 \nabla^2}{2M} + V_{\text{eff}} \right) \psi\ , \tag{A.13}$$

where $V_{\text{eff}} = V_{\text{ext}} + 2g[n_0(\mathbf{r}) + n_T(\mathbf{r})]$ is the effective potential which incorporates the external potential and the mean fields. We diagonalise this Hamiltonian using the method of finite-differences, to find the second derivative with respect to position. We take the definition of the first derivative, accurate to $\mathcal{O}(h^2)$, as

$$f'(x) = \lim_{h \to 0} \frac{f(x+h) - f(x-h)}{2h}\ , \tag{A.14}$$

and the second derivative to be

$$f''(x) = \lim_{h \to 0} \frac{f(x+h) - 2f(x) + f(x-h)}{h^2}\ . \tag{A.15}$$

Figure A.1 indicates the 6 lowest-energy single-particle states of the 1D harmonic oscillator potential $V_{\text{ext}} = M\omega^2 x^2/2$ with a trap frequency $\omega = 2\pi \times 40\,\text{Hz}$, in the absence of a BEC such that $V_{\text{eff}} = V_{\text{ext}}$. We can also extend this calculation to 3D cylindrical (r, z) or Cartesian systems (x, y, z).

A.3 Numerical solution of the Gross-Pitaevskii equation

We now discuss methods of solving the Gross-Pitaevskii-like equations (equations A.10 and A.11). We present the split-step Fourier method for finding ground states and

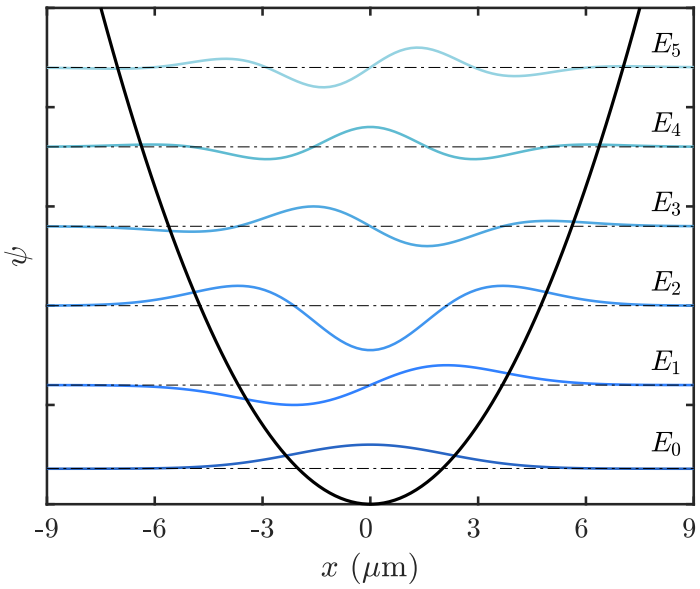

Figure A.1: Eigenstates and eigenenergies of a ^{87}Rb atom in a harmonic potential $V_{\text{ext}} = m\omega^2 x^2/2$ with a trap frequency $\omega = 2\pi \times 40\,\text{Hz}$.

performing time evolution of wavefunctions. We first consider a BEC and later extend the method to consider coupled systems at finite temperature.

We consider the application of split-step Fourier method [209]. Equation may be expressed as $\hat{H} = \hat{V} + \hat{T}$ where, in 1D, the kinetic energy operator $\hat{T} = -\hbar^2/2M\, d^2/dx^2$ and the potential energy operator $\hat{V}$ includes the external potential; the following methods also apply when potential is modified to include the mean-field interaction term, such that $V_{\text{eff}}(x) = V_{\text{ext}}(x) + 2g|\psi|^2$. Integrating between timesteps t and $t + \Delta t$ leads to the time-dependent equation:

$$\psi(x, t + \Delta t) = e^{-i\hat{H}\Delta t/\hbar}\psi(x, t) \ . \tag{A.16}$$

The operators $\hat{V}$ and $\hat{T}$ do not commute, however the approximation

$$e^{-i\hat{H}\Delta t/\hbar}\psi(x, t) \approx e^{-i\hat{V}\Delta t/2\hbar}e^{-i\hat{T}\Delta t/\hbar}e^{-i\hat{V}\Delta t/2\hbar}\psi(x, t) \ . \tag{A.17}$$

is valid to $\mathcal{O}(\Delta t^3)$. We can further simplify the problem by noting that the operator

$\hat{V}$ is diagonal in real (x) space and the operator $\hat{T}$ is diagonal in reciprocal (k) space. This feature can be exploited by applying the operators to the wave function in the relevant space. Equation A.17 can therefore be written

$$\psi(x, t + \Delta t) \approx e^{-i\hat{V}\Delta t/2\hbar}\mathcal{F}^{-1}\left[e^{-i\hat{T}\Delta t/\hbar}\mathcal{F}\left[e^{-i\hat{V}\Delta t/2\hbar}\psi(x, t)\right]\right] \ , \tag{A.18}$$

where $\mathcal{F}$ and $\mathcal{F}^{-1}$ denote the Fourier transform and inverse Fourier transform operations, respectively. This method incorporates period boundary conditions, owing to the finite range imposed by the solution grids in both real and reciprocal space. The computational cost of performing successive Fourier (and inverse Fourier) transforms is low, owing to fast numerical techniques such as fast Fourier transforms.

A.3.1 Imaginary time propagation

The ground state can be found conveniently using the method of imaginary time propagation [210]. The wavefunction can be expressed as a linear combination of eigenstates $\phi_i(\mathbf{r})$ with time-dependent probabilities $|a_i(t)|^2$ and energies $E_i(t)$, such that $\psi(\mathbf{r}, t) = \sum_i a_i(t)\phi_i(\mathbf{r})$. Performing the substitution $t \to -it$, we find the imaginary time evolution of the wavefunction can be expressed as

$$\psi(\mathbf{r}, -it - i\Delta t) = e^{-\hat{H}\Delta t/\hbar}\psi(\mathbf{r}, t) = \sum_i a_i(t)\phi_i(\mathbf{r})e^{-E_i\Delta t/\hbar} \ . \tag{A.19}$$

The amplitude of each eigenstate contribution decays over time however the lowest energy (ground) state decays with the slowest rate. Renormalising the wavefunction after each time step $-i\Delta t$, to conserve the number of particles, directs the solution to evolve towards the true ground state in the limit $t \gg \hbar/E_0$. We monitor convergence via the chemical potential: the chemical potential can be evaluated using the

expression

$$\mu = \frac{\hbar}{\Delta t} \ln \left| \frac{\psi(\mathbf{r}, t)}{\psi(\mathbf{r}, t + \Delta t)} \right| \tag{A.20}$$

at any position $\mathbf{r}$ within the condensate. The solution is terminated when the relative change between the calculated μ in successive time steps does not exceed a threshold[1]. Divergent solutions can be managed similarly.

The algorithm is summarised as follows: the physical constants and experimental parameters are first defined, including atomic properties, atom number and trap frequencies. We consider 1D traps, and consequently discretise position-space and momentum-space representations of the wave function into grid points with spacing Δx (`dx`) and Δk (`dk`), respectively, extending over the ranges `x` $= [(-P + 1)$`dx`$, P$`dx`$]$ and `k` $= [(-P + 1)$`dk`$, P$`dk`$]$, where `dk` $= \pi/(P$`dx`$)$ and P is an integer power of 2; this improves computation time when performing numerical Fourier transforms. We provide an initial estimate of the condensate wave function, in this case a Gaussian distribution, which is a solution to equation A.3 in the limit of no interactions, and define an interaction strength. For the case of a 1D system, we use the modified interaction strength: $g_{1D} = 2\hbar^2 a/(M l_x^2)$, where l_x is the harmonic oscillator length. We then go on to perform the imaginary time propagation to find the ground state and choose the trap centre to evaluate of the convergence of μ during the interation. We begin the imaginary time evolution to find the ground state using equation A.19 and terminate the procedure when μ converges or diverges. The algorithm code is provided below for a 1D system and implemented for the Matlab programming language.

[1]In this simulation, we choose to terminate the iteration when $\mu(t + \Delta t)/\mu(t) < 10^{-6}$.

```
hbar=1.054e-34; amu=1.660538921e-27; m=87*amu; as=5.8e-9; % Constants
N=1000; wr=100*2*pi; wx=40*2*pi;  % Simulation parameters
M=256; Nx=2*M; % Grid parameters
dx=double(2e-7); x=(-M:1:M-1)*dx;
dk=pi/(M*dx); k=(-M:1:M-1)*dk;
dt=double(10e-8); Nt=200000; % Timesteps

lx=sqrt(hbar/(m*wx));
g1d=2*hbar*hbar*as/(m*lx2); % Define interactions
V=0.5*m*wx2*x.2/hbar; % Define potential

psi_0=sqrt(N/lx)*(1/pi)(1/4)*exp(-x.2/(2*lx2)); % Trial wave function
psi_mid_old=psi((Nx-1)/2);

mu_old=1; j=1; mu_error=1;

while mu_error > 1e-6
psi=psi.*exp(-0.5*dt*(V+(g1d/hbar)*abs(psi).2)); % Apply PE operator
psi_k=fftshift(fft(psi))/Nx;
psi_k=psi_k.*exp(-0.5*dt*(hbar/m)*k.2); % Apply KE operator
psi=ifft(ifftshift(psi_k))*Nx;
psi=psi.*exp(-0.5*dt*(V+(g1d/hbar)*abs(psi).2)); % Apply PE operator
psi_mid=psi((Nx-1)/2);
mu=log(psi_mid_old/psi_mid)/dt; % Calculate mu
mu_error=abs(mu-mu_old)/mu;
psi=psi*sqrt(N)/sqrt((dx*norm(psi).2)); % Renormalise

if mod(j,5000)==0
mu_error
end
if j>1e6
print('Divergence')
break
end

mu_old=mu; j=j+1;
end
```

The numerical solution can be extended to 2D and 3D cases using the appropriate grids and numerical Fourier transform methods. We begin by simulating $4,000$ ^{87}Rb atoms in a 1D harmonic potential with 40 Hz trap frequency. We perform the imaginary time propagation procedure to find the BEC ground state. Figure A.2 shows

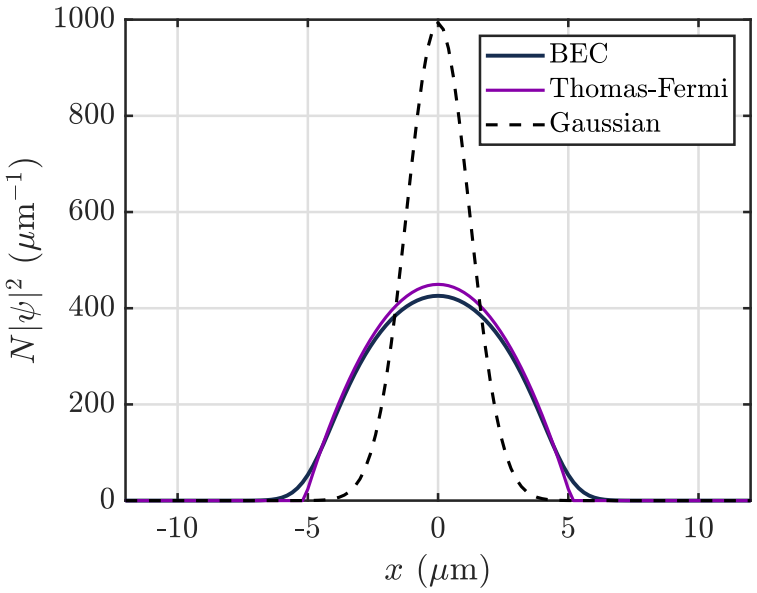

Figure A.2: Simulated density profiles of trapped gases. We illustrate the Gaussian ground state (dotted), which is used as a trial solution for the Gross-Pitaevskii equation solver. The density distributions found using Thomas-Fermi approximation (purple) and the Gross-Pitaevskii equation solver (blue) are also displayed.

the simulated density profile (blue), as well as the Gaussian (non-interacting) trial wave function (black, dashed) and the Thomas-Fermi limit (purple).

A.3.2 The time-dependent solution

Following the calculation of the interacting ground state, we evolve the time-dependent Gross-Pitaevskii equation. The time coordinate is no longer replaced by an imaginary pseudo-time and the process is iterated in increments of `dt`. The time iteration step is repeated `Nt` times to realise a real-time evolution up to `Nt` $\times$ `dt`. TOF expansion can be simulated by enforcing $V_{\text{ext}} = 0$ at the beginning of time evolution. Figure A.3 illustrates 20 ms of TOF expansion for the BEC illustrated in figure A.2.

A similar method can be applied to time-dependent potentials, such as moving optical lattices used in Bragg diffraction experiments [211], or to investigate dynamics of the trapped gas, such as modes of oscillation.

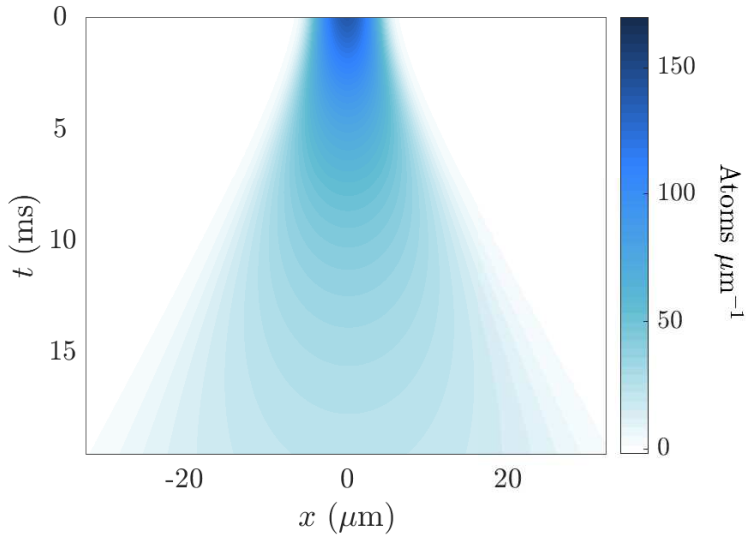

Figure A.3: Simulating TOF for an interacting gas. The trap is turned off at $t = 0$, such that $V_{\text{ext}} = 0$, and the cloud expands. The left axis indicates the TOF and the 1D density distribution is represented by the horizontal cross-section at time t.

A.4 Coupled gases

We extend this approach to solve for both the condensate and the coexisting thermal component, as described by equations A.10 and A.11. We modify the interaction term in the Hamiltonian to account for the interaction between thermal component and a BEC described by ψ_0. In solving the coupled system, we find the single-particle states for the pseudo-potential which includes the mean-field energy of the BEC, $V_{\text{eff}}(\mathbf{r}) = V_{\text{ext}}(\mathbf{r}) + 2gn_0(\mathbf{r})$, which we can find using the finite-element methods defined in section A.2.1. We truncate the infinite basis of single-particle excited states to include only 6 states and populate them according to the Bose-Einstein distribution (equation A.9), given the temperature of the system and the chemical potential of the BEC. The number of atoms in the harmonically-trapped condensate is given by $N_0 = N\left(1 - (T/T_c)^d\right)$, where T is the temperature, d is the system dimensionality and T_c is the interaction strength-dependent critical temperature. We apply the Fourier split-step method in order to find the ground state for the BEC and

repeatedly find the single-particle excited states of the new Hamiltonian, populating the thermal states according to their eigenvalue. We iterate this procedure until convergence of the chemical potential of the BEC. The modified algorithm to find the ground states is outlined as follows.

```
psi0_mid_old=psi0((Nx)/2);
truncationLimit=6; mu_old=1; j=1; mu_error=1;

while mu_error > 1e-6
% Apply PE operator
psi0=psi0.*exp(1).^(-0.5*dt*(V+(g1d/hbar)*(psi0.^2+2*sum(psiT.^2,1))));
psi_k = fftshift(fft(psi0))/Nx;
psi_k = psi_k.*exp(1).^(-0.5*dt*(hbar/m)*k.^2); %Apply KE operator
psi0 = ifft(ifftshift(psi_k))*Nx;
% Apply PE operator again
psi0=psi0.*exp(1).^(-0.5*dt*(V+(g1d/hbar)*(psi0.^2+2*sum(psiT.^2,1))));

psi0_mid = psi0((Nx)/2);
mu = log(psi0_mid_old/psi0_mid)/dt;
mu_error=abs(mu-mu_old)/mu;
psi0 = psi0*sqrt(N0)/sqrt((dx*norm(psi0).^2)); % N0 is condensate number

% Find single particle eigenstates
[vs,lambdas] = singleParticleEigenstates(x,(V+(2*g1d/hbar)*(psi0.^2+ ...
... sum(psiT.^2,1)))');
% Calculate occupations using Bose-Einstein distribution
[nEx] = calculateOccupations(T,mu,lambdas); % Define occupations
ind = min(find(nEx > 0));
% Truncate set of excited states
nEx = nEx(ind:ind+truncationLimit);
psiT = vs(:,ind:ind+truncationLimit);

psi0_mid = psi0((Nx)/2);
mu = log(psi0_mid_old/psi0_mid)/dt; % Check mu
mu_error=abs(mu0-mu0_old)/mu0;
% Populate thermal states
psiT = nEx.*psiT*sqrt(N-N0)/sqrt(dx*norm(psiT).^2);

if mod(j,5000)==0
mu_error; end
if j>1e4
print('Divergence') break; end
mu_old = mu; j=j+1; end
```

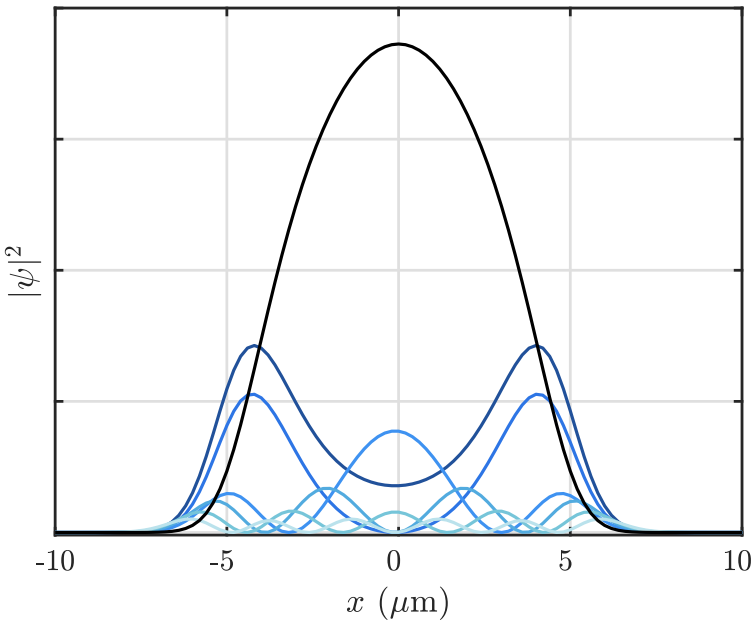

Figure A.4: Occupations of ground (black) and 6 excited states (blue) in the trapped, finite-T system. Single-particle states with higher energy are indicated by lighter blue colours. The thermal component occupies the excited states, with relative occupations in these states determined by the Bose-Einstein distribution for the eigenenergies of the states and the system temperature.

The function `singleParticleEigenstates` and `calculateOccupations` implement the finite-difference methods to solve equation A.13 and to calculate excited state occupations using equation A.9. An example profile for $4,000$ atoms in a potential with $\omega = 2\pi \times 40\,\text{Hz}$ and at temperature $20\,\text{nK}$ is shown in figure A.4. Source code for the methods defined earlier can be found in *https://bitbucket.org/footgroup/coupledgpue*.

A.5 Conclusion

We have presented a numerical solution to the Gross-Pitaevskii equation. Imaginary time methods were applied to find the ground state of a BEC, and real time evolution is used to simulate TOF expansion or to investigate time-dependent dynamics of the BEC. We have extended the algorithm to solve the coupled Hartree-Fock equations, which describe a BEC and thermal component of a finite-T quantum gas.

Experimentally, temperature is often extracted by performing free expansion in TOF and by analysing the Gaussian 'wings' of the density distribution. However, this method ignores the interaction between the BEC and the thermal component, which can lead to systematic shifts. Therefore, an application of our numerical solution is to predict exact density distributions for finite-T gases after TOF where precise thermometry is required.

The numerical methods defined within this chapter have since been applied in the simulation of a Bragg diffraction experiment, where a moving optical lattice is applied to a trapped gas to investigate its momentum distribution and excitation spectrum [211]. Ongoing work focuses on understanding the features of Bragg diffraction in a harmonically-trapped system, including the resonance line shape and the time-evolution of the diffracted component. Furthermore, these methods have been applied to systems of coupled condensates, such as those in Chapter 5 section 5.5. Preliminary experimental observations suggest that the minority $F = 2$ condensate is 'split' by the large mean-field of the $F = 1$ condensate. The numerical methods have been applied to find the ground state and first excited state of the $F = 2$ condensate and to investigate the feasibility of tunnelling through the 'soft barrier' defined by the central condensate.

Bibliography

[1] Immanuel Bloch, Jean Dalibard, and Wilhelm Zwerger. Many-body physics with ultracold gases. *Reviews of Modern Physics*, 80(3):885–964, 2008.

[2] Immanuel Bloch, Jean Dalibard, and Sylvain Nascimbène. Quantum simulations with ultracold quantum gases. *Nature Physics*, 8(4):267–276, 2012.

[3] Albert Einstein. Quantentheorie des einatomigen idealen Gases. *Wissenschaften, Verlag der Königlich-Preussischen Akademie*, pages 261–267, 1924.

[4] S N Bose. Plancks Gesetz und Lichtquantenhypothese (German translation). *Z. Phys (Germany)*, 26:178–181, 1924.

[5] M. H. Anderson, J. R. Ensher, M. R. Matthews, C. E. Wieman, and E. A. Cornell. Observation of Bose-Einstein Condensation in a Dilute Atomic Vapor. *Science*, 269(5221):198–201, 1995.

[6] K. B. Davis, M. O. Mewes, M. R. Andrews, N. J. van Druten, D. S. Durfee, D. M. Kurn, and W. Ketterle. Bose-Einstein Condensation in a Gas of Sodium Atoms. *Physical Review Letters*, 75(22):3969–3973, 1995.

[7] I. Ferrier-Barbut, M. Delehaye, S. Laurent, A. T. Grier, M. Pierce, B. S. Rem, F. Chevy, and C. Salomon. A mixture of Bose and Fermi superfluids. *Science*, 345(6200):1035–1038, 2014.

[8] S. Ospelkaus, K.-K. Ni, M. H. G. de Miranda, B. Neyenhuis, D. Wang, S. Kotochigova, P. S. Julienne, D. S. Jin, and J. Ye. Ultracold polar molecules near quantum degeneracy. *Faraday Discussions*, 142:351, 2009.

[9] T Lahaye, C Menotti, L Santos, M Lewenstein, and T Pfau. The physics of dipolar bosonic quantum gases. *Reports on Progress in Physics*, 72(12):126401, 2009.

[10] Elizabeth A. Donley, Neil R. Claussen, Sarah T. Thompson, and Carl E. Wieman. Atom-molecule coherence in a Bose-Einstein condensate. *Nature*, 417(6888):529–533, 2002.

[11] S. Jochim. Bose-Einstein Condensation of Molecules. *Science*, 302(5653):2101–2103, 2003.

[12] K. Xu, T. Mukaiyama, J. R. Abo-Shaeer, J. K. Chin, D. E. Miller, and W. Ketterle. Formation of Quantum-Degenerate Sodium Molecules. *Physical Review Letters*, 91(21):210402, 2003.

[13] M. W. Zwierlein, C. A. Stan, C. H. Schunck, S. M. F. Raupach, A. J. Kerman, and W. Ketterle. Condensation of Pairs of Fermionic Atoms near a Feshbach Resonance. *Physical Review Letters*, 92(12):120403, 2004.

[14] K. M. O'Hara. Observation of a Strongly Interacting Degenerate Fermi Gas of Atoms. *Science*, 298(5601):2179–2182, 2002.

[15] B. DeMarco. Onset of Fermi Degeneracy in a Trapped Atomic Gas. *Science*, 285(5434):1703–1706, 1999.

[16] M. Holland, S. J. J. M. F. Kokkelmans, M. L. Chiofalo, and R. Walser. Resonance Superfluidity in a Quantum Degenerate Fermi Gas. *Physical Review Letters*, 87(12):120406, 2001.

[17] D. S. Petrov, M. Holzmann, and G. V. Shlyapnikov. Bose-Einstein Condensation in Quasi-2D Trapped Gases. *Physical Review Letters*, 84(12):2551–2555, 2000.

[18] D. S. Petrov, G. V. Shlyapnikov, and J. T. M. Walraven. Phase-Fluctuating 3D Bose-Einstein Condensates in Elongated Traps. *Physical Review Letters*, 87(5):050404, 2001.

[19] Demascoth Kadio, Mariusz Gajda, and Kazimierz Rzążewski. Phase fluctuations of a Bose-Einstein condensate in low-dimensional geometry. *Physical Review A*, 72(1):013607, 2005.

[20] Michael Gring, Maximilian Kuhnert, Tim Langen, Takuya Kitagawa, Bernhard Rauer, Matthias Schreitl, Igor Mazets, David A Smith, Eugene Demler, and Jörg Schmiedmayer. Relaxation and Prethermalization in an Isolated Quantum System. *Science*, 337(6100):1318–1322, 2012.

[21] S. Dettmer, D. Hellweg, P. Ryytty, J. J. Arlt, W. Ertmer, K. Sengstock, D. S. Petrov, G. V. Shlyapnikov, H. Kreutzmann, L. Santos, and M. Lewenstein. Observation of Phase Fluctuations in Elongated Bose-Einstein Condensates. *Physical Review Letters*, 87(16):160406, 2001.

[22] V Berezinskii. Destruction of Long-range Order in One-dimensional and Two-dimensional Systems Possessing a Continuous Symmetry Group. II. Quantum Systems. *J. Exp. TP*, 34(3):610, 1971.

[23] J M Kosterlitz and D J Thouless. Ordering, metastability and phase transitions in two-dimensional systems. *Journal of Physics C: Solid State Physics*, 6(7):1181–1203, 1973.

[24] Zoran Hadzibabic, Peter Krüger, Marc Cheneau, Baptiste Battelier, and Jean Dalibard. Berezinskii-Kosterlitz-Thouless crossover in a trapped atomic gas. *Nature*, 441(7097):1118–1121, 2006.

[25] T Langen, R Geiger, M Kuhnert, B Rauer, and Jörg Schmiedmayer. Local emergence of thermal correlations in an isolated quantum many-body system. *Nature Physics*, 9(10):640–643, 2013.

[26] Tim Langen, Remi Geiger, and Jörg Schmiedmayer. Ultracold Atoms Out of Equilibrium. *Annual Review of Condensed Matter Physics*, 6(1):201–217, 2015.

[27] T. Langen, T. Schweigler, E. Demler, and J. Schmiedmayer. Double light-cone dynamics establish thermal states in integrable 1D Bose gases. *New Journal of Physics*, 20(2):023034, 2018.

[28] Christian-Marcel Schmied, Aleksandr N. Mikheev, and Thomas Gasenzer. Prescaling in a Far-from-Equilibrium Bose Gas. *Physical Review Letters*, 122(17):170404, 2019.

[29] Maximilian Prüfer, Philipp Kunkel, Helmut Strobel, Stefan Lannig, Daniel Linnemann, Christian-Marcel Schmied, Jürgen Berges, Thomas Gasenzer, and Markus K. Oberthaler. Observation of universal dynamics in a spinor Bose gas far from equilibrium. *Nature*, 563(7730):217–220, 2018.

[30] Christoph Eigen, Jake A.P. Glidden, Raphael Lopes, Nir Navon, Zoran Hadzibabic, and Robert P. Smith. Universal Scaling Laws in the Dynamics of a Homogeneous Unitary Bose Gas. *Physical Review Letters*, 119(25):250404, 2017.

[31] J Berges, Sz. Borsányi, and C Wetterich. Prethermalization. *Physical Review Letters*, 93(14):142002, 2004.

[32] Sebastian Erne, Robert Bücker, Thomas Gasenzer, Jürgen Berges, and Jörg Schmiedmayer. Universal dynamics in an isolated one-dimensional Bose gas far from equilibrium. *Nature*, 563(7730):225–229, 2018.

[33] Christoph Eigen, Jake A. P. Glidden, Raphael Lopes, Eric A. Cornell, Robert P. Smith, and Zoran Hadzibabic. Universal prethermal dynamics of Bose gases quenched to unitarity. *Nature*, 563(7730):221–224, 2018.

[34] T. L. Harte, E. Bentine, K. Luksch, A. J. Barker, D. Trypogeorgos, B. Yuen, and C. J. Foot. Ultracold atoms in multiple radio-frequency dressed adiabatic potentials. *Physical Review A*, 97(1):013616, 2018.

[35] T Morgan, Th Busch, and T Fernholz. Adiabatic potentials using multiple radio frequencies. *arXiv:1405.2534*, 2014.

[36] A. J. Barker, S. Sunami, D. Garrick, A. Beregi, K. Luksch, E. Bentine, and C. J. Foot. Realising a species-selective double well with multiple-radiofrequency-dressed potentials. *Journal of Physics B: Atomic, Molecular and Optical Physics*, 53(15):155001, 2020.

[37] K. Merloti, R. Dubessy, L. Longchambon, A Perrin, P-E Pottie, V. Lorent, and H. Perrin. A two-dimensional quantum gas in a magnetic trap. *New Journal of Physics*, 15(3):033007, 2013.

[38] Y. Colombe, E. Knyazchyan, O. Morizot, B. Mercier, V. Lorent, and H. Perrin. Ultracold atoms confined in rf-induced two-dimensional trapping potentials. *Europhysics Letters (EPL)*, 67(4):593–599, 2004.

[39] S. Hofferberth, B. Fischer, T. Schumm, J. Schmiedmayer, and I. Lesanovsky. Ultracold atoms in radio-frequency dressed potentials beyond the rotating-wave approximation. *Physical Review A*, 76(1):013401, 2007.

[40] Hélène Perrin and Barry M Garraway. Trapping Atoms With Radio Frequency Adiabatic Potentials. In *Advances in Atomic, Molecular and Optical Physics.*, pages 181–262. Elsevier, 2017.

[41] S Hofferberth, I Lesanovsky, B Fischer, T Schumm, and Jörg Schmiedmayer. Non-equilibrium coherence dynamics in one-dimensional Bose gases. *Nature*, 449(7160):324–327, 2007.

[42] Adam J. Barker, Harry Style, Kathrin Luksch, Shinichi Sunami, David Garrick, Felix Hill, Christopher J. Foot, and Elliot Bentine. Applying machine learning optimization methods to the production of a quantum gas. *Machine Learning: Science and Technology*, 1(1):015007, 2020.

[43] Elliot Bentine, Adam J. Barker, Kathrin Luksch, Shinichi Sunami, Tiffany L. Harte, Ben Yuen, Christopher J. Foot, Daniel J. Owens, and Jeremy M. Hutson. Inelastic collisions in radiofrequency-dressed mixtures of ultracold atoms. *Physical Review Research*, 2:133163, 2020.

[44] Adam J. Barker, Shinichi Sunami, David Garrick, Abel Beregi, Kathrin Luksch, Elliot Bentine, and Christopher J. Foot. Coherent splitting of two-dimensional Bose gases in magnetic potentials. *New Journal of Physics*, 22:103040, 2020.

[45] A Einstein. The Quantum Theory of Radiation. *Physikalische Zeitschrift*, 181(121), 1917.

[46] J von Fraunhofer. Bestimmung des Brechungsund Farbenzerstreuung-Vermogens verschiedener Glasarten in Bezug auf die Vervollkommnung achromatischer Fernrohre. *Denkschriften der Koniglichen Akademie der Wissenschaften zu Munchen fur die Jahre 1814 und 1815*, 5:193–226, 1817.

[47] J.R. Rydberg. Investigations of the composition of the emission spectra of chemical elements. *Kongliga Svenska Vetenskaps-Akademiens Handlingar*, 23:1–177, 1889.

[48] E Schrödinger. An Undulatory Theory of the Mechanics or Atoms and Molecules. *The Physical Review*, 28(6), 1926.

[49] N. Bohr. On the constitution of atoms and molecules. In *Philosophical Magazine*, volume 26. Birkhauser Boston, 1913.

[50] A. Sommerfeld. Zur Theorie der Balmerschen Serie. *Sitzungberichte der Bayerischen Akademie der Wissenschaften (München), mathematischphysikalische Klasse*, pages 425–458, 1915.

[51] David J. Griffiths and Darrell F. Schroeter. *Introduction to Quantum Mechanics*. Cambridge University Press, 2018.

[52] Christopher J Foot. *Atomic Physics*. Oxford University Press, 2005.

[53] G. A. Sinuco-Leon, B. M. Garraway, H. Mas, S. Pandey, G. Vasilakis, V. Bolpasi, W. von Klitzing, B. Foxon, S. Jammi, K. Poulios, and T. Fernholz. Microwave spectroscopy of radio-frequency-dressed Rb-87. *Physical Review A*, 100(5):053416, 2019.

[54] Hector Mas, Saurabh Pandey, Georgios Vasilakis, and Wolf von Klitzing. Bichromatic adiabatic shells for atom interferometry. *New Journal of Physics*, 21(12):123039, 2019.

[55] G. Breit and I. I. Rabi. Measurement of Nuclear Spin. *Physical Review*, 38(11):2082–2083, 1931.

[56] Claude Cohen-Tannoudji, Jacques Dupont-Roc, and Gilbert Grynberg. *Atom-Photon Interactions*. Wiley-VCH Verlag GmbH, Weinheim, Germany, 1998.

[57] Elliot Bentine. Atomic Mixtures in Radiofrequency-Dressed Potentials, DPhil thesis, University of Oxford, 2018.

[58] K. Luksch, E. Bentine, A. J. Barker, S. Sunami, T. L. Harte, B. Yuen, and C. J. Foot. Probing multiple-frequency atom-photon interactions with ultracold atoms. *New Journal of Physics*, 21(7):073067, 2019.

[59] Barry M Garraway and Hélène Perrin. Recent developments in trapping and manipulation of atoms with adiabatic potentials. *Journal of Physics B: Atomic, Molecular and Optical Physics*, 49(17):172001, 2016.

[60] Kathryn A Burrows, Hélène Perrin, and Barry M Garraway. Nonadiabatic losses from radio-frequency-dressed cold-atom traps: Beyond the Landau-Zener model. *Physical Review A*, 96(2):023429, 2017.

[61] Tiffany Laura Harte. Ultracold Atoms in Dressed Potentials, DPhil thesis, University of Oxford, 2017.

[62] Kathrin Luksch. Investigating the spectrum of atoms in multiple-radiofrequency dressed potentials for coherent splitting of quantum gases, DPhil thesis, University of Oxford, 2019.

[63] R. Kollengode Easwaran, L. Longchambon, P-E Pottie, V. Lorent, H. Perrin, and B. M. Garraway. RF spectroscopy in a resonant RF-dressed trap. *Journal of Physics B: Atomic, Molecular and Optical Physics*, 43(6):065302, 2010.

[64] D. Trypogeorgos. Periodically driven atomic systems, DPhil thesis, University of Oxford, 2014.

[65] E Bentine, T L Harte, K Luksch, A J Barker, J Mur-Petit, B Yuen, and C J Foot. Species-selective confinement of atoms dressed with multiple radiofrequencies. *Journal of Physics B: Atomic, Molecular and Optical Physics*, 50(9):094002, 2017.

[66] M. H. T. Extavour, L. J. LeBlanc, T. Schumm, B. Cieslak, S. Myrskog, A. Stummer, S. Aubin, and J. H. Thywissen. Dual-Species Quantum Degeneracy of 40K and 87Rb on an Atom Chip. In *AIP Conference Proceedings*, volume 869, pages 241–249. AIP, 2006.

[67] I. Lesanovsky, S. Hofferberth, J. Schmiedmayer, and P. Schmelcher. Manipulation of ultracold atoms in dressed adiabatic radio-frequency potentials. *Physical Review A*, 74(3):033619, 2006.

[68] R. Stevenson, M. R. Hush, T. Bishop, I. Lesanovsky, and T. Fernholz. Sagnac Interferometry with a Single Atomic Clock. *Physical Review Letters*, 115(16):163001, 2015.

[69] P Navez, S Pandey, H Mas, K Poulios, T Fernholz, and W von Klitzing. Matter-wave interferometers using TAAP rings. *New Journal of Physics*, 18(7):075014, 2016.

[70] Ben Yuen and Christopher J. Foot. Multi-Frequency Atom-Photon Interactions. *arXiv:1907.01469*, 2019.

[71] German A. Sinuco-León and Barry M. Garraway. Radio-frequency dressed lattices for ultracold alkali atoms. *New Journal of Physics*, 17(5):053037, 2015.

[72] O. Zobay and B. M. Garraway. Atom trapping and two-dimensional Bose-Einstein condensates in field-induced adiabatic potentials. *Physical Review A*, 69(2):023605, 2004.

[73] B. E. Sherlock. Ultracold quantum gases in time-averaged adiabatic potentials, DPhil thesis, University of Oxford, 2011.

[74] E. L. Raab, M. Prentiss, Alex Cable, Steven Chu, and D. E. Pritchard. Trapping of Neutral Sodium Atoms with Radiation Pressure. *Physical Review Letters*, 59(23):2631–2634, 1987.

[75] C Cohen-Tannoudji. Manipulating Atoms with Photons. Nobel Prize Lecture, 1998.

[76] Stephan Falke, Nathan Lemke, Christian Grebing, Burghard Lipphardt, Stefan Weyers, Vladislav Gerginov, Nils Huntemann, Christian Hagemann, Ali Al-Masoudi, Sebastian Häfner, Stefan Vogt, Uwe Sterr, and Christian Lisdat. A strontium lattice clock with 3 10 17 inaccuracy and its frequency. *New Journal of Physics*, 16(7):073023, 2014.

[77] C. J. Ballance, T. P. Harty, N. M. Linke, M. A. Sepiol, and D. M. Lucas. High Fidelity Quantum Logic Gates Using Trapped-Ion Hyperfine Qubits. *Physical Review Letters*, 117(6):060504, 2016.

[78] Daniel A Steck. Rubidium 85 D Line Data. 2001.

[79] J.J. Arlt, O. Maragò, S. Webster, S. Hopkins, and C.J. Foot. A pyramidal magneto-optical trap as a source of slow atoms. *Optics Communications*, 157(1-6):303–309, 1998.

[80] Daniel A Steck. Rubidium 87 D Line Data. 2001.

[81] S. N. Atutov, V. Biancalana, P. Bicchi, C. Marinelli, E. Mariotti, M. Meucci, A. Nagel, K. A. Nasyrov, S. Rachini, and L. Moi. Light-induced diffusion and desorption of alkali metals in a siloxane film: Theory and experiment. *Physical Review A*, 60(6):4693–4700, 1999.

[82] C. Klempt, T. van Zoest, T. Henninger, O. Topic, E. Rasel, W. Ertmer, and J. Arlt. Ultraviolet light-induced atom desorption for large rubidium and potassium magneto-optical traps. *Physical Review A*, 73(1):013410, 2006.

[83] T. Karaulanov, M. T. Graf, D. English, S. M. Rochester, Y. J. Rosen, K. Tsigutkin, D. Budker, E. B. Alexandrov, M. V. Balabas, D. F. Jackson Kimball, F. A. Narducci, S. Pustelny, and V. V. Yashchuk. Controlling atomic vapor density in paraffin-coated cells using light-induced atomic desorption. *Physical Review A*, 79(1):012902, 2009.

[84] M Meucci, E Mariotti, P Bicchi, C Marinelli, and L Moi. Light-Induced Atom Desorption. *Europhysics Letters (EPL)*, 25(9):639–643, 1994.

[85] A. Gozzini, F. Mango, J. H. Xu, G. Alzetta, F. Maccarrone, and R. A. Bernheim. Light-induced ejection of alkali atoms in polysiloxane coated cells. *Il Nuovo Cimento D*, 15(5):709–722, 1993.

[86] D. S. Barker, E. B. Norrgard, J. Scherschligt, J. A. Fedchak, and S. Eckel. Light-induced atomic desorption of lithium. *Physical Review A*, 98(4):043412, 2018.

[87] F. Mango and E. Maccioni. Light-induced ejection of calcium atoms from polymer surfaces. *The European Physical Journal D*, 50(3):253–256, 2008.

[88] Krzysztof Rębilas and Marek J. Kasprowicz. Reexamination of the theory of light-induced atomic desorption. *Physical Review A*, 79(4):042903, 2009.

[89] Toptica DL Pro, 2016.

[90] M J Padgett, N Bett, and R J Butcher. A simple frequency discriminator circuit for offset locking of lasers. *Journal of Physics E: Scientific Instruments*, 21(6):554–557, 1988.

[91] D J McCarron, S A King, and S L Cornish. Modulation transfer spectroscopy in atomic rubidium. *Measurement Science and Technology*, 19(10):105601, 2008.

[92] B. T. Sheard. Magnetic Transport and Bose-Einstein Condensation of Rubidium Atoms, DPhil thesis, University of Oxford, 2011.

[93] Stephen Blundell and Katherine M. Blundell. *Concepts in thermal physics*. Oxford University Press, 2010.

[94] C J Pethick and H Smith. *Bose-Einstein Condensation in Dilute Gases*. Cambridge University Press, 2nd edition, 2008.

[95] M. Gildemeister, E. Nugent, B. E. Sherlock, M. Kubasik, B. T. Sheard, and C. J. Foot. Trapping ultracold atoms in a time-averaged adiabatic potential. *Physical Review A*, 81(3):031402, 2010.

[96] C. F. Ockeloen, A. F. Tauschinsky, R. J.C. Spreeuw, and S. Whitlock. Detection of small atom numbers through image processing. *Physical Review A - Atomic, Molecular, and Optical Physics*, 82(6):061606, 2010.

[97] Bo Yan, Min Ke, Xiaolin Li, and Yuzhu Wang. Reduction of interference fringes in absorption imaging of cold atom cloud using eigenface method. *Chinese Optics Letters, Vol. 5, Issue 3, pp. 128-130*, 5(3):128–130, 2007.

[98] Andika Putra, Daniel L. Campbell, Ryan M. Price, Subhadeep De, and I. B. Spielman. Optimally focused cold atom systems obtained using density-density correlations. *Review of Scientific Instruments*, 85(1):013110, 2014.

[99] Josh Patterson and Adam Gibson. *Deep learning : a practitioner's approach*. O'Reilly, 1 edition, 2015.

[100] Hokey Min. Artificial intelligence in supply chain management: theory and applications. *International Journal of Logistics Research and Applications*, 13(1):13–39, 2010.

[101] Daniel S. Kermany. Identifying Medical Diagnoses and Treatable Diseases by Image-Based Deep Learning. *Cell*, 172(5):1122–1131.e9, 2018.

[102] C. C. Bradley, C. A. Sackett, J. J. Tollett, and R. G. Hulet. Evidence of Bose-Einstein Condensation in an Atomic Gas with Attractive Interactions. *Physical Review Letters*, 75(9):1687–1690, 1995.

[103] Wolfgang Ketterle and N.J. Van Druten. Evaporative Cooling of Trapped Atoms. In *Advances In Atomic, Molecular, and Optical Physics*, volume 37, pages 181–236. Academic Press, 1996.

[104] A. D. Tranter, H. J. Slatyer, M. R. Hush, A. C. Leung, J. L. Everett, K. V. Paul, P. Vernaz-Gris, P. K. Lam, B. C. Buchler, and G. T. Campbell. Multi-parameter optimisation of a magneto-optical trap using deep learning. *Nature Communications*, 9(1):4360, 2018.

[105] I. Geisel, K. Cordes, J. Mahnke, S. Jöllenbeck, J. Ostermann, J. Arlt, W. Ertmer, and C. Klempt. Evolutionary optimization of an experimental apparatus. *Applied Physics Letters*, 102(21):214105, 2013.

[106] P. B. Wigley, P. J. Everitt, A. van den Hengel, J. W. Bastian, M. A. Sooriyabandara, G. D. McDonald, K. S. Hardman, C. D. Quinlivan, P. Manju, C. C. N. Kuhn, I. R. Petersen, A. N. Luiten, J. J. Hope, N. P. Robins, and M. R. Hush. Fast machine-learning online optimization of ultra-cold-atom experiments. *Scientific Reports*, 6(1):25890, 2016.

[107] Michael R. Hush. M-LOOP, 2019.

[108] Fred. Glover and Gary A. Kochenberger. *Handbook of Metaheuristics*. Springer US, 2003.

[109] Michael R. Wagner and Patrick Jaillet. *Online Optimisation*. Springer, 2018.

[110] Rainer Storn and Kenneth Price. Differential Evolution A Simple and Efficient Heuristic for global Optimization over Continuous Spaces. *Journal of Global Optimization*, 11(4):341–359, 1997.

[111] Matthias Seeger. Gaussian Processes for Machine Learning. *International Journal of Neural Systems*, 14(02):69–106, 2004.

[112] Pradnya A. Vikhar. Evolutionary algorithms: A critical review and its future prospects. In *2016 ICGTSPICC*, pages 261–265. IEEE, 2016.

[113] Carl Edward. Rasmussen and Christopher K. I. Williams. *Gaussian processes for machine learning*. MIT Press, 2006.

[114] Jürgen Schmidhuber. Deep learning in neural networks: An overview. *Neural Networks*, 61:85–117, 2015.

[115] Dan Hendrycks and Kevin Gimpel. Gaussian Error Linear Units (GELUs). *arXiv:1606.08415*, 2016.

[116] Sandesh S. Kalantre, Justyna P. Zwolak, Stephen Ragole, Xingyao Wu, Neil M. Zimmerman, M. D. Stewart, and Jacob M. Taylor. Machine learning techniques for state recognition and auto-tuning in quantum dots. *npj Quantum Information*, 5(1):6, 2019.

[117] K. Gnana Sheela and S. N. Deepa. Review on Methods to Fix Number of Hidden Neurons in Neural Networks. *Mathematical Problems in Engineering*, 2013:1–11, 2013.

[118] Diederik P. Kingma and Jimmy Ba. Adam: A Method for Stochastic Optimization. *arXiv:1412.6980*, 2014.

[119] Sebastian Ruder. An overview of gradient descent optimization algorithms. *arXiv:1609.04747*, 2016.

[120] Arnaud Mignan and Marco Broccardo. One neuron is more informative than a deep neural network for aftershock pattern forecasting. *arXiv:1904.01983*, 2019.

[121] D Hangleiter, M T Mitchison, T H Johnson, M Bruderer, M B Plenio, and D Jaksch. Nondestructive selective probing of phononic excitations in a cold Bose gas using impurities. *Physical Review A*, 91(1):013611, 2015.

[122] M. A. Cirone, G De Chiara, G. M. Palma, and A. Recati. Collective decoherence of cold atoms coupled to a Bose-Einstein condensate. *New Journal of Physics*, 11(10):103055, 2009.

[123] Mohammad Mehboudi, Aniello Lampo, Christos Charalambous, Luis A Correa, Miguel Ángel García-March, and Maciej Lewenstein. Using Polarons for sub-nK Quantum Nondemolition Thermometry in a Bose-Einstein Condensate. *Physical Review Letters*, 122(3):030403, 2019.

[124] Carlos Sabín, Angela White, Lucia Hackermuller, and Ivette Fuentes. Impurities as a quantum thermometer for a Bose-Einstein condensate. *Scientific Reports*, 4(1):6436, 2015.

[125] Luis A. Correa, Mohammad Mehboudi, Gerardo Adesso, and Anna Sanpera. Individual Quantum Probes for Optimal Thermometry. *Physical Review Letters*, 114(22):220405, 2015.

[126] H. P. Büchler and G. Blatter. Supersolid versus Phase Separation in Atomic Bose-Fermi Mixtures. *Physical Review Letters*, 91(13):130404, 2003.

[127] B. J. DeSalvo, Krutik Patel, Geyue Cai, and Cheng Chin. Observation of fermion-mediated interactions between bosonic atoms. *Nature*, 568(7750):61–64, 2019.

[128] F Schreck, L Khaykovich, K L Corwin, G Ferrari, T Bourdel, J Cubizolles, and C Salomon. Quasipure Bose-Einstein Condensate Immersed in a Fermi Sea. *Physical Review Letters*, 87(8):080403, 2001.

[129] S. G. Crane, X. Zhao, W. Taylor, and D. J. Vieira. Trapping an isotopic mixture of fermionic 84Rb and bosonic 87Rb. *Physical Review A*, 62(1):011402, 2000.

[130] S. B. Papp, J. M. Pino, and C. E. Wieman. Tunable Miscibility in a Dual-Species Bose-Einstein Condensate. *Physical Review Letters*, 101(4):040402, 2008.

[131] Kean Loon Lee, Nils B. Jørgensen, I-Kang Liu, Lars Wacker, Jan J. Arlt, and Nick P. Proukakis. Phase separation and dynamics of two-component Bose-Einstein condensates. *Physical Review A*, 94(1):013602, 2016.

[132] QuProCS - Home.

[133] A Usui, B Buča, and J Mur-Petit. Quantum probe spectroscopy for cold atomic systems. *New J. Phys*, 20:103006, 2018.

[134] Roberto Onofrio and Carlo Presilla. Reaching Fermi Degeneracy in Two-Species Optical Dipole Traps. *Physical Review Letters*, 89(10):100401, 2002.

[135] J. Catani, G. Lamporesi, D. Naik, M. Gring, M. Inguscio, F. Minardi, A. Kantian, and T. Giamarchi. Quantum dynamics of impurities in a one-dimensional Bose gas. *Physical Review A - Atomic, Molecular, and Optical Physics*, 85(2), 2012.

[136] C. C N Kuhn, G. D. McDonald, K. S. Hardman, S. Bennetts, P. J. Everitt, P. A. Altin, J. E. Debs, J. D. Close, and N. P. Robins. A Bose-condensed, simultaneous dual-species Mach-Zehnder atom interferometer. *New Journal of Physics*, 16(7):073035, 2014.

[137] A. Bonnin, N. Zahzam, Y. Bidel, and A. Bresson. Simultaneous dual-species matter-wave accelerometer. *Physical Review A*, 88(4):043615, 2013.

[138] L. J. LeBlanc and J. H. Thywissen. Species-specific optical lattices. *Physical Review A*, 75(5):053612, 2007.

[139] S. Hofferberth, I. Lesanovsky, B. Fischer, J. Verdu, and J. Schmiedmayer. Radiofrequency-dressed-state potentials for neutral atoms. *Nature Physics*, 2(10):710–716, 2006.

[140] Daniel J. Owens and Jeremy M. Hutson. Inelastic losses in radio-frequency-dressed traps for ultracold atoms. *Physical Review A*, 96(4):042707, 2017.

[141] P. S. Julienne, F. H. Mies, E. Tiesinga, and C. J. Williams. Collisional Stability of Double Bose Condensates. *Physical Review Letters*, 78(10):1880–1883, 1997.

[142] T. V. Tscherbul, T. Calarco, I. Lesanovsky, R. V. Krems, A. Dalgarno, and J. Schmiedmayer. rf-field-induced Feshbach resonances. *Physical Review A*, 81(5):050701, 2010.

[143] B. S. Rem, A. T. Grier, I. Ferrier-Barbut, U. Eismann, T. Langen, N. Navon, L. Khaykovich, F. Werner, D. S. Petrov, F. Chevy, and C. Salomon. Lifetime of the Bose gas with resonant interactions. *Physical Review Letters*, 110(16):163202, 2013.

[144] Richard J. Fletcher, Alexander L. Gaunt, Nir Navon, Robert P. Smith, and Zoran Hadzibabic. Stability of a Unitary Bose Gas. *Physical Review Letters*, 111(12):125303, 2013.

[145] R. W. Pattinson, T. P. Billam, S. A. Gardiner, D. J. McCarron, H. W. Cho, S. L. Cornish, N. G. Parker, and N. P. Proukakis. Equilibrium solutions for immiscible two-species Bose-Einstein condensates in perturbed harmonic traps. *Physical Review A*, 87(1):013625, 2013.

[146] D. S. Petrov, D. M. Gangardt, and G. V. Shlyapnikov. Low-dimensional trapped gases. *Journal de Physique IV (Proceedings)*, 116:5–44, 2004.

[147] N. D. Mermin and H. Wagner. Absence of Ferromagnetism or Antiferromagnetism in One- or Two-Dimensional Isotropic Heisenberg Models. *Physical Review Letters*, 17(22):1133–1136, 1966.

[148] Vanderlei Bagnato and Daniel Kleppner. Bose-Einstein condensation in low-dimensional traps. *Physical Review A*, 44(11):7439–7441, 1991.

[149] P. C. Hohenberg. Existence of Long-Range Order in One and Two Dimensions. *Physical Review*, 158(2):383–386, 1967.

[150] Jorge José, editor. *40 Years of Berenzinskii-Kosterlitz-Thouless Theory*. World Scientific, 2013.

[151] Richard J. Fletcher, Martin Robert-de Saint-Vincent, Jay Man, Nir Navon, Robert P. Smith, Konrad G.H. Viebahn, and Zoran Hadzibabic. Connecting Berezinskii-Kosterlitz-Thouless and BEC Phase Transitions by Tuning Interactions in a Trapped Gas. *Physical Review Letters*, 114(25):255302, 2015.

[152] Markus Holzmann, Gordon Baym, J.-P. Blaizot, and F. Laloë. Superfluid transition of homogeneous and trapped two-dimensional Bose gases. *Proceedings of the National Academy of Sciences*, 104(5):1476–1481, 2007.

[153] Markus Holzmann and Werner Krauth. Kosterlitz-Thouless Transition of the Quasi-Two-Dimensional Trapped Bose Gas. *Physical Review Letters*, 100(19):190402, 2008.

[154] D. J. Bishop and J. D. Reppy. Study of the superfluid transition in two-dimensional He4 films. *Physical Review Letters*, 40(26):1727–1730, 1978.

[155] Maximilian Prüfer, Torsten V. Zache, Philipp Kunkel, Stefan Lannig, Alexis Bonnin, Helmut Strobel, Jürgen Berges, and Markus K. Oberthaler. Experimental extraction of the quantum effective action for a non-equilibrium many-body system. *arXiv:1909.05120*, 2019.

[156] Lauriane Chomaz, Laura Corman, Tom Bienaimé, Rémi Desbuquois, Christof Weitenberg, Sylvain Nascimbène, Jérôme Beugnon, and Jean Dalibard. Emergence of coherence via transverse condensation in a uniform quasi-two-dimensional Bose gas. *Nature Communications*, 6:6162, 2015.

[157] Rémi Desbuquois, Lauriane Chomaz, Tarik Yefsah, Julian Léonard, Jérôme Beugnon, Christof Weitenberg, and Jean Dalibard. Superfluid behaviour of a two-dimensional Bose gas. *Nature Physics*, 8(9):645–648, 2012.

[158] Nikolay Prokof'ev, Oliver Ruebenacker, and Boris Svistunov. Critical Point of a Weakly Interacting Two-Dimensional Bose Gas. *Physical Review Letters*, 87(27):270402, 2001.

[159] Peter Krüger, Zoran Hadzibabic, and Jean Dalibard. Critical Point of an Interacting Two-Dimensional Atomic Bose Gas. *Physical Review Letters*, 99(4):040402, 2007.

[160] Tim Langen, Thomas Gasenzer, and Jörg Schmiedmayer. Prethermalization and universal dynamics in near-integrable quantum systems. *Journal of Statistical Mechanics: Theory and Experiment*, 2016(6):064009, 2016.

[161] J Eisert, M Friesdorf, and C Gogolin. Quantum many-body systems out of equilibrium. *Nature Physics*, 11(2):124–130, 2015.

[162] Marcos Rigol, Vanja Dunjko, and Maxim Olshanii. Thermalization and its mechanism for generic isolated quantum systems. *Nature*, 452(7189):854–858, 2008.

[163] Zoran Hadzibabic and Jean Dalibard. Two-dimensional Bose fluids: An atomic physics perspective. *arXiv:0912.1490*, 2009.

[164] Jae-Yoon Choi, Sang Won Seo, and Yong-il Shin. Observation of Thermally Activated Vortex Pairs in a Quasi-2D Bose Gas. *Physical Review Letters*, 110(17):175302, 2013.

[165] David R. Nelson and J. M. Kosterlitz. Universal Jump in the Superfluid Density of Two-Dimensional Superfluids. *Physical Review Letters*, 39(19):1201–1205, 1977.

[166] S. Giorgini, L. P. Pitaevskii, and S. Stringari. Condensate fraction and critical temperature of a trapped interacting Bose gas. *Physical Review A - Atomic, Molecular, and Optical Physics*, 54(6):R4633–R4636, 1996.

[167] Richard J. Fletcher. Bose-Einstein Condensation and Superfluidity in Two Dimensions, PhD thesis, University of Cambridge, 2015.

[168] Camilla De Rossi, Romain Dubessy, Karina Merloti, Mathieu de Goër de Herve, Thomas Badr, Aurélien Perrin, Laurent Longchambon, and Hélène Perrin. The scissors oscillation of a quasi two-dimensional Bose gas as a local signature of superfluidity. *Journal of Physics: Conference Series*, 793:012023, 2017.

[169] O. M. Maragò, S. A. Hopkins, J. Arlt, E. Hodby, G. Hechenblaikner, and C. J. Foot. Observation of the Scissors Mode and Evidence for Superfluidity of a Trapped Bose-Einstein Condensed Gas. *Physical Review Letters*, 84(10):2056–2059, 2000.

[170] P. A. Murthy, D. Kedar, T. Lompe, M. Neidig, M. G. Ries, A. N. Wenz, G. Zürn, and S. Jochim. Matter-wave Fourier optics with a strongly interacting two-dimensional Fermi gas. *Physical Review A*, 90(4):043611, 2014.

[171] I. Shvarchuck, Ch Buggle, D. S. Petrov, K. Dieckmann, M. Zielonkowski, M. Kemmann, T. G. Tiecke, W. von Klitzing, G. V. Shlyapnikov, and J. T.M. Walraven. Bose-Einstein Condensation into Nonequilibrium States Studied by Condensate Focusing. *Physical Review Letters*, 89(27):270404, 2002.

[172] L. P. Pitaevskii and A. Rosch. Breathing modes and hidden symmetry of trapped atoms in two dimensions. *Physical Review A*, 55(2):R853–R856, 1997.

[173] T. Peppler, P. Dyke, M. Zamorano, I. Herrera, S. Hoinka, and C. J. Vale. Quantum Anomaly and 2D-3D Crossover in Strongly Interacting Fermi Gases. *Physical Review Letters*, 121(12):120402, 2018.

[174] Maxim Olshanii, Hélène Perrin, and Vincent Lorent. Example of a Quantum Anomaly in the Physics of Ultracold Gases. *Physical Review Letters*, 105(9):095302, 2010.

[175] Karina Merloti, Romain Dubessy, Laurent Longchambon, Maxim Olshanii, and Hélène Perrin. Breakdown of scale invariance in a quasi-two-dimensional Bose gas due to the presence of the third dimension. *Physical Review A*, 88(6):061603, 2013.

[176] P. A. Murthy, I. Boettcher, L. Bayha, M. Holzmann, D. Kedar, M. Neidig, M. G. Ries, A. N. Wenz, G. Zürn, and S. Jochim. Observation of the Berezinskii-Kosterlitz-Thouless Phase Transition in an Ultracold Fermi Gas. *Physical Review Letters*, 115(1):010401, 2015.

[177] L Mathey and Anatoli Polkovnikov. Supercritical superfluid and vortex unbinding following a quantum quench. *Physical Review A*, 80(4):041601, 2009.

[178] L Mathey and Anatoli Polkovnikov. Light cone dynamics and reverse Kibble-Zurek mechanism in two-dimensional superfluids following a quantum quench. *Physical Review A*, 81(3):033605, 2010.

[179] Adilet Imambekov, Vladimir Gritsev, and Eugene Demler. Fundamental noise in matter interferometers. *Proceedings of the International School of Physics "Enrico Fermi"*, 164:535–606, 2007.

[180] Anatoli Polkovnikov, Ehud Altman, and Eugene Demler. Interference between independent fluctuating condensates. *Proceedings of the National Academy of Sciences*, 103(16):6125–6129, 2006.

[181] Anatoli Polkovnikov, Krishnendu Sengupta, Alessandro Silva, and Mukund Vengalattore. Colloquium : Nonequilibrium dynamics of closed interacting quantum systems. *Reviews of Modern Physics*, 83(3):863–883, 2011.

[182] D Adu Smith, M Gring, T Langen, M Kuhnert, B Rauer, R Geiger, T Kitagawa, I Mazets, E Demler, and Jörg Schmiedmayer. Prethermalization revealed by the relaxation dynamics of full distribution functions. *New Journal of Physics*, 15(7):075011, 2013.

[183] Thomas Schweigler, Valentin Kasper, Sebastian Erne, Igor Mazets, Bernhard Rauer, Federica Cataldini, Tim Langen, Thomas Gasenzer, Jürgen Berges, and Jörg Schmiedmayer. Experimental characterization of a quantum many-body system via higher-order correlations. *Nature*, 545(7654):323, 2017.

[184] Marine Pigneur, Tarik Berrada, Marie Bonneau, Thorsten Schumm, Eugene Demler, and Jörg Schmiedmayer. Relaxation to a Phase-Locked Equilibrium State in a One-Dimensional Bosonic Josephson Junction. *Physical Review Letters*, 120(17):173601, 2018.

[185] Bernhard Rauer, Sebastian Erne, Thomas Schweigler, Federica Cataldini, Mohammadamin Tajik, and Jörg Schmiedmayer. Recurrences in an isolated quantum many-body system. *Science*, 360(6386):307–310, 2018.

[186] Niclas Luick, Lennart Sobirey, Markus Bohlen, Vijay Pal Singh, Ludwig Mathey, Thomas Lompe, and Henning Moritz. An ideal Josephson junction in an ultracold two-dimensional Fermi gas. *arXiv:1908.09776*, 2019.

[187] Vijay Pal Singh, Niclas Luick, Lennart Sobirey, and Ludwig Mathey. Josephson junction dynamics in a two-dimensional ultracold Bose gas. *arXiv:2002.08375*, 2020.

[188] L Mathey, Kenneth J Günter, Jean Dalibard, and Anatoli Polkovnikov. Dynamic Kosterlitz-Thouless transition in two-dimensional Bose mixtures of ultracold atoms. *Physical Review A*, 95(5):053630, 2017.

[189] T W B Kibble. Topology of cosmic domains and strings. *Journal of Physics A: Mathematical and General*, 9(8):1387–1398, 1976.

[190] Nir Navon, A. L. Gaunt, Robert P. Smith, and Zoran Hadzibabic. Critical dynamics of spontaneous symmetry breaking in a homogeneous Bose gas. *Science*, 347(6218):167–170, 2015.

[191] Jérôme Beugnon and Nir Navon. Exploring the Kibble-Zurek mechanism with homogeneous Bose gases. *Journal of Physics B: Atomic, Molecular and Optical Physics*, 50(2):022002, 2017.

[192] Shinichi Sunami. In preparation, 2021.

[193] P. Cladé, C. Ryu, A. Ramanathan, K. Helmerson, and W. Phillips. Observation of a 2D Bose Gas: From Thermal to Quasicondensate to Superfluid. *Physical Review Letters*, 102(17):170401, 2009.

[194] Steffen Patrick Rath and Wilhelm Zwerger. Full counting statistics of the interference contrast from independent Bose-Einstein condensates. *Physical Review A*, 82(5):053622, 2010.

[195] Z Hadzibabic, P Krüger, M Cheneau, S P Rath, and J Dalibard. The trapped two-dimensional Bose gas: from Bose-Einstein condensation to Berezinskii-Kosterlitz-Thouless physics. *New Journal of Physics*, 10(4):045006, 2008.

[196] Alexander D. Cronin, Jörg Schmiedmayer, and David E. Pritchard. Optics and interferometry with atoms and molecules. *Reviews of Modern Physics*, 81(3):1051–1129, 2009.

[197] Michael Albiez, Rudolf Gati, Jonas Fölling, Stefan Hunsmann, Matteo Cristiani, and Markus K. Oberthaler. Direct Observation of Tunneling and Nonlinear Self-Trapping in a Single Bosonic Josephson Junction. *Physical Review Letters*, 95(1):010402, 2005.

[198] A.G. Bratsos. The solution of the two-dimensional sine-Gordon equation using the method of lines. *Journal of Computational and Applied Mathematics*, 206(1):251–277, 2007.

[199] Yuri D. van Nieuwkerk and Fabian H. L. Essler. Self-consistent time-dependent harmonic approximation for the sine-Gordon model out of equilibrium. *Journal of Statistical Mechanics: Theory and Experiment*, page 084012, 2018.

[200] M. R. Andrews, C. G. Townsend, H.-J. Miesner, D. S. Durfee, D. M. Kurn, and W. Ketterle. Observation of Interference Between Two Bose Condensates. *Science*, 275(5300):637–641, 1997.

[201] Romain Dubessy, Camilla De Rossi, Thomas Badr, Laurent Longchambon, and Hélène Perrin. Imaging the collective excitations of an ultracold gas using statistical correlations. *New Journal of Physics*, 16(12):122001, 2014.

[202] Romain Dubessy, Camilla De Rossi, Mathieu de Goër De Herve, Thomas Badr, Aurélien Perrin, Laurent Longchambon, and Hélène Perrin. Local correlations reveal the superfluid to normal boundary in a trapped two-dimensional quantum gas. 2018.

[203] Mark A. Kasevich. Coherence with Atoms. *Science*, 298(5597):1363–1368, 2002.

[204] J. M. McGuirk, G. T. Foster, J. B. Fixler, M. J. Snadden, and M. A. Kasevich. Sensitive absolute-gravity gradiometry using atom interferometry. *Physical Review A*, 65(3):033608, 2002.

[205] Tom Kibble. Phase-transition dynamics in the lab and the universe. *Physics Today*, 60(9):47–52, 2007.

[206] L Pitaevskii and S Stringari. *Bose-Einstein Condensation and Superfluidity*. Oxford University Press, 2016.

[207] L P Pitaevskii. Vortex Lines in an Imperfect Bose Gas. *J. Exptl. Theoret. Phys. (U.S.S.R.)*, 13(40):646–651, 1961.

[208] E Gross. Structure of a Quantised Vortex in Boson Systems. *Il Nuovo Cimento*, 20:454–477, 1961.

[209] A. Minguzzi. Numerical methods for atomic quantum gases with applications to Bose-Einstein condensates and to ultracold fermions. *Physics Reports*, 395(4-5):223–355, 2004.

[210] Carlo Barenghi and Nick G. Parker. *A Primer on Quantum Fluids*. Springer Briefs in Physics. Springer International Publishing, 2016.

[211] S. B. Papp, J. M. Pino, R. J. Wild, S. Ronen, C. E. Wieman, D. S. Jin, and E A Cornell. Bragg Spectroscopy of a Strongly Interacting Rb85 Bose-Einstein Condensate. *Physical Review Letters*, 101(13):135301, 2008.